LB/TH/35/2025
TH5934

ENHANCED SEPARATION OF HETEROGENEOUS CARBON MICROSPHERES FOR SUPERCAPACITOR ELECTRODES

Liyanage Achini Isanka

198092D

Degree of Master of Philosophy

Department of Chemical and Process Engineering

Faculty of Engineering

University of Moratuwa

Sri Lanka

June 2025

ENHANCED SEPARATION OF HETEROGENEOUS CARBON MICROSPHERES FOR SUPERCAPACITOR ELECTRODES

Liyanage Achini Isanka

198092D

Thesis submitted in partial fulfillment of the requirements for the degree

Master of Philosophy

Department of Chemical and Process Engineering

Faculty of Engineering

University of Moratuwa

Sri Lanka

June 2025

DECLARATION

I declare that this is my own work, and this thesis/dissertation does not incorporate without acknowledgement any material previously submitted for a degree or diploma in any other University or Institute of higher learning and to the best of my knowledge and belief it does not contain any material previously published or written by another person except where the acknowledgement is made in the text. I retain the right to use this content in whole or part in future works (such as articles or books).

Signature: ..... Date: 11/07/2025

L. A. Isanka
Department of Chemical & Process Engineering
University of Moratuwa
Sri Lanka

The above candidate has carried out research for the MPhil thesis under my supervision. I confirm that the declaration made above by the student is true and correct.

Name of Supervisor (PI): Dr. S. A. D. T. Subasinghe
Department of Chemical & Process Engineering
University of Moratuwa
Sri Lanka

Signature of the supervisor: ……. Date: 12/07/2025……..

Name of Supervisor: Prof. (Mrs) Sanja Gunawardena
Department of Chemical & Process Engineering
University of Moratuwa
Sri Lanka

Signature of the supervisor: ……. Date: 12-07-2025……..

DEDICATION

To my family for always believing in me and cheering me on.

ACKNOWLEDGEMENT

I wish to express my deepest gratitude to my supervisors, Dr. Thushara Subasinghe and Prof. (Mrs.) Sanja Gunawardhane for their invaluable guidance, continuous support, supervision, assistance, motivation, and encouragement throughout this period of study.

This research would not have been possible without the generous financial support provided by the Senate research Committee (SRC) for the SRC long term grant (Grant No. SRC/LT/2019/26). I am also profoundly grateful to the academic staff of the Department of Chemical and Process Engineering, University of Moratuwa, for their insightful guidance. Moreover, my sincere gratitude goes to Dr. Chathura Ranasinghe for his immense support with the tools for computational fluid dynamics.

My sincere thanks go to the progress review committee for their expertise and valuable suggestions, as well as to the head and staff of the Faculty of Graduate Studies, University of Moratuwa, for their efforts in facilitating this research degree. I would also like to acknowledge the Department of Material Science Engineering, University of Moratuwa, for allowing me to undertake and complete courses from their MSc. taught programs and for facilitating with equipment for the analysis. My heartfelt thanks to Mr. M.A.P.C. Gunawardana and Mr. D. F. Ranasinghe, staff technical officer from department for assisting me with material testing.

Further, words can't express my gratitude Mrs. I.K. Athukorala, Mr. B. Karunathilaka, Mrs. W.S.M De Silva, Mr. H.L.G.S. Peiris and the non-academic staff of the Department of Chemical and Process Engineering, University of Moratuwa, for their invaluable assistance at every stage of this research.

Special thanks are due to my batchmates and research group members for their support for continuous encouragement. Finally, I am profoundly grateful to my family, whose unwavering belief in me has been my greatest source of strength and motivation throughout this journey.

ABSTRACT

This study focuses on the development and optimization of a microfluidic system for effective separation of carbon microspheres with heterogeneous surface properties. Traditional microparticle separation methods such as, micro-sieving, centrifugal separation, and gravity flotation rely only on size and weight differences. To address this limitation, coated microchannels were employed for the separation process, allowing for separation of microspheres based on surface heterogeneity. The separation efficiency was evaluated by analyzing particle flow rates with ImageJ software, indicating the potential of this approach for precise particle sorting.

Additionally, diffusion experiments were conducted within a microfluidic chip to investigate the impact of externally applied electric fields on the diffusion coefficient of nanoparticles with surface functional groups. The results demonstrated that electric fields could effectively manipulate nanoparticle diffusion, facilitating nanoscale particle separation.

Further, a computational model was developed using ANSYS Fluent to simulate the diffusion behavior of nanoparticles under varying electric field strengths. The model was validated against experimental data collected under identical conditions confirming the reliability of the simulation. This study highlights the potential of microfluidic systems as versatile platforms for advanced particle separation and nanoscale particle manipulation, offering significant implications for materials science, biotechnology, and nanotechnology.

Keywords: Carbon microspheres, Surface chemistry, Microfluidics, Paper based microfluidics

TABLE OF CONTENTS

TABLE OF FIGURES

LIST OF TABLES

LIST OF ABBREVIATIONS

Abbreviation	Description
(FTIR)	Fourier Transform Infrared Spectroscopy
(SEM)	Scanning Electron Microscopy
(UDF)	User Defined Function
(XRD)	X-Ray Diffraction
(PMMA)	Poly Methyl Methacrylate
(ATR)	Attenuated Total Reflectance
(EDLC)	Electrical Double Layer Capacitors
(UPS)	Uninterruptible Power Supplies
(AEDLC)	Asymmetric Electrochemical Double Layer Capacitor
(CNT)	Carbon Nanotubes
(DEP)	Dielectrophoresis
(DNA)	Deoxyribonucleic Acid
(RNA)	Ribonucleic Acid
(SEC)	Size Exclusion Chromatography
(**μ**PAD)	Paper Microfluidic Devices
(FA)	Formic Acid
(TFA)	Trifluoroacetic Acid
(NH_4OH)	Ammonium Hydroxide
(ACN)	Acetonitrile
(MNP)	Magnetic Nanoparticles
(DPA)	Dipicolylamine
(RBC)	Red Blood Cells
(CAM)	Cell Adhesion Molecule
(AA)	Ascorbic Acid
(DA)	Dopamine Hydrochloride
(PBS)	Phosphate-Buffered Saline
(MEMS)	Microelectromechanical Systems

(CTC)	Circulating Tumor Cells
(PCR)	Polymerase Chain Reaction
(PDMS)	Polydimethylsiloxane
(CFD)	Computational Fluid Dynamics
(TEOS)	Tetraethyl Orthosilicate
(CNC)	Computer Numerical Control
(PTFE)	Polytetrafluoroethylene
(LED)	Light Emitting Diode
(FWHM)	Full-Width Half Maximum
(LAP)	Linear Assignment Problem
(HPLC)	High-Performance Liquid Chromatography
(DC)	Direct Current
(LC)	Liquid Chromatography
(HTC)	Hydrothermal Carbonization
(CVD)	Chemical Vapor Deposition
(XPS)	X-ray Photoelectron Spectroscopy
(USP)	Ultrasonic Spray Pyrolysis
(CMOS)	Complementary Metal Oxide Semiconductor

CHAPTER 1

INTRODUCTION

Supercapacitors, also referred to as electrical double-layer capacitors (EDLCs), represent a highly advanced class of energy storage devices that fundamentally differ from traditional capacitors in their method of energy storage. Unlike conventional capacitors, which store energy through the accumulation of electric charge on plates separated by a dielectric material, supercapacitors utilize the electrostatic interactions occurring at the interface between the electrolyte and the electrode [1], [2]. This unique mechanism, involving charge separation across an electric double layer, endows supercapacitors with exceptional capacitance values, significantly higher energy density, and superior power density.

The evolution of supercapacitor technology has witnessed remarkable advancements, positioning it as a superior alternative to conventional battery technologies [3]. The integration of advanced electrode materials and innovative electrolyte solutions has propelled supercapacitors beyond the performance capabilities of traditional batteries [4],[5]. This advancement has facilitated the development of energy storage solutions that offer rapid charge and discharge cycles, high power output, and extended operational lifespans, making supercapacitors indispensable in a variety of modern applications [6], [7].

In the realm of energy storage, devices such as batteries, capacitors, and supercapacitors serve distinct functions, each characterized by unique performance attributes [8]. Supercapacitors, however, have garnered significant attention due to their exceptional attributes, including rapid charge-discharge capabilities, high power density, long cycle life, and a broad operating temperature range [9].

These characteristics render supercapacitors particularly valuable in applications requiring swift energy delivery and robust performance. Their deployment as energy reservoirs in

machinery plays a crucial role in stabilizing the output of electronic equipment, thereby enhancing the overall efficiency and reliability of these systems [5].

Additionally, supercapacitors are integral components in electronic devices such as uninterruptible power supplies (UPS) and volatile memory backups in personal computers (PCs), underscoring their versatility and critical importance in contemporary electronic systems.

1.1 Carbon materials as electrode materials for supercapacitors

Carbon, recognized as one of the most abundant and versatile elements on Earth, plays a pivotal role in the development of electrode materials for supercapacitors. Carbon-based materials, including carbon microspheres, activated carbon, carbon fibers, and carbon nanotubes, are extensively utilized due to their outstanding electrical conductivity, high surface area, and favorable electrochemical properties [10], [11]. Among these materials, carbon microspheres have emerged as a particularly promising choice for supercapacitor electrodes. The spherical morphology of carbon microspheres provides a substantial specific surface area, which is crucial for enhancing the electrochemical performance of supercapacitors [12]. Furthermore, carbon microspheres exhibit high specific capacitance and excellent capacitance retention, making them highly suitable for advanced supercapacitor applications.

The performance characteristics of carbon-based materials in supercapacitors are significantly influenced by their intrinsic chemical and physical properties. These materials exhibit definite heterogeneity, with variations in size, weight, and surface characteristics [13], [14]. Critical surface properties, such as the availability of surface functional groups, surface roughness, porosity, and surface wettability, play decisive roles in determining the overall electrochemical behavior of the electrode material [15].

The optimization of these properties is essential for maximizing the efficiency and performance of supercapacitors. Research in the field of supercapacitors continues to focus on the development and optimization of carbon-based electrodes to achieve higher energy densities, improved power densities, and longer cycle lives [16], [17]. Innovations in material synthesis, surface modification, and structural engineering are pivotal in

advancing the performance of supercapacitors. Supercapacitors represent a cutting-edge solution in energy storage technology, distinguished by their high capacitance, energy density, and power density [18], [19].

1.2 Heterogeneity of carbon microspheres

The heterogeneity of carbon microspheres, a key consideration in supercapacitor electrode design, arises from variations in size, weight, and the presence of diverse surface functional groups [20], [21]. Such differences contribute to the complex and non-uniform nature of these materials. Notably, the presence of oxygen-containing functional groups can impede the efficient migration of ions into the micro pores of the carbon structure. A high concentration of these oxygen functional groups increases the contact resistance, consequently reducing the overall conductivity of the carbon surface [22].

The availability and distribution of functional groups on the surface of carbon microspheres lead to significant alterations in surface chemistry, resulting in heterogeneous surface properties. This heterogeneity contributes to an uneven electrical charge distribution within the pores of the carbon microspheres, thereby limiting the overall energy storage capacity [23], [24]. Additionally, this uneven charge distribution can adversely affect the reproducibility and cycle stability of the supercapacitor, as the non-uniform surface characteristics can lead to inconsistent performance over repeated charge-discharge cycles [25].

Given these challenges, there is a strong preference for homogeneous electrodes in supercapacitor applications. Homogeneous electrodes, characterized by a uniform distribution of surface properties, facilitate smoother charge distribution across the electrode surface. This uniformity is crucial for achieving high energy density, as it ensures efficient ion migration and reduces internal resistance.

Consequently, the use of homogeneous electrodes enhances the overall performance, stability, and longevity of supercapacitors, making them highly desirable for advanced energy storage applications.

1.3 Separation of heterogeneous carbon microspheres

Efficient separation of carbon microspheres, which possess heterogeneous properties, is essential to mitigate uneven charge distribution within carbon-based materials. Size separation of these materials is commonly achieved through a variety of methods, including filtration, centrifugal separation, gravity flotation, inertial forces, and magnetic forces [26]. However, the separation of microspheres that share similar sizes and weights but differ in surface properties poses a significant challenge.

This aspect of separation is critical, as it directly influences the energy storage efficiency of supercapacitors. Addressing this challenge is vital for enhancing the performance and reliability of supercapacitors, necessitating advanced separation techniques that can discriminate based on subtle differences in surface chemistry [27].

1.4 Background of the research

Affinity-based separation is a useful technique for separating carbon microspheres based on their surface properties, which can significantly enhance their performance in applications like supercapacitors. The development of miniaturized on-chip liquid chromatography (LC) systems has garnered significant interest due to their enhanced reproducibility, robustness, and potential for high-throughput analysis.

Compared with on-chip electrophoresis, on-chip LC separation also shows better reproducibility and robustness. Moreover, this can be easily coupled different of detection systems, such as mass spectrometry, fluorescent microscopy, and conductivity detectors.

1.4.1 Affinity-Based Separation

Affinity-based separation is a powerful technique that relies on the specific interactions between ligands and target molecules to achieve selective separation. This method is widely used in various fields, including biochemistry, molecular biology, and analytical chemistry, due to its high specificity and efficiency. By employing binding ligands such as antibodies, aptamers, and metal complexes, affinity-based separation can effectively

isolate specific biomolecules from complex mixtures. A variety of binding ligands can be used in the preparation of affinity chromatography.

1.4.2 Diffusion behavior of nanoparticles

The diffusion behavior of nanoparticles is a critical phenomenon in microfluidics, with applications in material science, biotechnology, and nanotechnology. It is the process by which particles spread from regions higher concentration to those of lower concentration due to random Brownian motion. For nanoparticles, diffusion is influenced by particle size, shape, surface charge, and the properties of the surrounding medium, including viscosity and temperature.

Functionalizing nanoparticles with surface groups complicates their interaction with the medium, often altering their diffusion characteristics. These functionalized nanoparticles are particularly relevant in drug delivery, diagnostics, and targeted therapy, where precise movement control is essential.

The application of external fields can affect the diffusion behavior, and this manipulation allows precise tuning of nanoparticle transport in confined environments, such as microfluidic channels, making it a valuable tool for advanced particle handling.

Understanding and predicting diffusion behavior under these influences requires both experimental and computational methods.

1.5 Problem Statement

Conventional methods for microparticle separation such as micro-sieving, centrifugal separation, and gravity flotation predominantly rely on size and weight differences. These approaches can be useful in some applications but fails to adequately separate particles with heterogeneous surface properties, which are vital in many advanced separation processes. This limitation hinders the precise separation of micro and nanoparticles in fields like biotechnology, materials science, and nanotechnology.

Moreover, the diffusion behavior of nanoparticles, particularly those with functionalized surfaces, is not yet fully understood when subjected to external electric fields. Current research lacks a thorough examination of how these fields influence the transport and behavior of functionalized nanoparticles in confined microfluidic environments. Addressing these gaps is essential for developing advanced microfluidic systems that enable precise separation and manipulation of microspheres and nanoparticles based on surface properties and diffusion characteristics.

1.6 Aim and the objective of the research

1.6.1 Aim of the study

The aim of this study is to develop and optimize a microfluidic system for the precise separation carbon microspheres with heterogeneous surface properties addressing the limitations of conventional size and weight-based separation methods. Moreover, the study investigates the influence of externally applied electric fields on the diffusion behavior of functionalized nanoparticles and develops a computational model to simulate and predict the diffusion behavior of nanoparticles under external fields.

Further a computational model will be developed to simulate the diffusion behavior of nanoparticle under external electric fields. This approach seeks to enhance the understanding and application of microfluidic systems for particle manipulation and separation in a variety of applications.

1.6.2 Research objectives

This research aims to investigate on mechanisms to separate carbon microspheres based on their heterogeneous surface properties. Investigations will be directed to fulfil following objectives.

1. To conduct a comprehensive study on surface characteristics of carbon microspheres.
2. To develop a separation technique based on surface forces to separate heterogeneous carbon microspheres using microfluidic systems.
3. To determine the optimum conditions which enable separation of heterogeneous carbon microspheres based on their surface functional groups.
4. To Evaluate and simulate of the effect of surface forces using dissipative particle dynamics.

CHAPTER 2

LITERATURE REVIEW

In this chapter, a comprehensive review of supercapacitors as energy storage devices, carbon as electrode materials for supercapacitors, methods of separation of heterogeneous carbon microspheres and behavior of carbon microspheres in microfluidic systems are reported.

2.1 Supercapacitors as Energy Storage Devices

Supercapacitors, also known as ultracapacitors or electrochemical capacitors, are advanced energy storage devices that merge the high-power density and rapid charge/discharge capabilities of traditional capacitors with the high energy storage capacity of batteries [28], [2]. This combination makes them uniquely suited for applications requiring quick bursts of energy and long-term reliability. Supercapacitors store energy through electrochemical processes at the electrode-electrolyte interface, enabling them to achieve significantly higher energy densities compared to conventional capacitors.

The supercapacitor has evolved and now overlaps with battery technology by using special electrodes and electrolytes. While the basic Electrochemical Double Layer Capacitor (EDLC) relies on electrostatic action, the Asymmetric Electrochemical Double Layer Capacitor (AEDLC) employs electrodes which are like batteries in achieving a higher energy density. However, this comes with a shorter cycle life and other challenges similar to those faced by batteries. Graphene electrodes hold the promise of enhancing both supercapacitors and batteries.

Voltage limits are acceptable for all capacitors where electrostatic capacitors can be designed to withstand higher voltages up to 2.8V, and higher are possible but result in decreases its lifetime. To achieve higher voltages, multiple supercapacitors can be connected in series. However, this configuration has shown to reduce the total capacitance and increases internal resistance.

The specific energy of supercapacitors spans from 1Wh/kg to 30Wh/kg, which is 10 to 50 times lower than that of Li-ion batteries. Unlike electrochemical batteries that provide a constant voltage throughout their usable power range, supercapacitors exhibit a linear voltage decline during discharge. This behavior limits the effective power output and is considered a key drawback associated with their discharge characteristics.

The voltage and current characteristics during the charge and discharge cycles of a supercapacitor is shown in Figure 2-1 below. During charging, the voltage rises linearly while the current decreases as the capacitor reaches full charge. This eliminates the need for a full-charge detection circuit. This behavior holds true with a constant current supply and within the capacitor's rated voltage.

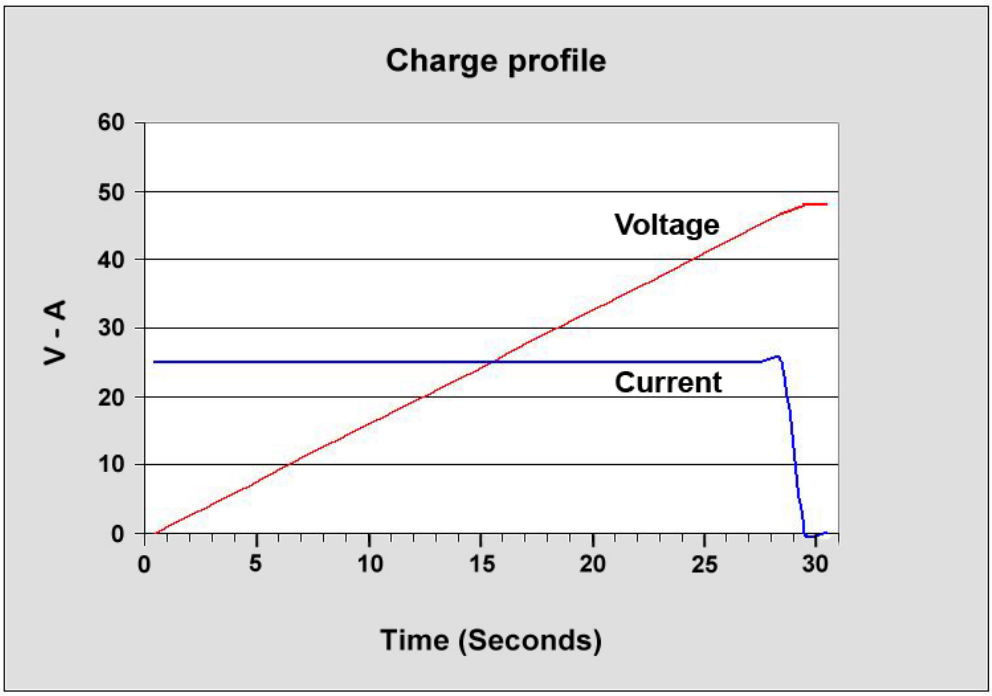

Figure 2-1 Charging characteristics of a supercapacitor (source: [29])

As shown in Figure 2-1 the voltage increases linearly during a constant current charge, and the current naturally drops when the capacitor is fully charged.

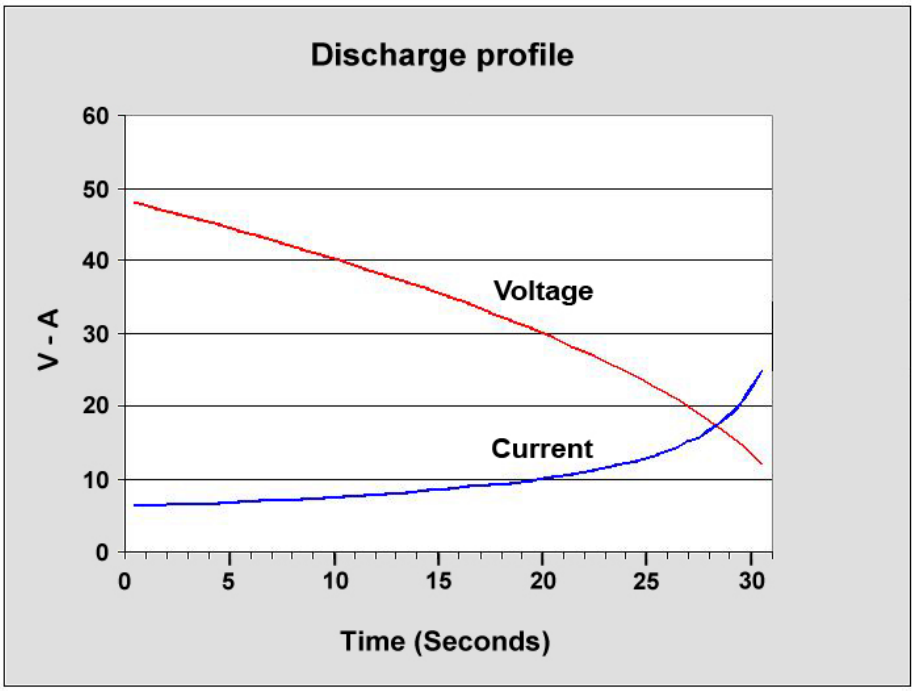

Figure 2-2 Discharging characteristics of a supercapacitor (source:[29])

As shown in Figure 2-2 the voltage drops linearly during discharge. An optional DC-DC converter maintains the wattage level by drawing higher current as the voltage decreases.

The charging time of a supercapacitor is quite similar to charging characteristics of an electrochemical battery, and the charge current is largely constrained by the charger's capacity [29]. Initial charging can be very rapid, while topping off the charge takes additional time. Supercapacitors are not susceptible to overcharge and do not require full-charge detection techniques.

Batteries, capacitors, supercapacitors all are energy storage devices where supercapacitors are in importance due to its quick charge discharge capability and high-power density. Considering batteries, when connecting with an external circuit, there is a movement of ions allowing a chemical reaction to happen. Due to the movement of ions, the current flows and an electric field develops [30]. The Ragone plot representing energy density vs. Power density has shown below in Figure 2-3.

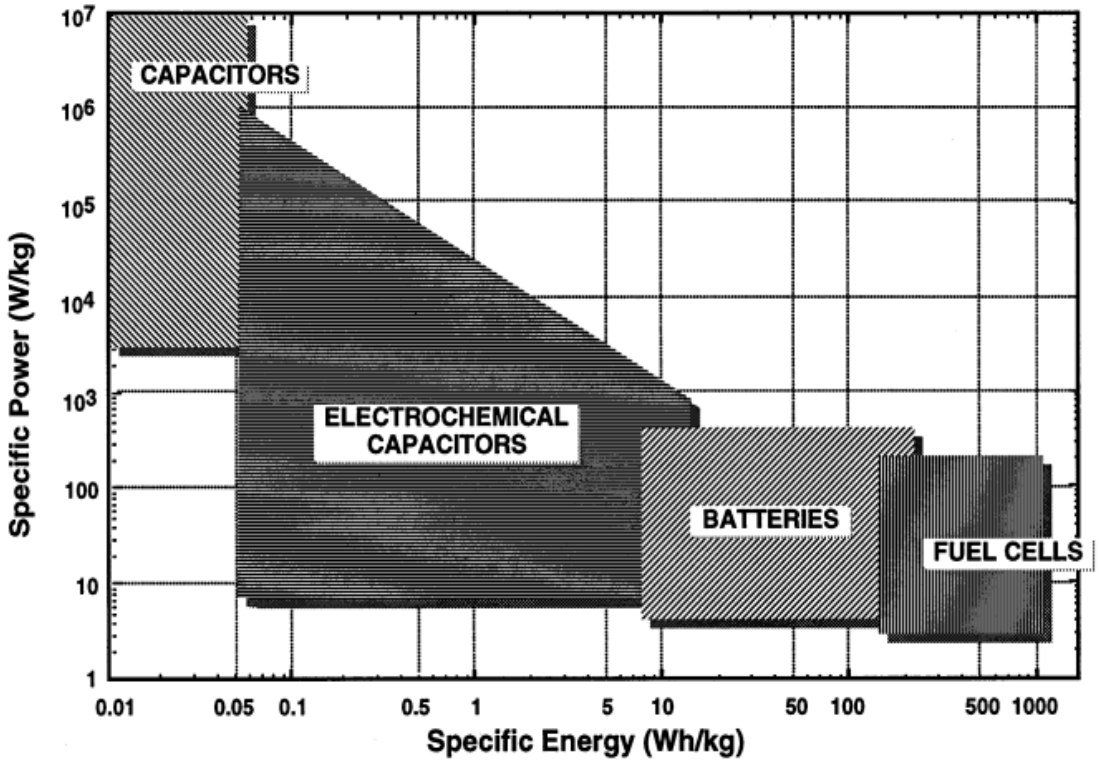

Figure 2-3 Ragone plot for various energy storage and conversion devices [30]

The Ragone plot is widely used for to compare the performance of energy storage devices [31]. Fuel cells can be seen on right side representing high energy density where capacitors can be seen on top left corner with high power density. Referring to the plot, supercapacitors have higher power density compared to batteries and fuel cells, but its energy density is lower than them.

Comparison of few parameters between conventional capacitor, supercapacitors and lithium-ion batteries are shown below in Table 2.1.

Table 2.1: Comparison between supercapacitors, capacitors, and batteries [32]

Parameters	Conventional capacitor	Supercapacitor	Battery (lithium-ion)
Energy storage	W-sec of energy	W-sec of energy	W-h of energy
Charge method	Voltage across terminals	Voltage across terminals	Constant current and constant voltage
Charge time	10^{-3} – 10^{-6} s	1 – 10 s	10 – 60 min
Cell voltage	6 – 800 V	2.3 V – 2.75 V/cell	1.2 V – 4.2 V/cell
Specific energy (Wh/kg)	0.01 to 0.05	1 to 5	8 to 600
Specific power (W/kg)	< 100,000	Up to 10,000	1000–3000
Charge/discharge efficiency	> 0.95	0.85 – 0.98	0.7 – 0.85
Cycle life	> 500,000	1 million	500 and higher
Operating temperature	− 20 to +100 °C	− 40 to +85 °C	− 20 to +65 °C
Form factor	Small to large	Small	Small to large
Lifetime	> 100 k cycles	> 100 k cycles	150 to 1500 cycles
Weight	1 g to 10 kg	1 to 2 g	1 g to > 10 kg

Batteries can be used in applications which needs to store a large amount of electricity and supercapacitors which are used in buffer energy systems advantageous in power peak demands.

A supercapacitor can be charged and discharged almost indefinitely. Supercapacitors experience minimal wear and tear from cycling compared to electrochemical batteries, which have a limited cycle life. Additionally, they have high capacitance retention which is around 80 percent of their original capacity even after 10 years under normal conditions. However, their lifespan can be shortened by exposure to higher-than-specified voltages.

Supercapacitors are also more tolerant of extreme temperatures, which is an area where batteries often struggle.

On the downside, supercapacitors exhibit a significantly higher self-discharge rate compared to electrostatic capacitors and slightly higher than electrochemical batteries, due to the organic electrolyte. A supercapacitor typically discharges from 100 to 50 percent in 30 to 40 days, whereas lead-acid and lithium-based batteries self-discharge at a rate of about 5 percent per month.

Supercapacitors are broadly categorized into two main types based on their charge storage mechanisms: electric double-layer capacitors (EDLCs) and pseudocapacitors. Electric Double-Layer Capacitors (EDLCs): EDLCs store energy through the electrostatic accumulation of charges at the electrode surfaces. These capacitors utilize high surface area carbon materials such as activated carbon, carbon nanotubes, or graphene to maximize the available surface area for charge storage [11]. The process involves the formation of an electric double layer at the interface between the electrode and the electrolyte, where ions from the electrolyte are adsorbed onto the surface of the electrode.

Pseudocapacitors: Pseudocapacitors, on the other hand, store energy through fast and reversible faradaic reactions (redox reactions) involving the transfer of electrons between the electrode and the electrolyte [33]. These reactions occur on the surface or within the bulk of materials such as transition metal oxides (e.g., ruthenium oxide, manganese oxide) or conducting polymers (e.g., polyaniline, polypyrrole). Pseudocapacitors generally offer higher energy densities than EDLCs due to the involvement of redox reactions in addition to electrostatic charge storage.

The unique properties of supercapacitors make them highly versatile and suitable for a wide range of applications such as portable electronics, electric vehicles, renewable energy systems and Power Backup and Uninterruptible Power Supplies.

Supercapacitors are used in devices such as smartphones, laptops, and wearable technology, where they provide quick bursts of power, supplementing the primary battery and extending device performance and battery life [34]. And in electric vehicles, supercapacitors are employed in regenerative braking systems to capture and store energy

that would otherwise be lost as heat [35]. This stored energy can then be used to assist in acceleration, improving overall efficiency and reducing wear on the battery.

Considering renewable energy systems, supercapacitors are integrated into solar and wind energy systems to stabilize power output and store excess energy generated during peak production periods. They provide rapid response to fluctuations in energy supply and demand, enhancing grid stability and reliability. Moreover, in power backup and uninterruptible power supplies (UPS), supercapacitors are used in UPS systems to provide instantaneous power backup during short-term power outages or voltage sags, protecting sensitive equipment from power interruptions.

Supercapacitors offer several advantages over traditional energy storage systems, making them highly beneficial for various applications. Their high-power density delivers energy at a much faster rate than batteries, making them ideal for applications requiring quick bursts of power. Also, they can be charged and discharged in seconds to minutes, compared to hours for batteries.

Moreover, they have shown to have a long cycle life and exhibit exceptional cycle stability, often enduring millions of charge-discharge cycles with minimal capacity loss. This contrasts sharply with the limited cycle life of conventional batteries. Supercapacitors are also able to maintain performance over a wide temperature range, making them suitable for use in extreme environments.

2.2 Electrode Materials for Supercapacitors

The performance of supercapacitors is largely dependent on the electrode materials used. This thesis aims to provide a comprehensive review of the various electrode materials employed in supercapacitors, focusing on their characteristics, advantages, and limitations. Electrode materials for supercapacitors can be broadly classified into three categories: carbon-based materials, metal oxides, and conducting polymers. Each category possesses distinct electrochemical properties that contribute to the overall performance of the supercapacitor. Activated carbon, carbon microspheres, carbon fibers, carbon nanotubes and graphene are the widely used carbon materials for supercapacitor electrode.

- Activated Carbon: This is a highly porous form of carbon with a large surface area. Its microporous structure allows for high adsorption capacity, making it excellent for use in supercapacitors where ions can readily adhere to its surface.
- Carbon Microspheres: These are spherical carbon particles with diameters typically ranging from tens of nanometers to several micrometers. Their uniform size and shape make them useful in various applications, including as electrode materials in supercapacitors.
- Carbon Fibers: These are composed primarily of carbon atoms bonded together in a crystalline alignment, resulting in high tensile strength and stiffness. In supercapacitors, carbon fibers are often used to create electrodes with enhanced mechanical properties.
- Carbon Nanotubes (CNTs): These are cylindrical nanostructures made of carbon atoms arranged in a hexagonal lattice. CNTs possess extraordinary electrical conductivity and mechanical strength, making them ideal candidates for supercapacitor electrodes.
- Graphene: In graphene a single layer of carbon atoms arranged in a two-dimensional honeycomb lattice, exhibits remarkable electrical conductivity, high surface area, and mechanical strength [36]. Graphene-based electrodes have demonstrated exceptional performance in terms of capacitance and energy density. The major challenge with graphene is its scalable production and the aggregation of graphene sheets, which can reduce the effective surface area.

Each of these carbon-based materials offers distinct advantages, and research have been continued to explore ways to optimize their properties for improved supercapacitor performance, such as increasing energy density and cycling stability [37], [38], [39].

Among these different materials used for supercapacitor electrodes, metal oxides also have garnered significant attention due to their high theoretical capacitance, excellent electrochemical stability, and diverse redox properties [40]. Ruthenium oxide (RuO_2), manganese oxide (MnO_2), nickel oxide (NiO), cobalt oxide (Co_3O_4) and vanadium oxide (V_2O_5) are some common metal oxides used in supercapacitors. Considering these metal oxide electrode materials, RuO_2 is considered a benchmark material for supercapacitor

electrodes due to its exceptional capacitance, high electrical conductivity, and excellent cyclic stability. However, its high cost and toxicity limit its widespread application.

MnO_2 is a cost-effective alternative with multiple valence states, which contributes to its high pseudocapacitance. It also exhibits good electrochemical performance and environmental benignity [41]. However, its relatively low electrical conductivity necessitates the use of conductive additives or composite materials. NiO is another promising material characterized by its high theoretical capacitance and good electrochemical stability. It is often used in hybrid capacitors where it is paired with carbon-based materials to improve overall performance.

Moreover, Co_3O_4 shows high capacitance and good cycling stability. It is capable of fast charge-discharge rates, making it suitable for high-power applications. However, similar to MnO_2, its low electrical conductivity is a challenge that needs to be addressed. Considering V_2O_5, it offers a unique layered structure that facilitates ion intercalation, leading to high capacitance values. It also demonstrates good electrochemical reversibility and stability.

Regarding the advantages of metal oxides in supercapacitors, they have high theoretical capacitance primarily due to their ability to undergo multiple oxidation states, which facilitates a higher charge storage capacity [42]. Also, the pseudocapacitive behavior of metal oxides arises from reversible redox reactions at the electrode-electrolyte interface. This redox activity enhances the charge storage mechanism, allowing for higher energy densities compared to electric double-layer capacitors (EDLCs). Further, metal oxides generally demonstrate excellent electrochemical stability, which is crucial for maintaining performance over long cycling periods. Materials like RuO_2 are known for their robust stability even under high voltage conditions.

Regardless of all the advantages listed above, many metal oxides, despite their high capacitance, suffer from low electrical conductivity [43]. To overcome this, researchers have developed composite materials combining metal oxides with conductive substrates such as carbon nanotubes (CNTs), graphene, or conductive polymers. Also, volumetric changes during redox reactions can lead to structural degradation of the metal oxide electrodes. Strategies such as nano structuring (e.g., creating nanoparticles, nanowires, or

nanoflakes) and doping with other elements have been employed to enhance structural stability.

Recent research has focused on developing hierarchical nanostructures, which combine different metal oxides or metal oxides with carbon-based materials to leverage the synergistic effects. For example, ternary composites such as $NiCo_2O_4$/NiO, and hybrid materials like MnO_2/graphene, have shown enhanced capacitance and stability. Another promising approach is the incorporation of metal oxides into flexible and wearable supercapacitors. Materials like MnO_2 and V_2O_5 are being integrated into flexible substrates to develop next-generation energy storage devices for portable electronics.

2.3 Carbon as Electrode Materials for Supercapacitors

Carbon-based materials discussed above have gained significant attention in various fields due to their unique properties and abundance. In the realm of energy storage, such as supercapacitors, carbon-based materials offer several advantages including high surface area, excellent electrical conductivity, and chemical stability [44].

Among the electrode materials discussed above, carbon microspheres have been proven to be the ideal electrode material due to several characteristics that make them attractive for supercapacitor applications. Their high specific surface area, often achieved through careful control of synthesis methods, provides ample active sites for ion adsorption, which contributes to high capacitance [45]. Additionally, their spherical morphology promotes efficient ion diffusion, enhancing the charge/discharge rates of supercapacitors.

Moreover, carbon microspheres can be engineered to have tailored pore structures and surface chemistries, further optimizing their electrochemical performance. These features contribute to high specific capacitance, which measures the amount of charge that can be stored per unit mass or volume of the electrode material.

Furthermore, the high capacitance retention of carbon microspheres over multiple charge/discharge cycles is crucial for the long-term stability and durability of supercapacitors. This characteristic ensures that the device maintains its energy storage

capacity over extended periods of use, making carbon microspheres a promising choice for practical applications.

However, the ideal electrode material should be selected depending on specific requirements such as cost, scalability, and performance metrics tailored to the intended application. Nonetheless, carbon microspheres undoubtedly represent a compelling option within the broader spectrum of carbon-based materials for supercapacitor electrodes.

The properties of carbon electrode materials are crucial in determining the performance of electrochemical devices such as batteries, supercapacitors, and fuel cells. This includes both chemical and physical properties of these devices such as [46]:

- Surface Functional Groups: The presence of functional groups on the surface of carbon materials can influence the electrochemical reactivity. Functional groups like carboxyl, hydroxyl, and others can provide active sites for reactions, affect electron transfer rates, and influence the adsorption of reactants or electrolytes. For instance, an increase in oxygen-containing groups can enhance wettability and ion accessibility, improving the capacitance in supercapacitors [47], [48].
- Surface Roughness: Rough surfaces increase the surface area available for electrochemical reactions. A higher surface area typically leads to greater capacitance and energy storage capacity. However, extremely rough surfaces might hinder the uniform flow of ions, impacting the efficiency and rate capabilities of the device [2], [49].
- Porosity: It is a critical factor, particularly in applications like supercapacitors and batteries where ion transport plays a significant role in device performance. Higher porosity can allow for more efficient ion diffusion through the electrode, increasing the rate of charge and discharge. Microporosity contributes to high surface area, beneficial for charge storage, whereas macroporosity assists in reducing transport distances for ions and electrons [2], [50].
- Surface Wettability: Wettability affects how well an electrolyte permeates the electrode material. Better wettability ensures that the electrolyte can access more of the electrode's surface area, enhancing the electrochemical interactions and, consequently, the performance of the device. Hydrophilic surfaces, which attract

water-based electrolytes, can significantly improve ion transport and electrode utilization [51], [52].

2.4 Fabrication of Carbon Microspheres

The fabrication of carbon microspheres typically involves the carbonization of organic precursors under controlled conditions. The synthesis process begins with the selection of appropriate carbon-rich precursors, such as glucose, sucrose, phenol-formaldehyde resin, or biomass-based compounds. Hydrothermal carbonization (HTC) is popular approach for using saccharide-based precursors due to its simplicity, cost-effectiveness, and environmentally friendly nature.

Several methods have been developed to produce carbon microspheres, including chemical vapor deposition (CVD), hydrothermal carbonization, and template assisted synthesis. While some of these techniques, such as high-pressure carbonization, might increase production rates, they frequently demand operating pressures of up to 10 MPa and may result in lesser purity carbon spheres. Moreover, depending on the desired particle size and structure, chemical vapor deposition (CVD) and template-assisted synthesis are equally viable options. And chemical vapor deposition benefits in terms of process versatility.

2.4.1 Chemical vapor deposition

Several studies have demonstrated the effectiveness of chemical vapor deposition (CVD) methods for the synthesis of carbon microspheres with variable properties. Successful production of carbon nanospheres ranging from 400 to 2000 nm in diameter has been reported employing a catalytic CVD approach using kaolin-supported transition metal salts (e.g. Fe, Co, Ni) and acetylene gas [53]. The use of kaolin as a catalyst support facilitated high-yield synthesis at relatively moderate temperatures (650–900 °C). In contrast to that, another study has explored a non-catalytic CVD method and has shown that gas composition, mainly the presence of hydrogen, significantly influenced the size and morphology of carbon microspheres, which were smaller (200–350 nm) and more uniform at optimized conditions [54]. Further, studies have been conducted to extend the

utility of non-catalytic CVD through the synthesis of boron-doped hollow carbon spheres using acetylene and trimethyl borate in the presence of Ar/H_2, and this study has highlighted the ability to introduce heteroatom doping and hollow structures through control of gas composition and post-synthesis treatment [55]. Together, these studies underscore the versatility of CVD techniques for tailoring the structure, composition, and functionality of carbon spheres for diverse applications.

The effectiveness of CVD based synthesis relies greatly on several factors, including the nature of the catalyst, the substrate, the reaction temperature, and the reactant flow conditions. Transition metal catalysts, such as iron compounds, are widely used to promote carbon structure formation due to their catalytic efficiency and the cost effectiveness. Moreover, recent studies has explored the effectiveness of silicon wafers as substrates due to their thermal stability and compatibility with the process. Considering silicon wafers, p-type silicon (100) substrates have been widely employed.

Chemical vapor deposition technique can further be divided in to three categories, known as Catalytic CVD, non-catalytic CVD and template assisted CVD where, each method has its own strengths and limitations. Hydrothermal Carbonization

Hydrothermal carbonization (HTC) has been widely used as a sustainable method for the conversion of biomass into carbon-rich materials under relatively mild conditions. In several studies, various organic precursors such as glucose, cellulose, and carboxymethyl cellulose have been subjected to HTC, typically at temperatures ranging from 120 °C to 250 °C in sealed autoclaves, resulting in the formation of carbon microspheres. Hydrothermal treatment of glucose in the presence of metal salts has been done in recent studies to produce carbon spheres functionalized with metal ions. Further, the shell thickness and surface area have been controlled by adjusting the ration between the substrate and metal ratio [56].

Moreover, studies have been conducted to investigate the HTC of cellulose, where the biomass has been transformed into highly condensed and functionalized carbon microspheres through dehydration and aromatization reactions. Furthermore, these carbon microspheres have exhibited core–shell structures, with oxygenated functional groups such as hydroxyl, carbonyl formed during the process [57]. The carbonization process has

been observed around 220 °C, and the degree of carbon retention and structural condensation has been confirmed through elemental analysis, XRD, FTIR, and XPS.

Hydrothermal carbonization of carboxymethylcellulose and urea have been reported to yield nitrogen-doped conductive carbon microspheres and water-soluble fluorescent carbon nanodots (CNDs) [58]. Furthermore, CNDs with conductive properties and, photoluminescent CNDs with pH-sensitive properties and high water dispersibility have been obtained.

2.4.2 Template assisted synthesis

Template-assisted synthesis can be identified as a widely used method for fabricating carbon microspheres with controlled size, shape, porosity, and surface properties. This method involves the use of templates that guide the formation of carbon materials during synthesis. Additionally, carbon microspheres tailored for specific applications such as supercapacitors, batteries, catalysis, and drug delivery can be fabricated by manipulating the template structure and synthesis conditions [59].

Template-assisted methods offer precise control over particle size, porosity, and structural uniformity, making them suitable for applications in energy storage, catalysis, drug delivery, and adsorption [60]. However, the method involves multiple synthesis steps and use of hazardous chemicals, which must be carefully managed for sustainable and scalable production.

The typical procedure involves the impregnation or coating of the template with a carbon precursor such as resorcinol-formaldehyde resin, glucose, sucrose, or other polymerizable organic compounds [61]. Further, it is followed by a carbonization step, which is usually conducted in an inert atmosphere at elevated temperatures ranging from 600 °C to 1000 °C, which converts the precursor into a carbonaceous material. Subsequently, the template is removed through chemical etching or thermal decomposition which generates well defined carbon microspheres.

Among the techniques reviewed, chemical vapor deposition can be identified as a potentially strong method for the fabrication of carbon microspheres in the current

research due to its superior control over particle morphology, high purity of the resulting structures, and ability to produce uniform carbon spheres with tailored diameters [62]. Unlike hydrothermal carbonization, which often requires post-treatment steps to enhance material properties, or template-assisted synthesis, which involves complex template removal procedures, CVD offers a cleaner, template-free route with scalable potential. Furthermore, catalytic CVD holds an importance due to low processing temperatures using transition metal catalysts and enables precise manipulation of the microsphere characteristics, making it well-suited for the intended applications.

2.5 Properties of carbon microspheres

Properties of carbon microspheres plays a vital role in their functional performance across a broad spectrum of applications. Key structural features such as particle size, porosity, surface area, and degree of graphitization significantly affect their properties. For example, higher surface area and porosity enhances ion adsorption and transport, making the carbon microspheres ideal for energy storage devices like supercapacitors. Further, the presence of micropores (<2 nm) significantly enhances specific surface area, which is critical for adsorption and energy storage [63]. Mesopores (2–50 nm) facilitate efficient ion and molecule transport, while macropores (>50 nm) improve bulk diffusion. Moreover, spherical and uniform morphology in carbon microspheres improves packing and flow characteristics, which are beneficial in drug delivery and catalysis.

Surface chemistry is equally important, as the presence of functional groups such as hydroxyl (–OH), carboxyl (–COOH), and amine (–NH_2) can change the hydrophilicity, chemical reactivity, and interfacial compatibility of carbon microspheres with various media. These surface functional groups facilitate dispersion in aqueous or polymeric environments and serve as active sites for chemical interactions and biological binding. The degree of graphitization, defined by the arrangement and order of carbon atoms, further determines the electrical and thermal conductivity of the microspheres [64]. Highly graphitized carbon microspheres exhibit superior electrical conductivity, which is desirable in applications such as battery electrodes and supercapacitors, while amorphous

structures may offer higher chemical reactivity and better adsorption characteristics due to the presence of disordered carbon domains.

Moreover, advanced structural designs, including hollow microspheres, core–shell architectures, and surface modified systems enable further tuning of key properties such as density, mechanical stability, and functional loading capacity [65]. These features are particularly beneficial in applications requiring lightweight materials with high specific activities. By strategically controlling synthesis parameters, such as precursor selection, strategy of templating, and activation conditions, it is possible to engineer the microstructure and surface characteristics of carbon microspheres to meet specific application requirements [66].

2.6 Heterogeneity of carbon electrode materials

The heterogeneous nature of carbon materials mean arise when the above discussed properties vary widely even within the same batch of material. Manufacturers and researchers often work to optimize these characteristics through various treatments and processing techniques to tailor carbon electrodes for specific applications and performance requirements.

Heterogeneous structural characteristics of carbon microspheres have been observed in samples synthesized via Ultrasonic Spray Pyrolysis (USP). Despite being produced under controlled conditions, considerable variation in morphology, pore structure, and internal architecture has been evident in the samples [67]. Microscopic analyses of carbon microspheres have revealed that pore size, wall thickness, and surface roughness varied among particles, even within the same batch. As a result of this, the microspheres have exhibited complex and non-uniform internal structures, leading to a high degree of heterogeneity. This structural variability was considered significant, as it influenced key material properties such as surface area, porosity, and electrochemical performance. Figure 2-4 shows the surface morphology of carbon microspheres under SEM microscopy.

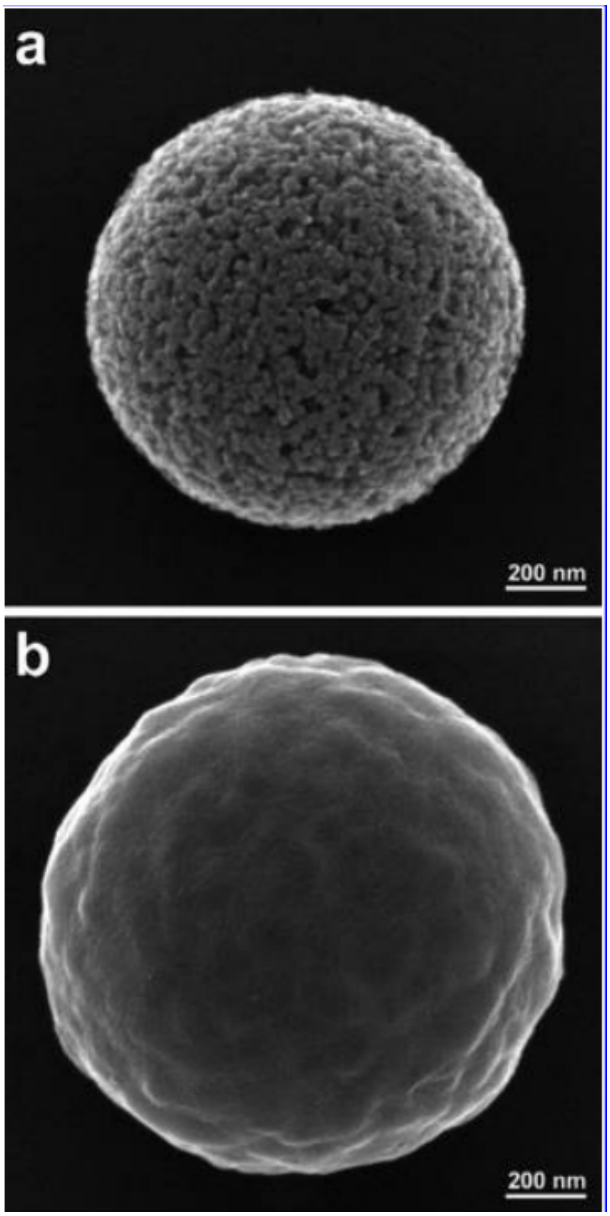

Figure 2-4 SEM images showing the morphology of carbon microspheres [68]

As discussed above, heterogeneity in carbon microspheres primarily results from variations in size, weight, and the distribution of surface functional groups [46]. These differences directly influence the surface chemistry, leading to diverse and heterogeneous surface properties within the same material. Such heterogeneity can disrupt the uniformity in electrochemical characteristics, which is crucial for the optimal performance of devices like supercapacitors [1], [69].

In supercapacitor applications, homogeneous electrodes are particularly favored due to their ability to ensure a smooth and consistent charge distribution across the electrode's surface. This uniformity is essential for achieving not only high energy density but also for enhancing the overall efficiency and durability of the supercapacitor. The homogeneity of the electrode material facilitates equal participation of all areas in the electrochemical reactions, thereby maximizing the device's performance and lifecycle [70].

2.7 Separation of heterogeneous carbon microspheres

The separation of carbon microspheres exhibiting heterogeneous properties is essential for enhancing their performance, particularly in energy storage applications, by preventing uneven charge distribution within carbon materials [71], [72]. To achieve size-based separation of carbon materials, various methods such as filtration, centrifugal separation, gravity flotation, inertia force, and magnetic force are commonly employed [73], [74], [75], [76], [77], [78]. These methods are effective for distinguishing particles based on physical dimensions and mass. However, they fall short when dealing with microspheres that share the same size and weight but have differing surface properties. This type of separation is challenging yet crucial for improving the energy storage efficiency and overall performance of supercapacitors.

Advanced techniques such as dielectrophoresis (DEP), electrophoretic separation, surface-selective adsorption and desorption, chromatographic techniques, microfluidic devices and selective chemical functionalization can be employed to separate particles based on their surface properties.

Electrophoretic Separation is a separation technique using an electric field to move charged particles based on their electrophoretic mobility, influenced by surface charge. It is a method effective for differentiating microspheres with varying surface charges, enabling precise separation [79]. Whereas dielectrophoresis (DEP) exploits differences in particle polarizability in a non-uniform electric field, causing particles to move towards regions of higher or lower field intensity. This is being widely applied in separation of microspheres with distinct dielectric properties related to their surface characteristics [80].

Moreover, surface selective adsorption and desorption involves chemical agents that selectively bind to or release from microsphere surfaces based on specific surface properties [81]. It is being widely applied in applications where differentiation and separation is done based on unique surface chemistries. Utilization of microfluidic devices can be done in micro-scale channels to exploit differences in particle interactions with channel walls or flowing fluids and this provides precise control over separation based on subtle variations in surface properties [82].

Selective Chemical Functionalization is a technique which introduces functional groups that selectively react with specific surface features of microspheres [83]. This enables targeted binding and separation of microspheres with specific surface characteristics. Spectroscopic Methods Coupled with Sorting is a method which identifies surface properties using techniques like Raman or infrared spectroscopy, followed by sorting mechanisms [84]. This method provides detailed analysis of surface properties, facilitating accurate separation.

Chromatographic Techniques can be identified as a useful method in separating particles based on their interactions with a stationary phase in chromatography, such as hydrophobic interaction or ion-exchange chromatography [85]. This method is applicable for separating microspheres by surface hydrophobicity or charge differences.

Achieving effective separation of carbon microspheres with heterogeneous surface properties is critical for optimizing the performance of supercapacitors and other energy storage devices. By employing advanced techniques tailored to surface property differentiation, it is possible to achieve a higher degree of uniformity, enhancing the overall efficiency and functionality of these materials in various applications.

2.8 Microfluidic based separation methods

Microfluidic systems have been widely used in various kinds of applications due to its reduced size and the consumption of low sample volumes which makes them suitable for limited and precious samples. Also, their smaller dimensions allow rapid separation often in seconds. Further, employment of advanced systems such as chromatography along with microfluidic systems facilitates analysis with higher sensitivity [86]. Microfluidic systems

propose integrated platforms which enable the easy handling and analysis of biological samples, which minimizes the sample requirements significantly. For an example, cells within biological samples can be lysed within microchannels and undergo the extraction and analysis of biomolecules such as DNA, mRNA, and metabolites within the channel [87], [88], [89], [90]. On-chip liquid chromatography systems can be effectively integrated directly within the channel with various detection systems such as mass spectrometry [91], [92], fluorescence microscopy [93], and conductivity detectors [94]. When used in combine with a fluorescent microscope, the separation process can be easily visualized and monitored in real time. Microchip liquid chromatography is versatile, capable of biomolecule separation and the separation of biological particles [95], [96].

The liquid chromatography separation can be categorized into five classes based on their separation mechanisms, affinity based, adsorption based [97], [98], size exclusion based [99], hydrodynamic based, and ion exchange based columns, where both size exclusion and hydrodynamic liquid chromatography separates particles according to their size. Figure 2-5 illustrates the domains of application with different types of liquid chromatography systems.

Considering adsorption-based separation, the technique relies on partitioning analytes between the stationary phase and the mobile phase with reversed phase liquid chromatography being the widely used method [100], [101]. Microfabricated pillar arrays fabricated with silicon oxide, etched using photolithography offers a high separation efficiency for compounds like coumarin derivatives [102]. Monolithic columns which are porous stationary phases formed directly within microchannels are versatile, supports the analysis of proteins, peptides, and small molecules like neurotransmitters [103], [104]. Some column designs can combine sample enrichment columns with analytical columns and nano spray tips for efficient proteomic analysis. This integration reduces sample loss and enhances throughput [105].

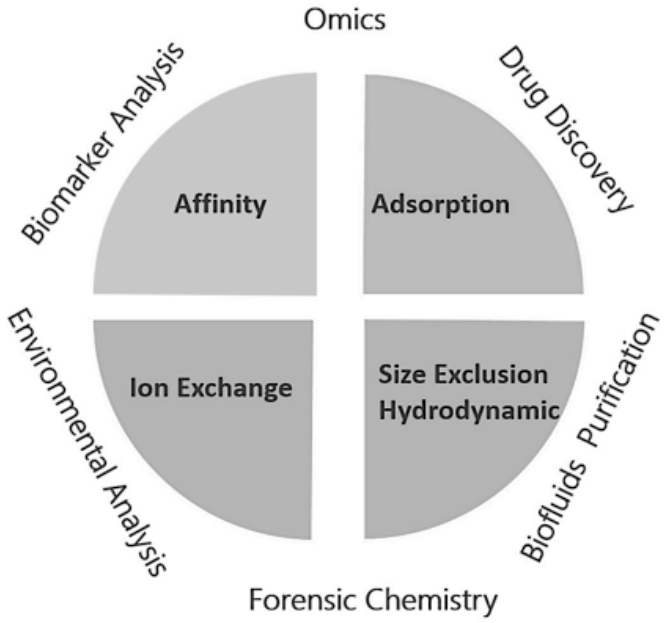

Figure 2-5: Domains of application with different types of liquid chromatography systems

Size exclusion and hydrodynamic based separation methods can be used to separate analytes based on size differences. The Size Exclusion Chromatography (SEC) uses porous beads to separate molecules based on size [106]. For example, SEC can be utilized to purify proteins and for the analysis of polymers on microfluidic platforms. The hydrodynamic chromatography technique exploits the parabolic flow profile in microchannels to separate particles by size. Larger particles travel faster in the center of the flow stream, while smaller ones move closer to the channel walls [107], [108]

Further the ion-based separation methods separate charged species using ionic interactions. Considering ion exchange columns, hydroxyapatite particles are packed in microchannels to purify biomolecules like viruses from biological samples, where the ionic strength of the buffer controls elution [109], [110] The paper-based ion chromatography includes ion-exchange paper microfluidic devices (μPADs) for low-cost, portable analysis. For example, anion-exchange μPADs can quantify calcium or acidity in samples like wine or serum [111]In addition to these, other separation mechanisms are there, that include unique approaches tailored for specific applications. In Extended nanospace channels, the channels as narrow as 10–100 nm are used for attoliter scale

analysis. The electric double layer formed within these channels enables the separation of charged species, enhancing efficiency for small volume applications [112], [113].

Moreover, Gradient elution can be utilized to separate complex mixtures, stepwise gradients are introduced using specialized microdevices like T-nanomixers [114], [115]. This technique supports the high-throughput analysis of biomolecules such as amino acids. A summary of few applications of microfluidic based chromatography separations are depicted in Table 2.2. Furthermore, affinity-based separation can be highlighted as the most widely used technique which works on specific molecular interactions between a ligand on the stationary phase and the target molecules in the analytes, which was identified to be the optimum technique for the separation addressed and is discussed in detail in the next section.

Table 2.2: Examples for microfluidics-based chromatography separation applications

Separation Mechanism	Stationary Phase	Mobile Phase	Analytes	Ref
Affinity	TiO_2 - ZrO_2	Acidic/Basic mobile phase: FA, TFA, NH_4OH	Phosphopeptides	[116]
Affinity	TiO_2 nanotube array	Loading buffer: TFA and ACN	Phosphopeptides	[117]
Affinity	TiO_2-ZrO_2 film	Loading buffer: 50% ACN and 1% TFA	Phosphopeptides	[118]
Affinity	MNPs modified with bis-Zn-DPA	Diluted RBC solution	Escherichia coli	[119]
Affinity	Anti-EpCAM	Healthy blood	Circulating tumor cells	[120]
Ion	Carboxyl groups on cellulose paper	AA and DA buffer solutions	Ascorbic acid, dopamine hydrochloride	[111]
Affinity	Immunomagnetic beads	Plasma	Exosomes	[121]
Affinity	DNA aptamers	PBS binding buffer	Cancer cells	[122]
Size exclusion	Sephadex G25 beads	-	Proteins	[108]
Adsorption	Polymethyl acrylate	DI water	Neurotransmitters	[103]

2.8.1 Affinity based microfluidic separation

Affinity-based microfluidic separation is a powerful technique that utilizes specific molecular interactions to selectively isolate and analyze target compounds within complex mixtures. This method relies on the principle of affinity binding, where ligands such as antibodies, aptamers, oligonucleotides, or metal complexes interact with target analytes through highly specific and reversible interactions [123]. By integrating this approach into microfluidic platforms, researchers have developed compact, efficient, high-throughput systems particularly suited for analyzing biological samples.

As discussed above, the miniaturization enabled by microfluidic devises for affinity-based separation offers several advantages, including reduced sample and reagent consumption, enhanced reaction kinetics due to shorter diffusion distances, and precise control over separation processes. Moreover, the ability to integrate multiple functional units, such as sample preparation, separation, and detection, into a single device creates a streamlined workflow, ideal for clinical diagnostics, drug discovery, and proteomics [124]. Affinity-based microfluidic systems have been applied to a wide range of analytes, from circulating tumor cells and nucleic acids to proteins and metabolites [125]. These systems rely on immobilized ligands within microchannels or beads to capture targets with high specificity, even in complex biological matrices such as blood, serum, or cell lysates [126]. Recent advancements in fabrication techniques, such as soft lithography, plasma bonding, and 3D printing, have further enhanced the versatility and scalability of these platforms. A summary of fabrication methods and applications concerning on chip liquid chromatography systems are discussed here.

2.8.1.1 Oxidized metal affinity separation

Oxidized metal groups are used as stationary phases in oxidized metal affinity separation techniques. Titanium dioxide (TiO_2) has become widely used material for phosphopeptide enrichment in proteomics due to its strong affinity for phosphate groups. This interaction allows highly specific binding of phosphorylated peptides, making TiO_2 an effective stationary phase for selective enrichment. In these systems, the stationary phase is

typically coated or modified with a TiO_2 layer to facilitate binding. Protein digests are introduced into the column using an acidic mobile phase, which enhances the interaction between TiO_2 and phosphate groups. During the process, interfering peptides and background compounds are effectively washed away, while phosphopeptides remain bound to the stationary phase. This targeted enrichment significantly enhances the sensitivity and specificity of downstream proteomic analyses, enabling a comprehensive study of protein phosphorylation, a key post-translational modification in various cellular processes.

Figure 2-6 illustrates the process for fabricating polymeric microfluidic devices with standard microelectromechanical systems (MEMS) technology namely lithography of a TiO_2–ZrO_2 based microchip liquid chromatography system for phosphopeptide analysis. Further their study has been able to show that microfluidic device can separate phosphopeptide standard mixtures as well as analyze the phosphopeptides from protein digests [116].

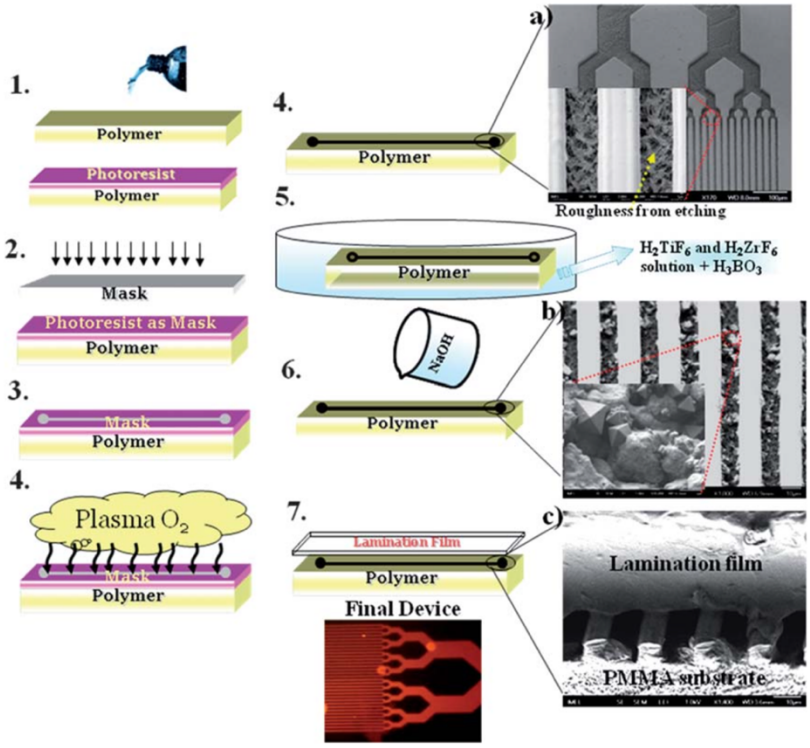

Figure 2-6: Liquid deposition method for preparing TiO_2–ZrO_2 based microfluidics for phosphopeptide enrichment

The microfluidic affinity chromatography chip exhibited high recovery rates and the capability to efficiently handle small sample volumes, and further improvements to the analysis performance can be done by tuning the structure of the metal oxide. Metal complexes also symbolize another important class of ligands that can be used in affinity separation. Metal complexes are formed when an electron donor compound combines with metal ions, and these complex ligands can be employed in targeted separation of molecules. The synthesis of zinc-coordinated bis (dipicolylamine) coated nanoparticles and their use to capture bacteria and purify blood within microfluidic chips has been studied [119]. These nanoparticles have shown to bind to anionic phospholipids present on bacterial membranes, and these nanoparticles can be removed effectively using magnetic fields. Thus, the system demonstrate in the study is highly beneficial in treating patients with bloodstream infections.

2.8.1.2 Antibody based microfluidic separation

Antibody-based microfluidics has been extensively studied given the interaction between antibodies and antigens. Chromatography can be described as the separation of molecules based on the interactions between mobile phase and stationary phase [127]. Antibody-based microfluidics is widely used for the separation and analysis of cells, bacteria, and biofluids. The capture of circulating tumor cells (CTCs) from the blood of cancer patients is one of the prominent applications. CTCs are generated by the primary tumor and enters the bloodstream, facilitates cancer diagnosis and monitoring. Even in a scenario of having a low number of these cells in the blood streams, antibody-based microfluidics may still be able to capture them. There also has been other antibody-antigen based microfluidic devices applicable in separating the CTCs.

For an example, the adaptation of radial flow technique in isolating CTCs has been studied, where anti-EpCAM (epithelial cell adhesion molecules) antibodies coated on a bean shaped microfluidic chips were used as shown in Figure 2-7. These microfluidic chips have been shown to be useful in sorting multiple types of cells and with the combination of other detection techniques like Polymerase Chain Reaction (PCR) and mass spectrometry, multiple cells sorting microfluidic chips can be prepared for disease diagnosis [128][129].

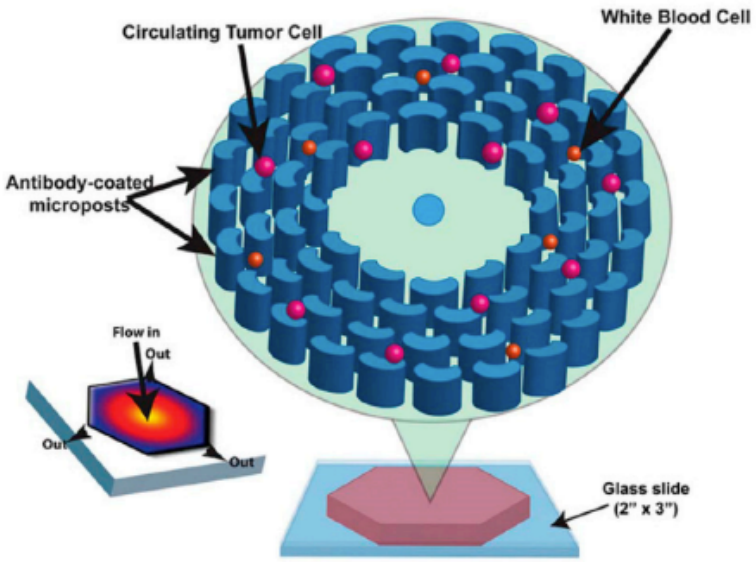

Figure 2-7: Schematic representation of microfluidics with bean-shaped micro channels

The antibody based microfluidic devices have also emerged as powerful tools in the analysis of vesicles, including exosomes and ectosomes. Exosomes are the extracellular vesicles less than 150 nm in diameter and are released during intercellular communication, thus can be used as a biomarker in cancer diagnosis. The specific exosome associated antibodies coated microchannels have been used to isolate exosomes and to extract the intravascular RNA [126]. Mutual arrangements with immunomagnetic bead technique can further improve the efficiency of microfluidic based exosome isolation. Polydimethylsiloxane (PDMS) fabricated magnetic microfluidic devices has also facilitated better quantification of exosomes by mixing the magnetic beads with exosomes where the antibody modified beads diagnose the exosomes. [121].

Isolation of exosomes and analysis of intravascular proteins has been done through microfluidic devices using pre-incubated antibody-coated magnetic beads [130]. Here the beads bonded with exosomes were retained withing the microfluidic device, and successively flushed with phosphate-buffered saline (PBS) to remove the blood cells. Then lysis was conducted, and the lysates were transferred to another microchamber on the chip, where the immunomagnetic beads capture the specific protein in lysates through detection reagents introduced to the chamber.

2.8.1.3 Aptamer based microfluidic separation

Aptamers are peptides that can specifically bind to target molecules and compared to antibodies they have distinctive advantages. Their synthesis time is shorter, and they can bind with large molecules as well as small molecules which is impossible with antibodies. Pairs of perpendicular PDMS microchannels have been used in capturing cancer cells and amplifying their DNA for gene mutation analysis, where one channel is allocated for capturing cells and the second channel is for DNA analysis [122]. These devices simplify the DNA analysis process and minimizes the sample consumptions. Aptamer based microfluidic devices loaded with anti-cocaine aptamers and gold nanoparticles has been used for cocaine detection. The unit is immersed in biofluids and if cocaine is there, it will gradually move to the area where anti-cocaine aptamers are loaded and will bind with them. Then the cocaine aptamer complex gradually moves to the area loaded with gold nanoparticles, and the color of gold nanoparticles will change from red to blue [131].

2.9 Diffusion based separation within microchannels

Diffusion is the primary mechanism considering mass transfer of nanoparticles in a variety of applications such as environmental engineering, biomedical diagnosis, targeted drug delivery, cosmetics, and food industry [132], [133], [134], [135], [136]. Therefore, understanding in the diffusion behavior of nanoparticles is prominent in all these applications to make them effective. Microchip separators are applicable for continuous and spontaneous separation of heterogeneous nanoparticles through differences in their diffusion behaviors determined by diffusion dynamics within microchannels [137], [138]. Better separations of nanoparticles within microchannels can be achieved by controlled manipulation of their diffusive transport.

Separation of heterogeneous nanoparticles has been done through various methods to manipulate the diffusion behavior, where nanoparticle surface modification has been widely used to control the diffusive transport [139], [140], [141], [142], [143]. These surface modifications require advanced technologies with complex fabrication processes, otherwise they cannot effectively manipulate the diffusion behaviors leading to separations [127], [128]. Active separation of nanoparticles through the variations on

magnetic properties, charge properties and, compressibility has been investigated where the selection of the external interferences can be done according to the differences identified between the nanoparticles [144]. These techniques have also been identified as a viable method in targeted drug delivery for cancer patients through the manipulation of diffusion behavior [145]. The diffusion coefficient plays a major role in diffusion applications and is a key variable which determines the diffusion efficiency. Diffusion is a phenomenon where mass transfer happens from higher concentrations to lower concentrations [146], and it can be in two major categories as collective diffusion, and self-diffusion.

The diffusion coefficient for collective diffusion is given by the Fick's law of diffusion, which describes the mass transfer driven by the concentration gradient [147], [148]. Here, collective diffusion occurs under the influence of adjacent nanoparticles, whereas self-diffusion refers to the movement of an individual nanoparticle, which remains unaffected by interparticle interactions due to the absence of nearby nanoparticles. The self-diffusion coefficient characterizes the random trajectory of a single tracer particle in the absence of a concentration gradient and is described by the Stokes-Einstein (SE) relation [149], [150]. In dilute systems, self-diffusion dominates as particles move independently, while in more concentrated suspensions, collective diffusion becomes increasingly significant due to hydrodynamic and interparticle interactions.

The application of Stokes-Einstein relation is valid only when the particle size is larger than the solvent molecule, while for particles and solvent molecules with similar sizes, empirical extensions on Stokes Einstein relation has been proposed [151]. Further, the application of these equations has narrowed to diffusion coefficient calculation for dilute solutions. For concentrated suspensions, the value of the collective diffusion coefficient differs from the self-diffusion coefficient due to interparticle interactions among neighboring nanoparticles. Although the diffusion of nanoparticles can occur via either collective diffusion or self-diffusion, collective diffusion is more common and occurs in most of the applications and separation processes. The diffusion coefficient for the transport of nanoparticles can be calculated using experimental results based on the theoretical models.

Spin echo nuclear magnetic resonance and dynamic light scattering has been employed to determine the self-diffusion coefficient experimentally [152], and capillary electrophoresis instrument combined with Taylor analysis model has been used for the determination of collective diffusion coefficient [149]. Although the diffusion coefficients calculated by these methods are accurate, the equipment needed are complex and expensive. Chip based microfluidic devices has gained a significant attention due to its capability in in-situ observation, low sample requirements and wastages, better mass transfer, and cost effectiveness. Considering the field of diffusion-based separations, microfluidic chips with well-engineered microchannels has demonstrated high efficiency in determining the diffusion coefficients [153], [154].

2.10 Evaluation and simulation of the effect of surface forces

As discussed above, microfluidic systems have revolutionized analytical and industrial processes by enabling precise control over fluid behavior at the microscale. Considering the separation of nanoparticles, separations driven by surface affinity have emerged as a powerful approach, and in combination with microfluidic systems it has major advantages such as, low sample consumptions, better control and in-situ observation. The study of separations based on surface forces necessitates a comprehensive understanding about fluid flow dynamics and physicochemical characteristics of the substances being separated. The simulation of the flow of nanoparticles benefits to get a better understanding about the diffusion behavior of these nanoparticles within microfluidic devices, thus the optimization of the separation can be enhanced with the involvement of simulation models.

The effects of varying Reynolds numbers and nanoparticle volume fractions on heat transfer, pressure drop, and entropy generation have been demonstrated using a computational fluid dynamics simulation model. The results have indicated that increasing the nanoparticle volume fraction enhances heat transfer, the friction factor, pumping power, and entropy generation [155]. Simulation models also have been developed to assess diffusion-induced stress in lithium-ion battery electrode particles under galvanostatic conditions, utilizing COMSOL Multiphysics 4.2 [156]. By incorporating

reconstructed particle geometries from micro/nano-CT, the study demonstrates how particle morphology significantly influences stress distribution and identifies regions prone to mechanical failure.

Furthermore, molecular dynamics simulations of nanoparticle diffusion have been conducted to examine the movement of nanoparticles in dense gases and liquids. Utilizing the Rudyak–Krasnolutskii (RK) potential, this study reveals significant deviations from traditional Einstein relations that govern Brownian particles, highlighting how diffusion coefficients are affected by nanoparticle material, size, and temperature [157]. The findings emphasize distinct nanoparticle behaviors in dense media and suggest updated theoretical models for their transport properties. Molecular dynamics simulations have been conducted to investigate nanoparticle diffusion at fluid interfaces and in bulk solvents. In bulk solvents, diffusion aligns with established theories. However, when nanoparticles adhere to interfaces, their motion becomes highly anisotropic, exhibiting significantly faster diffusion parallel to the interface than perpendicular to it [158]. This study offers insights into nanoparticle behavior at interfaces, which is relevant for applications such as catalysis and nanoparticle patterning. Simulating the diffusion behavior of spherical nanoparticles using Computational Fluid Dynamics (CFD) is beneficial to understand the transport phenomena and interactions of these particles within a fluid medium.

Computational Fluid Dynamics (CFD) simulations utilize various software tools tailored to specific research and industry needs. Prominent platforms like ANSYS Fluent, OpenFOAM, and Star-CCM+ are widely used in multiphysics modeling for fields such as aerospace, automotive, and energy [159], [160]. COMSOL Multiphysics integrates fluid dynamics with other physical domains, while specialized tools like NUMECA and FLOW-3D focus on turbomachinery and free surface flows, respectively. Cloud-based solutions like SimScale and integrated tools like SolidWorks Flow Simulation support rapid prototyping and product design. Platforms such as CFD++ and XFlow deliver high-fidelity simulations for extreme conditions and transient phenomena. Each software has unique strengths, enabling researchers to choose the best option based on project complexity, computational requirements, and industry applications.

The design, modeling, simulation and testing of a two-region micro-channel heat exchanger for onboard compressed natural gas cooling has been done employing engine coolant and refrigerant R134a as heat sinks in a dual-region design [160]. Numerical simulations and experimental tests have validated its performance, revealing efficient pressure drop predictions and flow distribution, with a cooling capacity exceeding that required for test conditions, thereby highlighting its potential for automotive applications. Further, the simulation of heat dissipation in rectangular micro-channels using water as the working fluid has been done aiming to enhance the thermal efficiency of micro-electro-mechanical systems (MEMS) [161]. Numerical simulations using ANSYS Fluent can be utilized to explore how varying aspect ratios and boundary conditions affect heat transfer and flow dynamics, demonstrating that higher aspect ratios stabilize Nusselt numbers and heat transfer characteristics. Key findings indicate that heat transfer is most efficient under four-wall boundary conditions, whereas one-wall boundary conditions yield the highest heat flux.

Moreover, the design and validation of a microfluidic chip for analyzing fluid dynamics and interactions within microscale channels through both experimental and computational methods have been done using ANSYS Fluent [162]. This study has investigated the behavior of two pH buffer solutions, emphasizing pressure drops and velocity profiles. The findings have validated the simulation model, demonstrating its utility in optimizing microfluidic designs for applications in medical diagnostics, food quality control, and the pharmaceutical industry.

CHAPTER 3

MATERIALS AND METHODS

This chapter details the methodologies employed for characterizing carbon microspheres and outlines the experimental procedures used to separate heterogeneous carbon microspheres using microfluidic systems. It further discusses the optimization of separation efficiency through the application of external forces. Additionally, it describes the simulation and modeling of surface force effects on separation, including the software setup and the modifications implemented to incorporate these forces via external algorithms.

3.1 Study on surface characteristics of carbon electrode materials

3.1.1 Fabrication of Carbon Microspheres

Among various methods discussed above for the synthesis carbon microspheres, Chemical Vapor Deposition (CVD) has emerged as a preferred technique due to its versatility, scalability, and the potential to yield uniform structures with controlled morphology under relatively mild conditions. In this work catalytic CVD approach was used for the synthesis of carbon microspheres using ion-based catalyst precursors deposited on p type silicon substrates [163]. The fabrication process includes substrate cleaning, catalyst deposition, and thermal treatment in a nitrogen atmosphere, followed by hydrocarbon gas introduction for carbon deposition as discussed below.

A p-type silicon (100) wafer with a 450 mm (18-inch) diameter was cut into square pieces which are 2cm × 2cm. The silicon was prepared for catalyst coating by first cleaning through soaking in acetone, followed by ultrasonic cleaning in deionized water at 40°C for 10 minutes, then in methanol for 5 minutes, and again rinsed with deionized water. The cleaned samples were then dried in an oven at 100°C for 2 hours. Solutions of ferric chloride ($FeCl_3$) and Iron nitrate nonahydrate ($Fe(NO_3)_3 \cdot 9H_2O$) were prepared by

dissolving them separately in 99.99% pure ethanol to prepare solutions with 50 mM concentration. The clean silicon pieces were slowly immersed into these catalyst solutions and left for 10 minutes, then removed slowly. Then the coated samples were dried in the oven at 100°C for 2 hours [163].

The catalyst-coated silicon substrates were then placed in a quartz tube furnace used for Chemical Vapor Deposition (CVD). The furnace was heated to 750°C at a rate of 10°C per minute, while pure nitrogen gas (99.99%) was passed through the tube at 100 sccm, maintaining atmospheric pressure. The substrates were kept at this temperature for 30 minutes to form iron particles.

Then, acetylene gas was added at 250 sccm (while nitrogen remained at 100 sccm) for another 30 minutes to grow carbon structures. After that, the acetylene flow was stopped, and nitrogen gas was continuously passed while the furnace cooled down to room temperature. The final samples were removed and stored in airtight containers for analysis.

3.1.2 Surface characteristics of carbon electrode materials

Understanding the surface characteristics of carbon microspheres is crucial for their separation based on surface heterogeneity. Several techniques are commonly used for this purpose. Fourier Transform Infrared Spectroscopy (FTIR) identifies surface functional groups by measuring infrared light absorption, which provides insights into chemical bonds and surface chemistry. Scanning Electron Microscopy (SEM) offers detailed images of the surface morphology, revealing the shape, size, and texture of the microspheres at high resolution. X-Ray Diffraction (XRD) examines the crystalline structure of the microspheres, providing data on phase composition and crystallinity, which are linked to surface properties. The current study focuses on employing FTIR, SEM, and XRD to analyze the surface characteristics of carbon microspheres.

These characterization techniques together provide a comprehensive understanding of both the chemical and physical nature of the carbon microsphere, which is essential when correlating surface properties with separation processes, especially when targeting particles with distinct functional groups. By analyzing variations in surface properties such

as porosity, morphology, and chemical composition, the interactions between carbon microspheres and their surrounding environment, can be more accurately predicted and optimized.

3.1.2.1 FTIR Analysis

A sample of carbon microspheres was gathered, and the sample was prepared by mixing a small amount of carbon microspheres with dry and finely ground potassium bromide (KBr) powder. The sample was well mixed with KBr until a uniform blend is achieved. The FTIR instrument was warmed up to ensure stable performance, and a background scan was performed with no sample in the beam path to record the baseline spectrum of the environment. This was used to subtract any atmospheric or instrumental noise from the sample spectrum. Then the prepared sample was placed in the FTIR sample compartment, in the sample holder.

Then the FTIR spectrometer was set to scan within 4000 cm^{-1} to 400 cm^{-1} wavenumber range. The scan was initiated, and the instrument was allowed to acquire the spectrum. The resulting FTIR spectrum was examined to identify absorbance or transmittance as a function of wavenumber. The observed peaks were analyzed with a reference spectra or literature data to determine the types of chemical bonds and functional groups.

3.1.2.2 SEM Analysis

A sample of dry carbon microspheres were obtained and was dispersed on an adhesive tape. And the microspheres were spread across the tape using a fine brush or a spatula. The sample was coated with a thin layer of conductive material to avoid charging effects and enhance image quality. After sample preparation, the machine was turned on and was allowed to warm up. The sample was carefully placed into the SEM sample chamber, and the proper positioning for imaging was ensured.

Imaging parameters were adjusted imaging started with lower magnification to locate areas of interest, then switch to higher magnifications for detailed observation of surface features. The acquired images were analyzed to assess the surface morphology, size, shape, and texture of the carbon microspheres.

3.1.2.3 Raman Spectroscopy

A dry sample of carbon microspheres was obtained and carefully placed onto a clean glass slide to prepare it for Raman spectroscopy. The sample was gently spread and flattened to form a thin, even layer, ensuring consistent laser focus and minimizing background interference. Care was taken to avoid clumps or uneven areas that could affect the spectral quality.

The prepared slide was then positioned on the stage of the Raman microscope. Initial calibration and alignment of the laser source, objective lens, and spectrometer were performed to ensure optimal focus and measurement accuracy. The excitation source selected was 532 nm laser, and the laser power was adjusted to an appropriate level to avoid thermal damage to the sample.

The spectral acquisition range was set from 800 to 2000 cm^{-1} to capture the characteristic D band and G band of carbon materials. The objective lens was used to focus on selected regions of the sample. Then the spectra obtained was subjected to baseline correction and normalization, and the intensity ratio of the D and G bands was determined to assess the degree of disorder and graphitization of the carbon microspheres. The resulting data were interpreted to evaluate the structural quality, defects, and overall graphitic nature of the material.

3.1.2.4 XRD Analysis

A sample of dry carbon microspheres were obtained and was carefully loaded into an XRD sample holder. Smooth the surface to ensure a flat and even layer, which helps in obtaining accurate and reproducible diffraction data. The initial alignment and calibration were performed for the X-ray source, detector, and goniometer to ensure accurate positioning and measurement. The prepared sample was put into the XRD sample chamber ensuring the proper positioning.

The 2θ range was set for the scan, which typically covers from 5° to 80° 2θ, to cover a broad range of diffraction angles and capture all relevant peaks. The step size, counting time per step were selected, and the X-ray source parameters, such as voltage and current

were adjusted. Then the scan was started to collect diffraction data. The XRD instrument will measure the intensity of X-rays diffracted by the carbon microspheres as the goniometer rotates and the detector records the diffracted beams.

Thereafter, the obtained diffraction pattern was analyzed to identify characteristic peaks corresponding to the crystalline phases of the carbon microspheres. The peaks were compared with standard reference databases to match them with known diffraction patterns.

Phase identification was done by comparing the diffraction pattern with reference patterns. This helps in understanding the crystalline structure and phase composition of the carbon microspheres. The degree of crystallinity and parameters such as unit cell dimensions, lattice parameters, and crystallite size were then evaluated.

3.2 Separation of heterogeneous carbon microspheres using sol-gel method

Among various techniques applicable, the sol-gel method provides a versatile and controllable platform for selective interaction and immobilization, enabling separation based on surface functionality and interaction strength.

3.2.1 Functionalization of carbon microspheres

Fabrication of carbon microspheres with an amino functional group was done using aniline as the source of the amino group. 10µl of aniline was dissolved in 6.66 µl of HCl aqueous solution (2.0 mol/L), followed by the addition of 10mg of carbon microspheres into the solution. After continuously stirring for a period of 30 minutes, 3.33 ml of 0.1M ammonium persulfate was added to the same solution. Amino functionalization of the carbon microspheres was allowed to happen for a period of 12 hours at room temperature [164].

The product was separated and rinsed with deionized water and ethanol several times. The functionalized carbon microspheres were characterized using FTIR analysis to detect the successful functionalization of the bare carbon microspheres.

3.2.2 Preparation of microchannels

Microfluidic channels were fabricated from PMMA (Poly Methyl Methacrylate) which is an ideal material for the fabrication of microchannels due to its transparent amorphous polymer structure, high strength and good flexibility. The channel pattern was engraved on PMMA plates using computer numerical control (CNC) milling machine to create a channel with 100 µm x 150 µm cross section and serpentine geometry. Then the engraved channel was enclosed with another PMMA plate. The two plates were bonded via thermal bonding. In addition to that, PMMA plates of 1cm x 3cm was used to test the coating process and the characteristics of the coated PMMA surfaces.

The fabricated channel should be coated with a material which have the capability to achieve the separation of microspheres with carboxyl functional groups and amino functional groups from bare carbon microspheres. PMMA microchannel coated with silica gel was used to fulfil this objective. Silica gel was selected as the coating material to enable effective separation of microspheres functionalized with carboxyl and amino groups. When the microspheres are suspended in an ethanol solution, the separation mainly relies on hydrogen bonding and polar interactions, rather than electrostatic forces.

With silanol groups on its surface, silica gel provides a chemically active interface capable of forming hydrogen bonds with both carboxyl and amino groups. Among these, carboxyl functionalized microspheres form stronger hydrogen bonding interactions with the silica surface due to the presence of both a carbonyl and hydroxyl group. Amino functionalized microspheres also interact with silica, but generally weaker in ethanol. Thus, carboxyl functionalized microspheres migrate faster through the microchannel. Additionally, silica gel adheres well to PMMA surfaces, ensuring a stable and uniform coating.

Experiments were carried out with styrene microparticles as a substitute for carbon particles in the initial experiments. These microparticles are identical, except for their surface chemistry. Some of the particles contain polar functional groups attached to their surface and makes interactions with the silica get coating inside the channel. Due to the interaction with the channel wall, particles with polar functional groups slows down while

bare particle move forward through the channel. Therefore, this phenomenon results in an effective separation between particles with heterogeneous surface properties.

3.2.3 Surface modification of the PMMA microchannel

The modification of the interior surfaces of the microchannel was done using the sol-gel method. The silica sol with colloidal silica particles was prepared following the Stober method for nanoparticle synthesis. TEOS (Tetraethyl orthosilicate) was used as the silica precursor where a molecule of TEOS reacts with two equivalents of water, leading to the formation of silica in its fully condensed form. In this procedure, 28 ml of distilled water was initially mixed with 3 ml of 25% (w/w) Ammonium Hydroxide and, 25 ml of Ethanol was separately mixed with 1.5 ml of TEOS. Thereafter, the two solutions were brought together, and the solution was continuously stirred for 2 hours at room temperature. Finally, 2 ml of the prepared sol was taken and rapidly mixed with 18 ml of 1M Hydrochloric acid for 10 minutes.

PMMA micro channels were cleaned by flushing ethanol at a rate of 20 ml/hr for 2-3 minutes. This was followed by the prepared silica particle solution and, it was flowed through the channel at a rate of 20 ml/hr for 10 minutes. After that, the channel was purged with air at a rate of 20 ml/hr to remove excess solution and dried by keeping on the hot plate at 60 °C for 30 minutes. Characterization of the coated microchannels were done to ensure the successful deposition of silica inside the microchannel wall. SEM (scanning electron microscopy) and FTIR (Fourier transform infrared spectroscopy) of coated PMMA plates were done to characterize the coating.

3.2.4 Microfluidic experiments to separate carbon microspheres with carboxyl and amino functional groups

Microfluidic experiments were conducted using coated microchannels and the flow of microspheres was observed under fluorescence microscopy. Carboxyl modified styrene microspheres and amino modified styrene microspheres which are identical, except for their surface chemistry were used as microspheres with heterogeneous surface properties.

They were allowed to flow through the coated microchannels at a rate of 0.01 ml/hr, and their fluorescence intensity was capture through fluorescence microscopy. Among the three types of microspheres, carboxyl modified styrene microspheres and amino modified styrene microspheres contain polar functional groups attached to their surface and makes interactions with the silica get coating when flowing inside the channel. Flow of microspheres through the channel was observed through micrographs captured in 25 ms intervals.

3.3 Determination of the optimum conditions which enable separation of heterogeneous carbon microspheres

The microfluidic chip was fabricated with an annular microchannel to form a stable interface between nanoparticles in suspension and deionized water at the T-junction observation area. Two PMMA plates with dimensions 21.39 × 37.90 × 2.00 mm, were laser-cut, and the annular microchannel, with a width of 200 μm and a depth of 100 μm, was engraved into the bottom plate using the CNC milling machine. After engraving, the plates were annealed, cleaned with deionized water and isopropanol, and dried using compressed air. Then the surface hydrophilicity was increased by plasma discharge and was bonded through thermocompression. Laser machining created two electrode slots, each measuring 50.00 μm in length and 0.30 μm in width, to accommodate copper parallel plate electrodes, spaced 5 mm apart. For sealing, two nitrile elastomer O-rings were used to secure the through holes of the microchip, which was mounted in a custom stainless steel chip fixture. Figure 3-1 depicts the microfluidic system, which was used for the experiments, connected with the syringe pump to control the flow rates.

This system utilizes a 1/16-inch diameter polytetrafluoroethylene (PTFE) tube as both the inlet and outlet tubing. For the inlet, one end of the PTFE tube is connected to a check valve and the other end of the inlet tube is attached to a customized stainless steel chip fixture using a tube fitting. The outlet tube follows the same setup, with one end connected to the chip fixture through an identical fitting. This configuration ensures controlled fluid flow and prevents backflow, leveraging the durability and chemical resistance of PTFE and stainless-steel components.

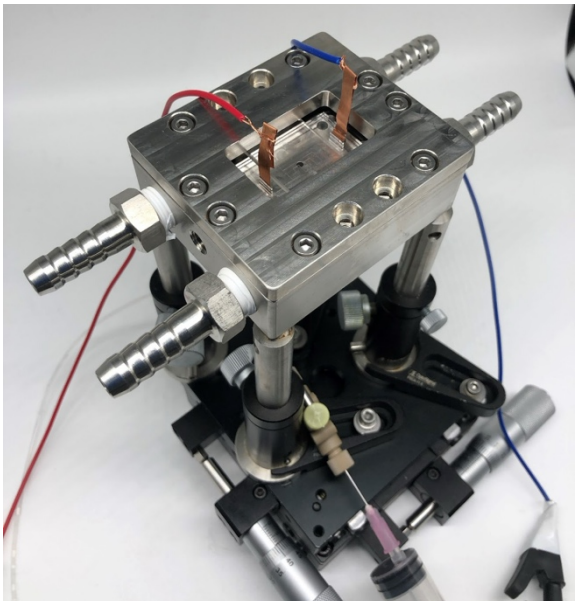

Figure 3-1: Microfluidic system integrated with the syringe pump

3.3.1 Sample preparation

An aqueous suspension of carboxyl-functionalized polystyrene nanoparticles was used for the experiments. These nanoparticles exhibit green fluorescence with an excitation wavelength of 470 nm and an emission wavelength of 525 nm. At 25 °C, the refractive index of the nanoparticles is 1.59.

The size distribution of the polystyrene nanoparticles in the aqueous medium was measured using a laser particle analyzer and the nanoparticles were found to have diameters ranging from 38.6 nm to 78.6 nm, with an average diameter of 54.6 nm. The zeta potential of the carboxyl-modified polystyrene nanoparticles at a pH of 7 was measured to be -41.23 ± 0.77 mV using a Zeta-Potential Analyzer.

Construction of the calibration curve of fluorescence intensity versus nanoparticle concentration done prior to the experiments. The nanoparticle suspension was first diluted with deionized water at various ratios, with each dilution treated by 2 minutes of ultrasonic mixing for uniformity. Each diluted suspension was sequentially injected into a microfluidic chip and observed under an epifluorescence microscope equipped with a 4×

objective lens. The fluorescent dyes within the nanoparticles were excited using an LED light source, set at an intensity of 36 units for both 2B (Blue) and 3-GR (Green and Red) channels and a fluorescence filter cube was used to match the excitation and emission wavelengths of the nanoparticle dyes.

Images were captured with a CMOS camera at an exposure time of 200 ms. The grey values from images of each diluted suspension were processed in ImageJ software and normalized to determine fluorescence intensity. The microchannel was thoroughly cleaned with deionized water and air between each test to prevent contamination. Tests were conducted diluting 100 µl of nanoparticle suspension to 150 µl with deionized water and treated by ultrasound for 2 minutes to ensure uniform dispersity. To reduce costs and conserve the nanoparticle suspension, 8 ml of immiscible dimethyl silicone oil was used as a propelling agent. This oil, along with the 150 µl nanoparticle suspension, was drawn into a 1 ml commercial syringe, allowing the controlled and minimal use of the nanoparticle suspension.

3.3.2 Experimental Setup

The procedure began by connecting a syringe containing the nanoparticle suspension to the inlet PTFE tube through an inlet check valve. Dimethyl silicone oil was used to propel the suspension through the inlet PTFE tube until it reached the O-ring, at which point the injection was paused to prevent overfilling. To remove any trapped air, another syringe filled with dimethyl silicone oil was used to fill the outlet tube. Once filled, the outlet check valve was closed to prevent the silicone oil from flowing out due to gravity. Thereafter the syringe containing dimethyl silicone oil was disconnected from the outlet check valve, completing the setup for the control condition and ensuring a stable environment for measuring the diffusion coefficient of nanoparticles without external field interference.

Initially, the microfluidic chip was injected manually with deionized water, then it was enclosed in a stainless-steel chip fixture. Once secured, the device was placed under a 4× objective lens on the fluorescence microscope for observation. The coarse and fine focus adjustments were then used to bring the microchannel of the microfluidic chip into clear

view. Detection of the fluorescent signal was done using the same fluorescent filter cube previously used to obtain calibration curve data.

Before injecting the nanoparticle sample, the outlet check valve was opened. The plunger of the sample syringe was then gently pushed to allow the nanoparticle sample to enter the microchannel through the O-ring. The fluorescent interface became visible on the computer monitor through the CMOS camera, and the exposure and delay times were set to 200 ms and 1000 ms, respectively, resulting in a frame rate of 0.83 fps. Once the fluorescent interface stabilized, the inlet and outlet check valves were closed in sequence to prevent any external turbulence interference and a sequence of images was recorded over 50 minutes using the CMOS camera.

3.3.3 Investigation of the effect of an external electric field on diffusion of nanoparticles

To investigate the effect of an electric field on nanoparticle diffusion, an external field was created using two small copper plates, which served as parallel plate electrodes. These plates were positioned in the prefabricated electrode slots within the microfluidic chip, with a narrow gap carefully maintained between the copper plates and the stainless-steel fixture to prevent short-circuiting. The copper electrodes were connected to the positive and negative terminals of a direct-current (DC) stabilized power supply using two 1 m wires.

Before beginning the experiment, the power supply's maximum output voltage and current were adjusted to 30 V and 0.005 A, respectively. When the power supply was activated, it operated in a steady voltage output mode, as there was no external circuit path. Applying the 30 V voltage to the copper electrodes generated an electric field with a strength of approximately 60 V/cm between the plates. The direction of the field strength could be reversed by swapping the connections of the positive and negative poles on the power supply.

3.4 Evaluation and simulation of the effect of surface forces

The simulation model was developed under conditions similar to those used in laboratory experiments to facilitate model verification. The modeled system consists of a microchannel filled with water, where a particle solution is introduced at the inlet. This particle solution contains carboxyl-modified polystyrene nanoparticles at a concentration of 3.291×10^{-5} % (v/v) in water. In the model, the particles move through the channel solely by diffusion, driven by the concentration gradient, with no external momentum applied. The system considered for the model is a microchannel filled with water, and the solution of particles is introduced at the inlet.

The model was developed considering that the diffusion occurs from the nanoparticle solution introduced at the inlet, into the water filled microchannel, with an initial assumption of zero nanoparticle concentration throughout the length of the channel. Diffusion begins immediately when the nanoparticle suspension is injected at the inlet, allowing the model to be formulated based on a one-dimensional semi-infinite diffusion process. The diffusion dominated flow of nanoparticle inside the channel is a multicomponent flow consisting polystyrene nanoparticles in a water medium. The diffusion coefficient can be defined as the proportionality constant between the species concentration gradient and the diffusion flux.

3.4.1 Simulation Setup in ANSYS Fluent

The development of the model geometry and the computational mesh was done. Fluent setup was initialized with double precision enabled to improve result accuracy. The computational mesh was automatically imported into Fluent, where any additional domain modifications could be made in the domain setup. The multicomponent model was activated using the species model, with inlet diffusion enabled under species transport. Fluent's dilute approximation was used to simulate species transport driven by concentration gradients.

In the solver settings, a pressure-based, transient time, and absolute velocity formulation were selected, and parameters for species transport through the fluid medium were configured using the species model. A mixture of polystyrene nanoparticles and water was then added, and mixture settings were adjusted accordingly. Boundary conditions were specified, with the inlet set as a velocity inlet with zero inlet velocity, and the walls as stationary with a no-slip condition.

The nanoparticle mass fraction at the inlet was set to 0.0035, and the fluid temperature was maintained at room temperature. The carboxyl functionalized polystyrene nanoparticles considered for the model has an average size of 54.6 nm in diameter and the diffusion occurs under externally applied electric field with field strength of 60 Vcm^{-1}. The zeta potential of the carboxyl modified polystyrene nanoparticles and channel wall are - 41.23 mV and 45.0 mV, respectively. Thereafter, the simulation was run, and the results were analysed.

CHAPTER 4

RESULTS AND DISCUSSION

In this section, the outcomes from the characterization of microspheres, and the diffusion experiments are presented. Moreover, the results obtained through the diffusion experiments under the effect of an external electric field are presented and its application as a possible method of separation of microspheres with microspheres with heterogeneous surface properties is discussed. Furthermore, the simulation of the separation of heterogeneous carbon microspheres using Ansys Fluent is presented and the results are discussed.

4.1 Study on surface characteristics of carbon electrode materials

Surface characteristics of carbon microspheres were analyzed using FTIR analysis, SEM analysis, Raman spectroscopy and XRD analysis. These techniques were employed to evaluate both the chemical composition and structural properties that influence the electrochemical behavior of the carbon microspheres. FTIR analysis was used to identify the presence of different functional groups, which are critical for surface reactivity and wettability. SEM imaging provided insights into particle morphology, surface roughness, and size distribution.

Raman spectroscopy was utilized to assess the degree of graphitization and structural disorder, which significantly impact the electrical conductivity. XRD analysis further confirms the amorphous or crystalline nature of the carbon microspheres, contributing to the understanding of their structure, composition, and physical properties. Collectively, these characterization methods offer a comprehensive profile of the surface properties relevant to supercapacitor applications.

4.1.1 FTIR Analysis

FTIR analysis is important to identify the availability of various functional groups on the selected sample of carbon microspheres. Characteristic peaks corresponding to specific functional groups can provide insights into the surface chemistry and possible modifications of the carbon microspheres. The transmittance spectra of carbon microspheres were tested, and the spectrum is given in Figure 4-1

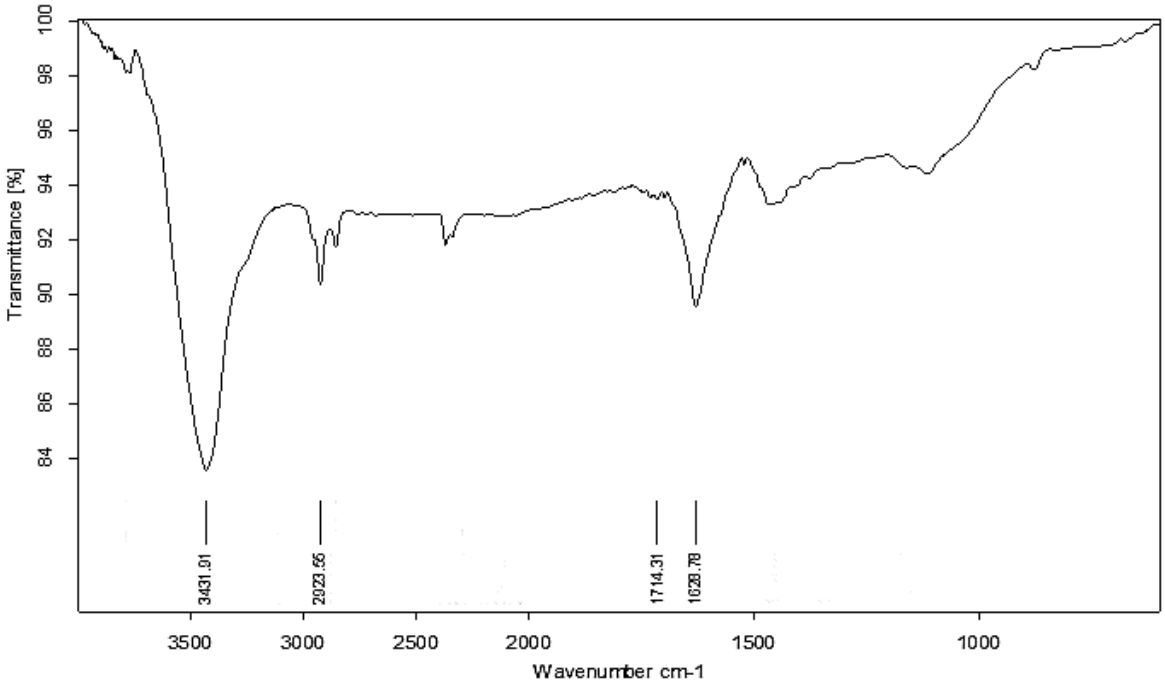

Figure 4-1: FTIR spectra of carbon microspheres

The spectrum was recorded in 4000 – 600 cm^{-1} range. A broad peak at 3341.91 cm^{-1}, within the typical range of 3200–3600 cm^{-1}, corresponds to O–H stretching vibrations, suggesting the presence of hydroxyl or carboxyl groups. A weaker band at 2923 cm^{-1}, located in the 2850–2950 cm^{-1} region can be attributed to C–H stretching vibrations of aliphatic hydrocarbons. The peak at 1714 cm^{-1}, within the 1700–1750 cm^{-1} range can be assigned to C=O stretching vibrations, commonly associated with carbonyl groups such as carboxylic acids, ketones, or aldehydes.

Additionally, the band at 1628 cm^{-1}, can be attributed to C=C vibrations and revels the aromatization of the samples [165], [166], [167], [168]. Moreover, the peak at 1030 cm^{-1}, which lies within the 1000–1260 cm^{-1} range, can be associated for C–O stretching vibrations are that are formed during the synthesis of carbon microspheres.

4.1.2 SEM Analysis

Scanning electron microscope (SEM) is one of the most widely used techniques in characterization of micro particles. The SEM analysis of the selected sample of carbon microspheres was conducted and shown below in Figure 4-2 (a) and (b) are images obtained at a magnification of 10 KX and 5 KX respectively.

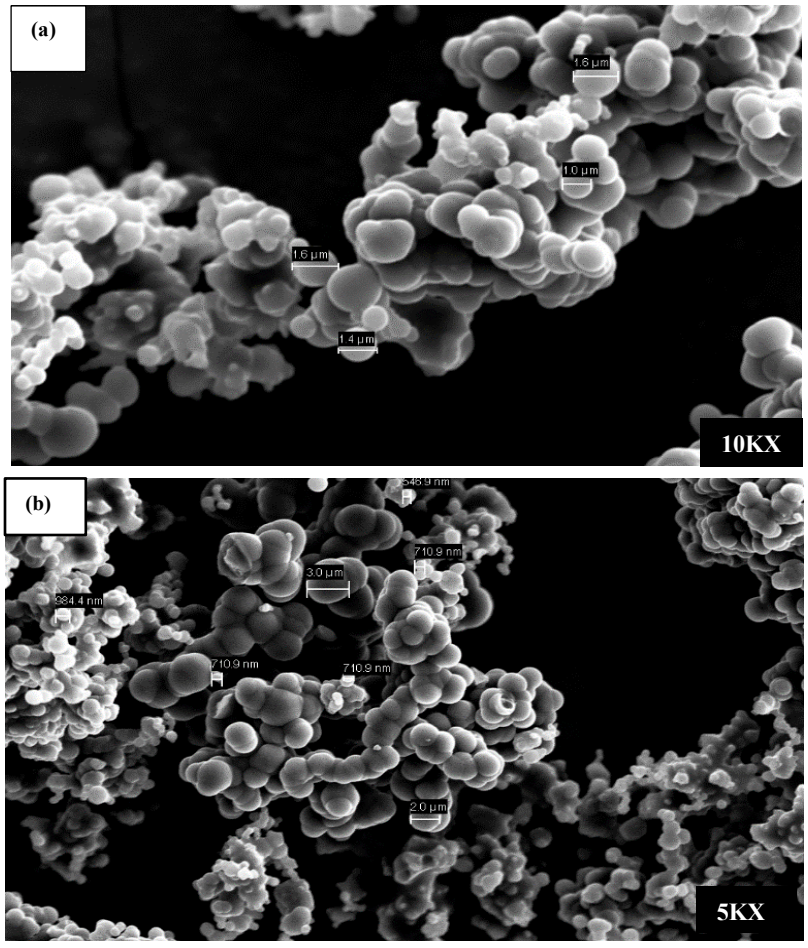

Figure 4-2: SEM images of carbon microspheres (a) 10 KX, (b) 5 KX magnifications

Analysis of SEM images is beneficial in understanding morphology and topology and detailed surface structure of carbon microspheres. According to figure 4-2 (a) & (b), the carbon microspheres own a spherical shape, and aggregates of carbon microspheres with diameters ranging from 550 nm to 3 μm are visible in SEM micrographs.

4.1.3 Raman Spectroscopy

Raman spectroscopy is an important technique in characterizing carbon materials where, the G and D bands are key indicators of their structure and properties. Figure 4-3 depicts the Raman spectra of the sample of carbon microspheres.

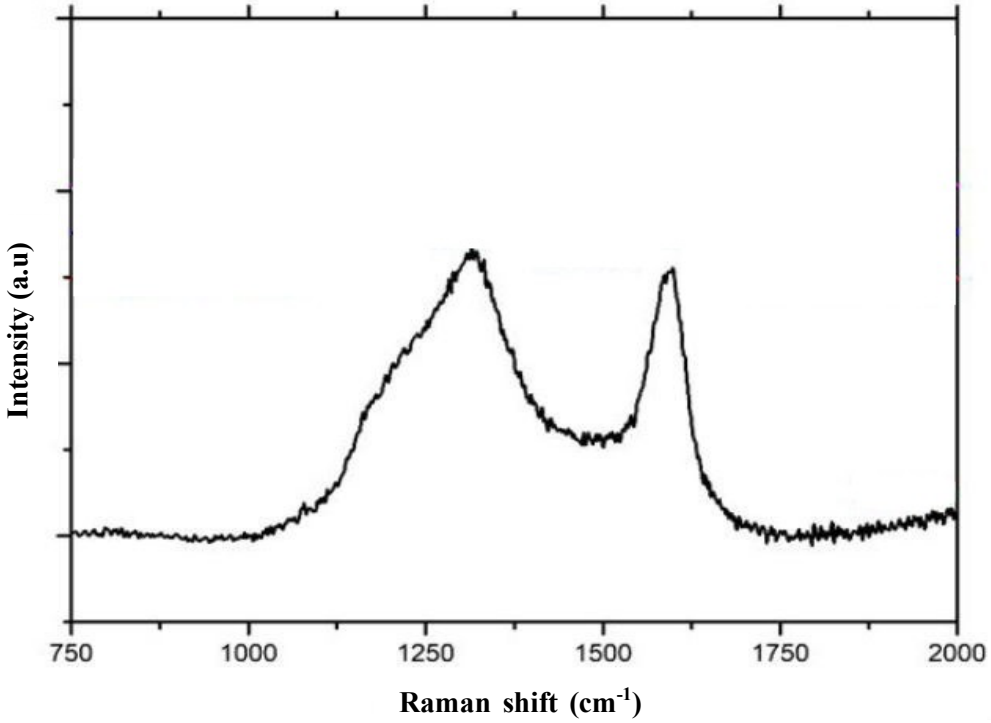

Figure 4-3: Raman spectra of carbon microspheres

The G band which is located around 1580 cm^{-1}, signifies the in-plane vibrations of C-C bonds indicating a well-ordered arrangement of carbon atoms [169]. The D band which appears near 1350 cm^{-1}, indicates disorders or defects in the graphitic lattice, often arising from the presence of dangling bonds or edge effects.

The G band in between 1592 -1600 cm^{-1} can be assigned to an E_{2g} mode of graphite and is related to the vibration of sp^2-bonded carbon atoms in a 2-dimensional hexagonal lattice, such as in a graphite layer [169], [170]. The D band in between 1308 - 1323 cm^{-1} corresponds to the vibrations of carbon atoms having dangling bonds in-plane terminations of a disordered graphitic network.

The intensity ratio between the D and G-bands, ID/IG can be used to characterize the degree of graphitization carbon microspheres, and it is proportional to the number of defects in graphitic carbon within the analyzed spectrum. ID/IG value was calculated to be 1.08 for the carbon microspheres and it reflects an amorphous carbon structure with a high content of lattice edges or defects with low degree of graphitization.

4.1.4 X-Ray Diffraction

Figure 4-4 shows the XRD pattern of carbon microspheres. Two clear characteristic peaks of the graphite structure can be observed at 2θ = 26.2° (d= 3.3985 Å) and 2θ = 45° (d = 2.0128 Å).

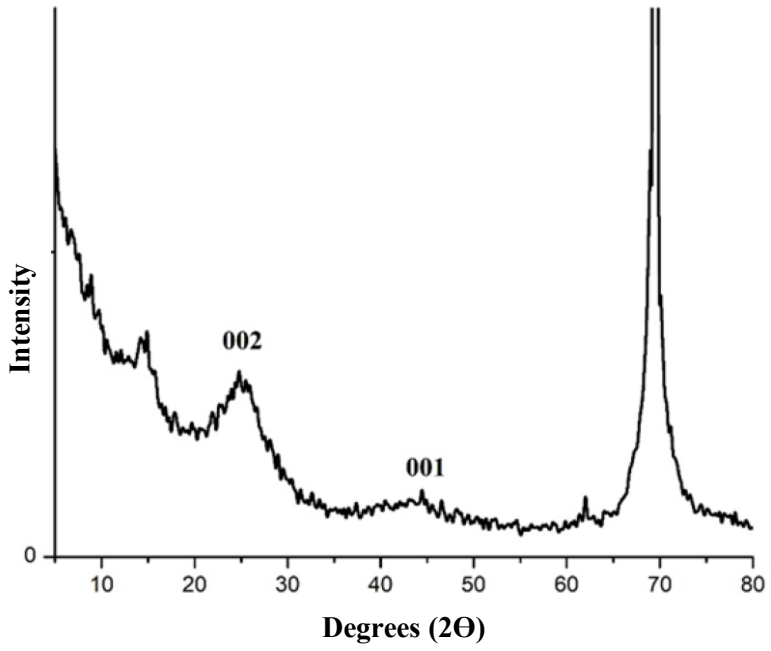

Figure 4-4: XRD pattern of carbon microspheres

These peaks can be assigned to be originating from typical graphitic (002) and (001) planes, and it has been reported that the presence of a peak at 44.01° gives a good indication of the presence of hexagonal graphite lattice. Moreover, the minor and major peaks observed at 14.44° and 69.16°, can be attributed to reflections from the underlying silicon substrate, since silicon wafers were used as the substrate in the CVD method for fabrication of carbon microspheres.

Peak broadening in the XRD suggests somewhat lower degree of graphitization, and the presence of amorphous carbon can be assumed. Crystalline size of the carbon microspheres was measured by measuring the full-width half maximum (FWHM) of the peak, incorporating Scherer formula. The crystalline size was obtained to be 16.983 Å, indicating that there could be about 5 graphitic layers present in single crystallite.

4.2 Separation experiments using silica gel modified microchannel.

As discussed in chapter 3, PMMA microchannels with 100 µm x 150 µm cross sectional area and serpentine geometry were fabricated, and an image of the fabricated channel is shown in Figure 4-5.

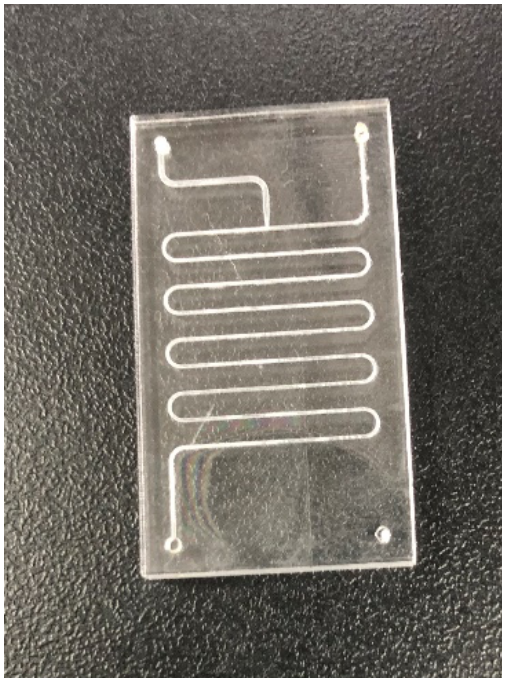

Figure 4-5 PMMA fabricated microchannel

4.2.1 FTIR analysis of amine functionalized carbon microspheres

Characterization of the functionalized carbon microspheres is important to ensure the successful binding of functional groups to the microspheres. FTIR characterization was done to verify the successful bonding of amine functional groups to the carbon microspheres. Figure 4-6 depicts the FTIR spectra of amine functionalized carbon microspheres whereas in comparison with that Figure 4-7 represents the FTIR spectra of bare carbon microspheres.

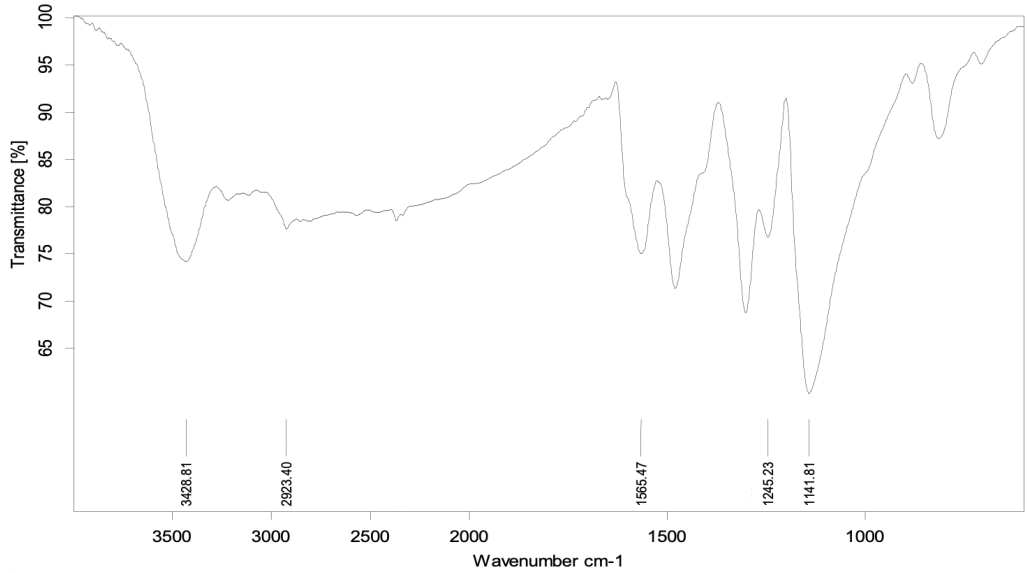

Figure 4-6: FTIR spectra of amine modified carbon microspheres

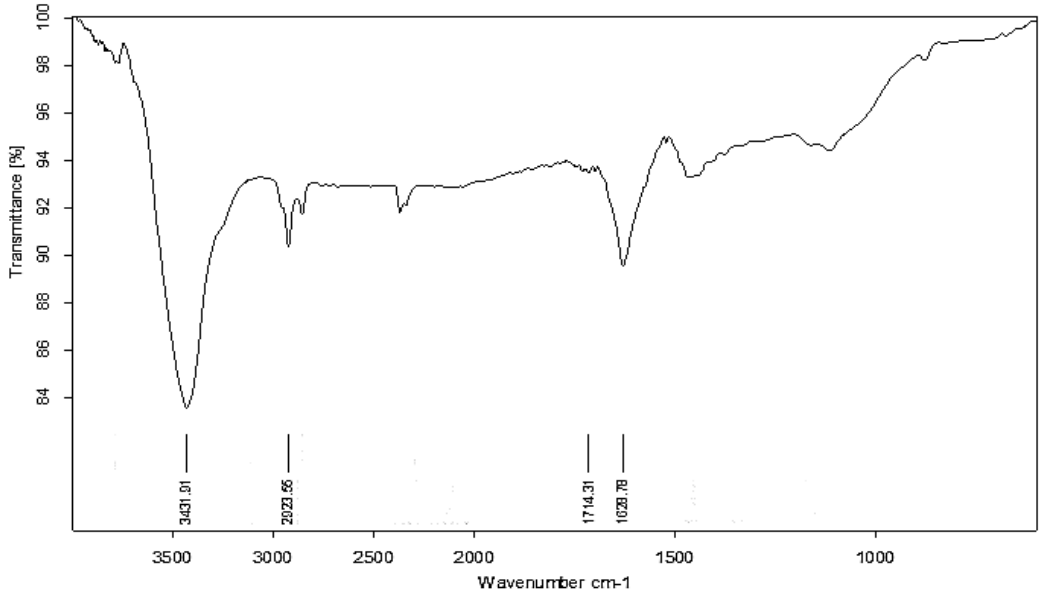

Figure 4-7: FTIR spectra of bare carbon microspheres

By referring to Figure 4-6 and Figure 4-7, it is visible that the FTIR spectra of functionalized carbon microspheres have a strong peak at 1141 cm^{-1} which corresponds to the C-N stretching mode vibrations. Moreover, the band at 1243 cm^{-1} is due to the presence of protonated $C\text{-}N^{+}$ group in the functionalized carbon microspheres [164].

Moreover, the peaks in the region 3500 - 3400 cm^{-1} can be attributed to N-H stretching vibrations, and the peak at 3428 cm^{-1} is assigned to N-H stretching vibrations. Also, the peak at 1565 cm^{-1} C–NH bonds [171]. In contrast, these peaks are absent in the spectrum of the bare carbon microspheres. Therefore, this comparative analysis confirms the effective incorporation of amine functional groups onto the surface of the carbon microspheres.

4.2.2 Characterization of the coating

Characterization of the coating was done using the coated PMMA plates since it is not feasible to characterize the coated PMMA microchannels. SEM and FTIR analysis were performed on these coated PMMA surfaces.

4.2.2.1 Characterization of coated PMMA surface

Shown below in Figure 4-8 is the Attenuated Total Reflectance - Fourier Transform Infrared ATR - FTIR spectra of a non-coated PMMA plate.

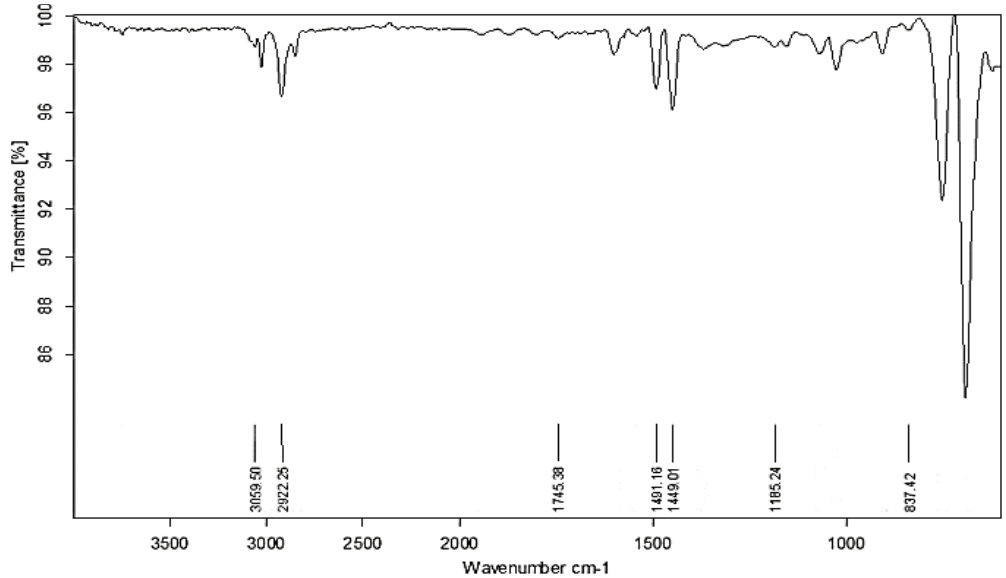

Figure 4-8:ATR-FTIR spectra of non-coated PMMA surface

Figure 4-9 depicts the ATR-FTIR spectra of a silica coated PMMA plate.

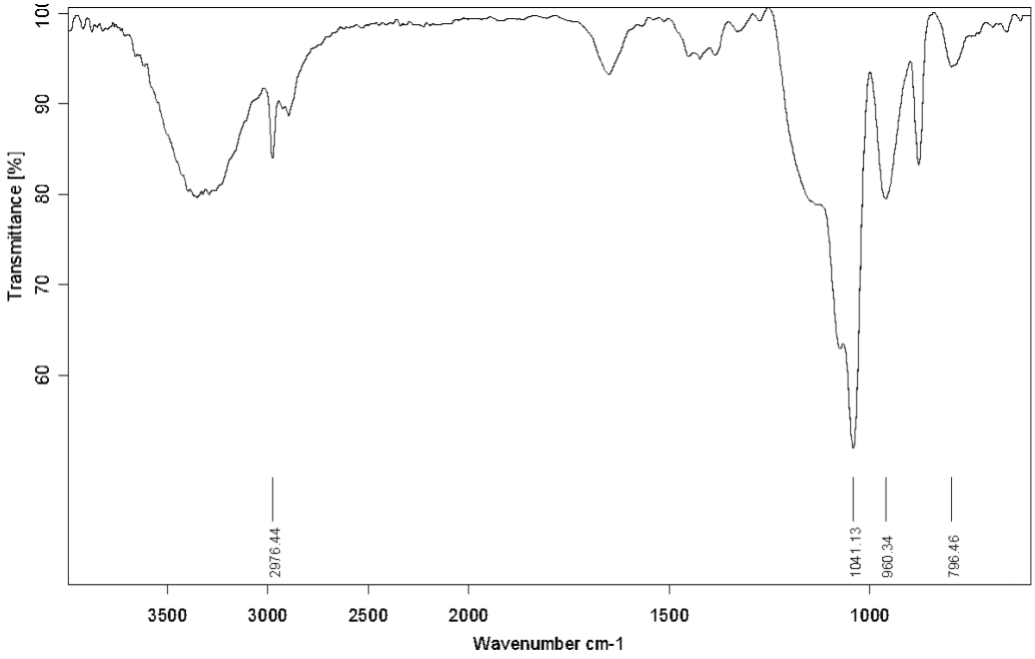

Figure 4-9: ATR-FTIR spectra of coated PMMA surface

The bands in between 3100 – 2800 cm^{-1} can be assigned to methyl and methylene C-H vibrations and bands around 1500 – 1350 cm^{-1} can be assigned bending vibrations of methyl and methylene C-H bonds. Also, C=O stretching mode vibrations can be allocated for peak at 1745 cm^{-1}.

Bands in the range 1350 – 1100 cm^{-1} corresponds to stretching vibrations of the ester group. The band at 1185 cm^{-1} can be assigned to C-H deformation vibrations, and the band at 837 cm^{-1} corresponds to methylene rocking mode vibrations [172].

In previous studies using solid silica gels has given four peaks at ∼1200 cm^{-1}, ∼1150 cm^{-1}, ∼1100 cm^{-1} and ∼ 950 cm^{-1} [173]. Silica materials have an absorption band corresponding to the Si–O–Si bond asymmetric stretching in the region from 1300 to 1000 cm^{-1}[174]. Hence, referring to the spectra given in Figure 4-9, the peak at 1041 cm^{-1} can be assigned to asymmetric stretching of O-Si-O and the symmetric mode of Si–O–Si bond has been found around 791 cm^{-1} [175].

The peak at 960 cm^{-1} shows that Si-OH bonds present in the coating. Further, the bands at 2976 cm^{-1} can be assigned to bending vibration modes of aliphatic CH_2 groups. Thus, the ATR-FTIR spectra confirms the successful deposition of a silica coating on the PMMA plate.

SEM analysis also was conducted ensure the successful deposition of the coating within the PMMA surface. The analysis was conducted using PMMA plates coated using the same exposure to the coating solution as with the micro channels. Figure 4-10 shows the SEM micrographs obtained through the analysis.

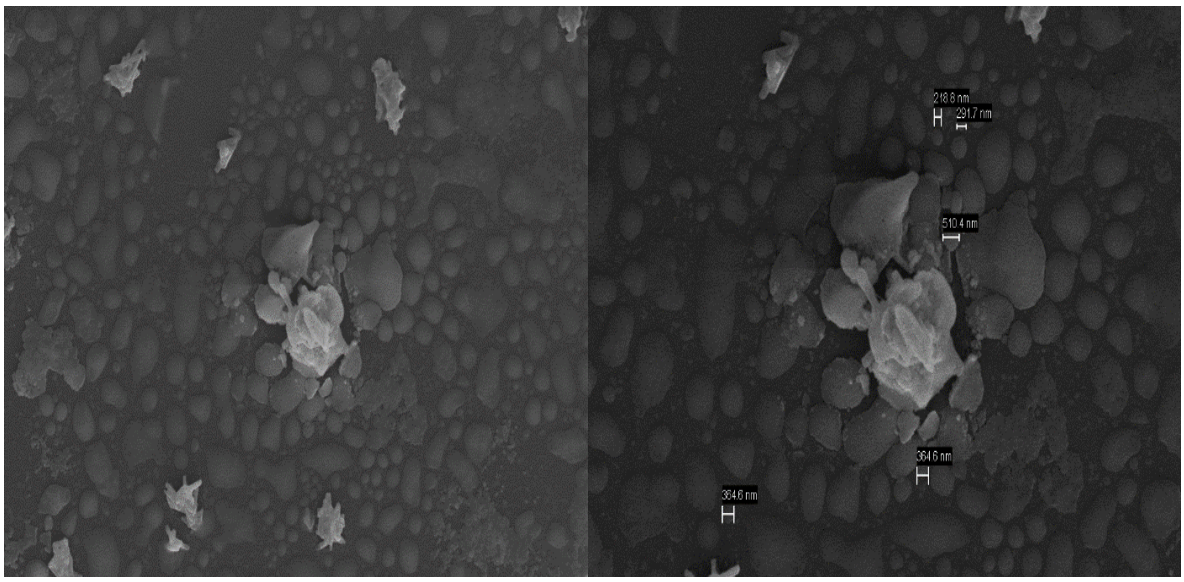

Figure 4-10: SEM micrographs of coated PMMA surface

The silica coating exhibits a granular morphology with uniformly dispersed spherical particles where, the particle diameters range from approximately 200 to 500 nm. Some aggregation of the particles is observed, can be explained as a result concentration differences during the sol-gel process. The coating appears continuous and densely packed which indicates good surface coverage of the PMMA substrate by the silica nanoparticles.

4.2.3 Microfluidic separation of functionalized carbon microspheres through coated microchannels

Once the microchannels are successfully coated, the microspheres are introduced into the channel and the flow behavior was observed under fluorescence microscope. Few examples for the in-situ micrographs obtained through fluorescence microscopy are given in Figure 4-11. These images help to analyze the distribution, movement, and interaction of microspheres within the coated microchannels.

The images obtained from in situ observation of microsphere flow were analyzed using ImageJ to determine the flow rate of microspheres. The TrackMate plugin in ImageJ was utilized to track the path of each individual particle and to calculate their velocities. TrackMate haa the capability to identify objects within a given radius, and track them over time, following a classical single particle tracking scheme. This enabled accurate analysis of particle motion within the microchannel. The collected data were further processed to evaluate variations in microsphere velocity along different regions of the channel.

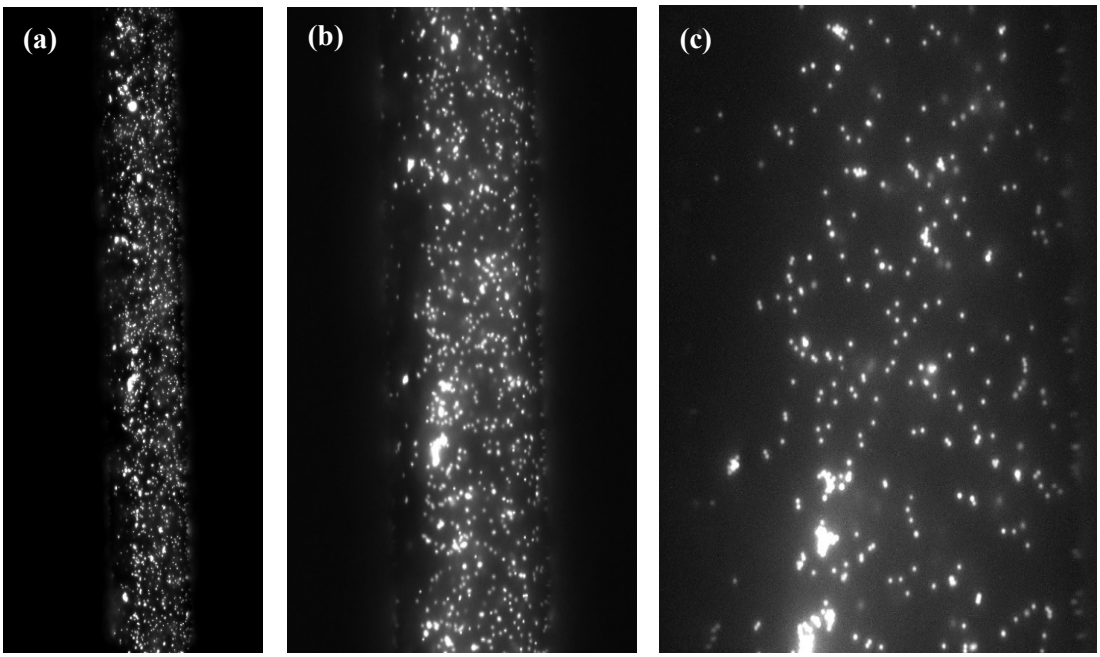

Figure 4-11: Optical micrographs of particle flow through the channel (a)10x magnification, (b)20x magnification and (c) 50x magnification

The analysis was done using the LoG detector with estimated blob diameter of 30 pixel and threshold value of 20. This detector is suitable for identifying spherical particles, making it ideal for tracking microspheres. After setting the detection parameters, the detection process was carried out, followed by the initial filtering of the spotted particles. The filtering helps ensure that only particles matching the desired size are selected for tracking. This step is crucial for validating the detection parameters and ensuring that only the microspheres of interest are selected for subsequent tracking and velocity analysis.

For visualization, the HyperStack Displayer was used, which reuses the ImageJ stack window and nondestructively overlays the results on the original image. This allows for dynamic visualization without altering the raw data. At this stage, the detected spots are highlighted with purple circles on the image stack, clearly marking each identified microsphere, as shown in Figure 4.10. This visual representation aids in verifying the accuracy of detection and tracking before proceeding to further analysis.

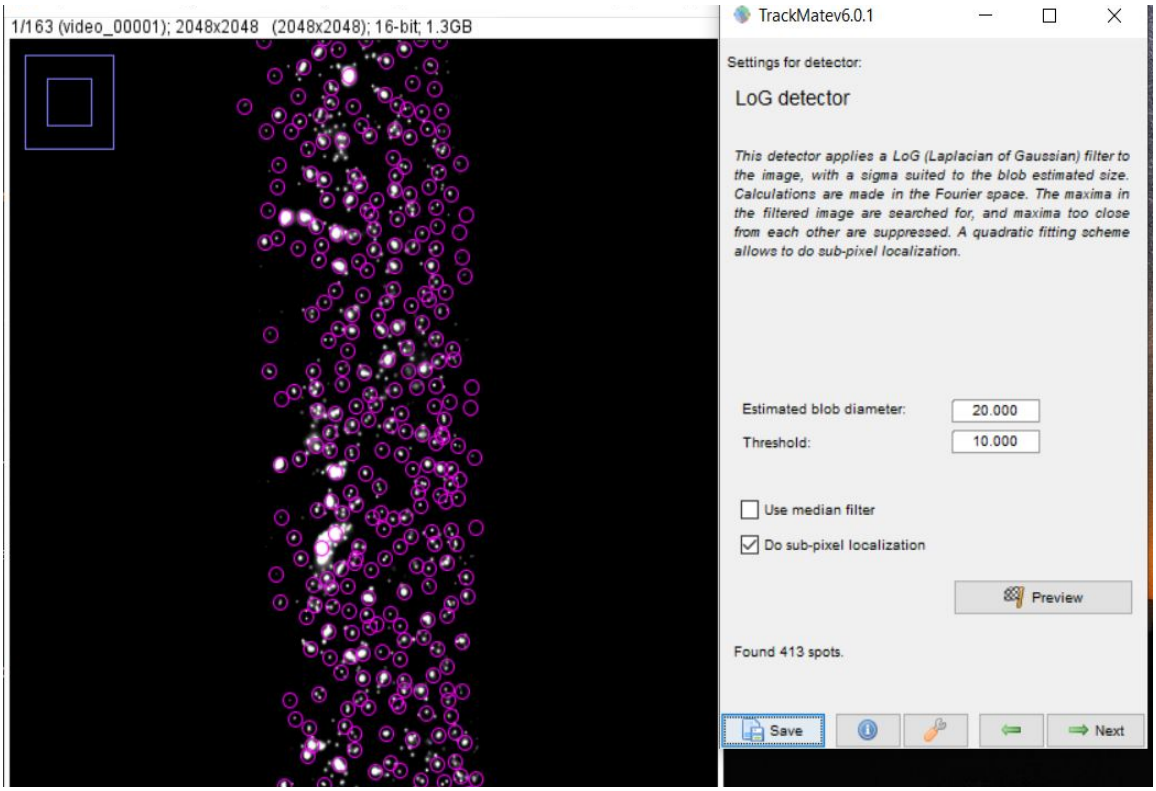

Figure 4-12: Detection of particles using the TrackMate LoG detector

The following stage provides more features to filter the spots further based on parameters such as intensity, quality, and size, allowing precise refinement of the dataset. Selection of the tracker is done afterward, where the Simple LAP tracker was utilized for the current analysis due to its robustness and efficiency in handling particle movements over time. This was followed by the configuration of the Simple LAP tracker, which included setting maximum linking distance and gap-closing parameters to ensure accurate trajectory reconstruction.

After tracking, an additional filtering step was applied to exclude tracks that were too short or inconsistent, thereby improving the reliability of the flow analysis. The resulting particle tracks, which visualize the flow paths of the detected microspheres, are illustrated in Figure 4-13. These trajectories provide critical insight into the motion behavior, velocity patterns, and potential interactions of particles within the microchannel environment.

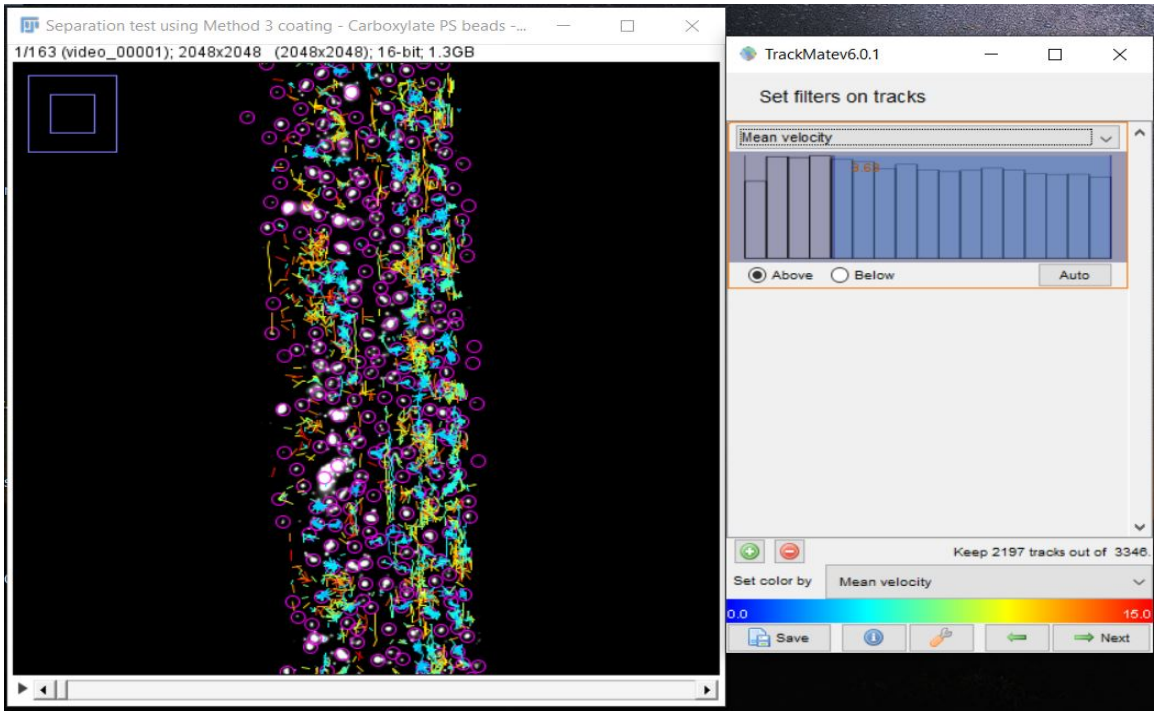

Figure 4-13: The resulting particle tracks showing the flow paths of particles detected

Track schemes and analysis details are displayed in the next panel for further analysis. The mean velocity of each particle track was obtained via the analysis data provided, and the mean velocity of the particle tracks for amino- and carboxyl-modified microspheres were calculated separately. This allows for a comparative evaluation of how different surface functionalization influence microsphere mobility within the coated microchannel.

These results provide insights into the interaction between the modified particle surfaces and the coated microchannel walls. Additionally, differences in flow behavior also reflect variations in surface charge, hydrodynamic properties, or adhesion tendencies of the modified microspheres.

Referring to the particle speed values obtained from the ImageJ analysis, the mean flow speed of carboxyl modified particles were found to be 1.266X whereas the mean flow speed of amino modified particles was 2.164X. It can be observed that the mean flow speed of carboxyl modified microspheres is lower than the mean flow speed of amino modified microspheres.

The observed flow speed difference of functionalized microspheres within the silica coated PMMA microchannel can be attributed to differences in surface chemistry and their resulting interactions with the silica gel coated channel wall. Specifically, microspheres functionalized with these polar functional groups exhibit varying affinities to the silica gel surface due to differences in intermolecular forces, such as hydrogen bonding, electrostatic interactions, and van der Waals forces.

Silica surfaces are inherently polar, and they interact strongly with polar functional groups. Carboxyl modified particles, being more negatively charged at neutral pH, exhibit stronger attractive interactions with the polar silica coating, which leads to increased adhesion that reduce their flow velocity. In contrast, amino-modified particles, which carry a more neutral or positively charged surface, exhibit weaker interactions with the silica surface and thus experience less resistance, which allows them to move more freely through the microchannel. This differential interaction within the coated microchannel leads to an effective separation based on surface functionalization.

The experimental data confirm this behavior, as carboxyl modified particles showed a lower mean flow speed which is 1.266X compared to the speed of amino modified particles, 2.164X. This variation in particle flow speeds can be incorporated to get a mixture of carboxyl modified and amino modified particles separated, given that they have required flow length to achieve effective separation. Thus, it can be concluded that the proposed technique has the potential to effectively separate carbon microsphere based on their surface properties.

4.3 Determination of the optimum conditions which enable separation of heterogeneous carbon microspheres

Under this section the optimization of the separation through a microfluidic channel was done enhancing the diffusive transport of functionalized nanoparticles. The study focuses on identifying the most effective conditions to promote selective separation of different surface characteristics.

4.3.1 Analysis of diffusive transport of nanoparticles

The diffusion of nanoparticles occurs along the length of the channel starting from the interface between nanoparticle suspension and water. Nanoparticle concentration was assumed zero throughout the channel beyond the interface. When diffusion starts to occur, the concentration begins to change, and the measured nanoparticle concentrations was fitted to Fick's second law model as shown in equation (1).

$$\frac{\partial C(x,t)}{\partial t} = D_F \frac{\partial^2 C(x,t)}{\partial x^2} \qquad (1)$$

where, $\frac{\partial C(x,t)}{\partial t}$ demonstrates the concentration variation with time, D_f is the diffusion coefficient, t is the time, x is the diffusion distance along the channel, $C(x,t)$ is the nanoparticle concentration at x distance at time t, and $\frac{\partial^2 C}{\partial x^2}$ represents the second derivative of concentration with respect to diffusion distance.

The analytical solution of Fick's second law model is given in equation (2).

$$C(x,t) = C_0 erfc(\eta)\ ,\ \eta = \frac{x}{\sqrt{4D_F t}} \qquad (2)$$

Where, $erfc(\eta)$ is complementary error function given by 1- $erf(\eta)$, x is the length in diffusion direction, and t represents the diffusion time. The diffusion coefficient (D_F) and initial nanoparticles concentration (C_0) data were fitted using equation (1) by a nonlinear least-squares fitting algorithm. Given below in equation (3) is the stokes Einstein-relational rigid spherical particles of nano-micro scale purely undergoing Brownian motion in the liquid phase. The diffusion coefficient (D_{SE}) for rigid spherical particles of nano-micro scale purely undergoing Brownian motion in the liquid phase.

$$D_{SE} = \frac{kT}{6\pi\mu r} \qquad (3)$$

Where, D_{SE} is directly proportional to Boltzmann's constant (k) and temperature (T), and inversely proportional to the viscosity of the medium (μ) and the radius (r) of particles.

4.3.2 Optimization of separation efficiency with the effect of an external electric field on nanoparticle diffusion

With regards to the optimization of the separation of functionalized microspheres the effect of separation efficiency using an external electric field is discussed in this section. The effect of an electric field on functionalized nanoparticles which carry surface charges would be a combination of electrophoresis and diffusion.

The effect of the electric field would be different for microspheres with different functional groups. Under the application of an external electric field, both the nanoparticle in the aqueous suspension and PMMA microchannel acquire charges, and Figure 4-14 depicts the charge distribution along the microchannel wall and particle surface and the flow of nanoparticles under electric field.

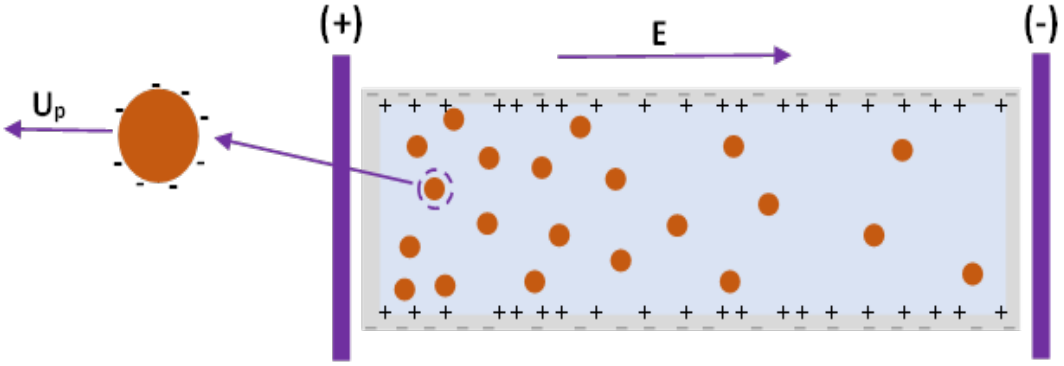

Figure 4-14: Illustration of the charge distribution along the microchannel wall and particle surface and the flow of nanoparticles under electric field

The charge on the nanoparticle and channel wall are represented using their zeta potential and due to these charges, nanoparticles get subjected to an electric force. The resulting electric force courses migration of the nanoparticles and electroosmotic flow of the solution inside the channel.

Given in equation (4) is the Helmholtz-Smoluchowski relation which provides a relation to get velocity gained by nanoparticle under an electric field.

$$u_p = \frac{\varepsilon_m}{\mu}(\zeta_w - \zeta_p)E \qquad (4)$$

Where, u_p is the velocity gained by the nanoparticles, ε_m is the medium permittivity, ζ_w is zeta potential of channel wall, and ζ_p is zeta potential of nanoparticles.

The experimental schematic diagram prepared is shown in Figure 4-15, where Figure 4-15 (a) represent the channel after the its filled with deionized water which is highlighted in purple color, Figure 4-15 (b) represent the microchannel just after the nanoparticle suspension is injected through the inlet until the nanoparticle suspension is filled up to the T-junction site as marked where the nanoparticle suspension is highlighted in green color, and Figure 4-15 (c) shows the schematic diagram of the complete experimental setup. And the experimental setup prepared according to that with copper electrodes to generate the electric field is presented in Figure 4-16.

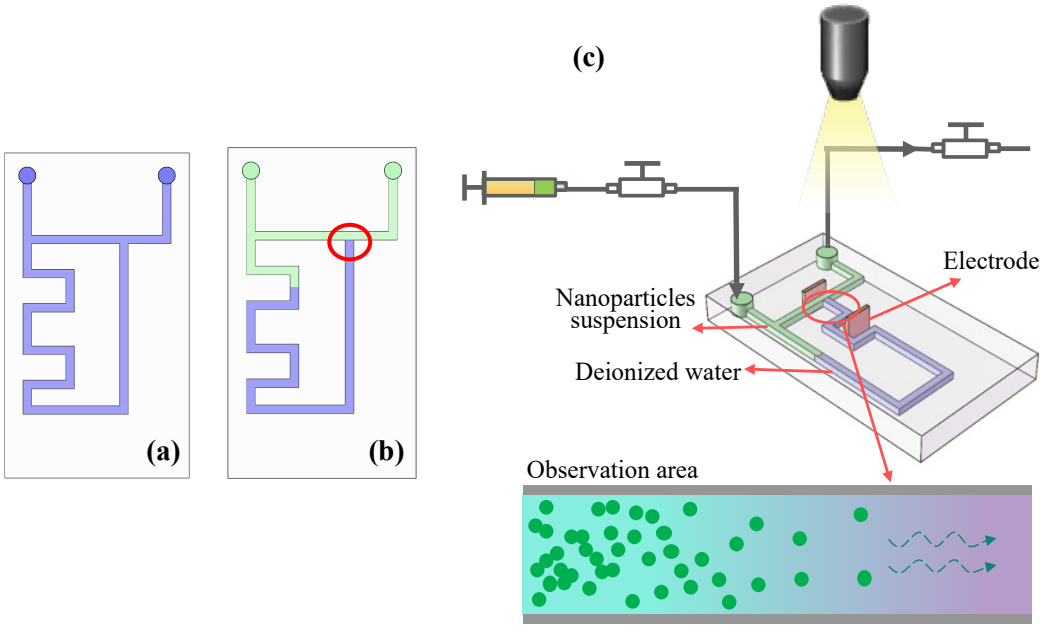

Figure 4-15: Experimental schematic diagram of (a) microchannel filled with deionized water, (b) microchannel with the nanoparticle suspension and deionized water and (c) the proposed experimental setup

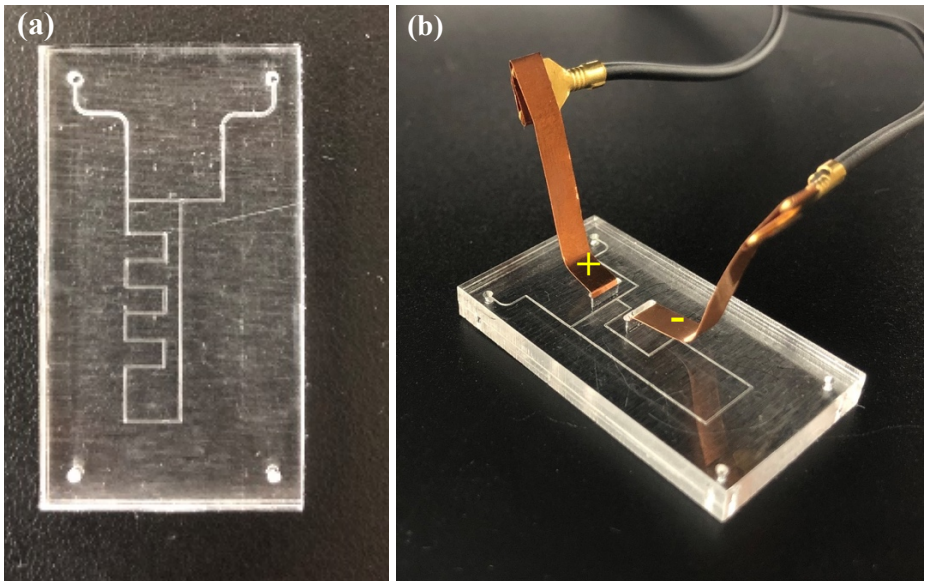

Figure 4-16 (a): PMMA microchannel prepared with engraved channel, and (b) Experimental setup with electrodes

The preparation of the calibration curve for known concentrations of nanoparticles was done initially to determine the nanoparticle concentration by correlating it with fluorescence intensity. Shown in Figure 4-17 is the calibration curve prepared for known nanoparticle concentrations ranging from 0 to 5.2 mg/ml, and the resulting fluorescence intensity.

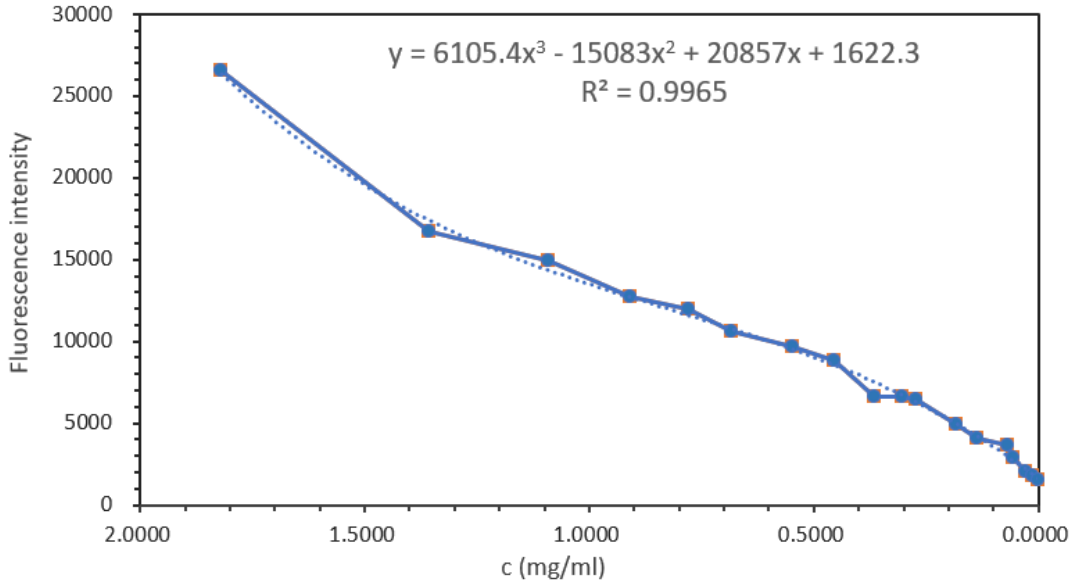

Figure 4-17: Calibration curve for the relation between fluorescence intensity and nanoparticle concentration

Over the time, the nanoparticles slowly diffuse into the water medium and images were taken covering the diffusion distance along the channel. In-situ micrographs of carboxyl-modified nanoparticles subjected to an electric field at 08, 24 and 40 minutes flow times are presented in Figure 4-18.

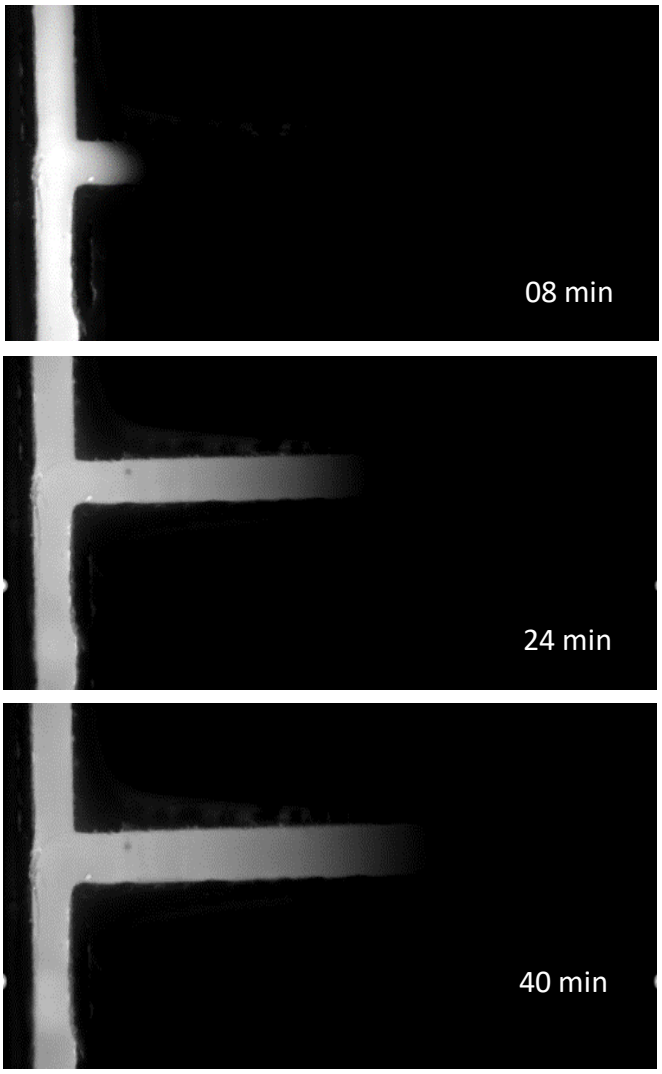

Figure 4-18: In-situ micrographs of carboxyl-modified fluorescent nanoparticles diffusing under the electric field obtained at 8, 24 and 40 minutes flow times

The variation of fluorescence intensity with the distance in the above micrographs are depicted in Figure 4-19. This intensity profile provides a quantitative representation of the spatial distribution of microspheres along the microchannel.

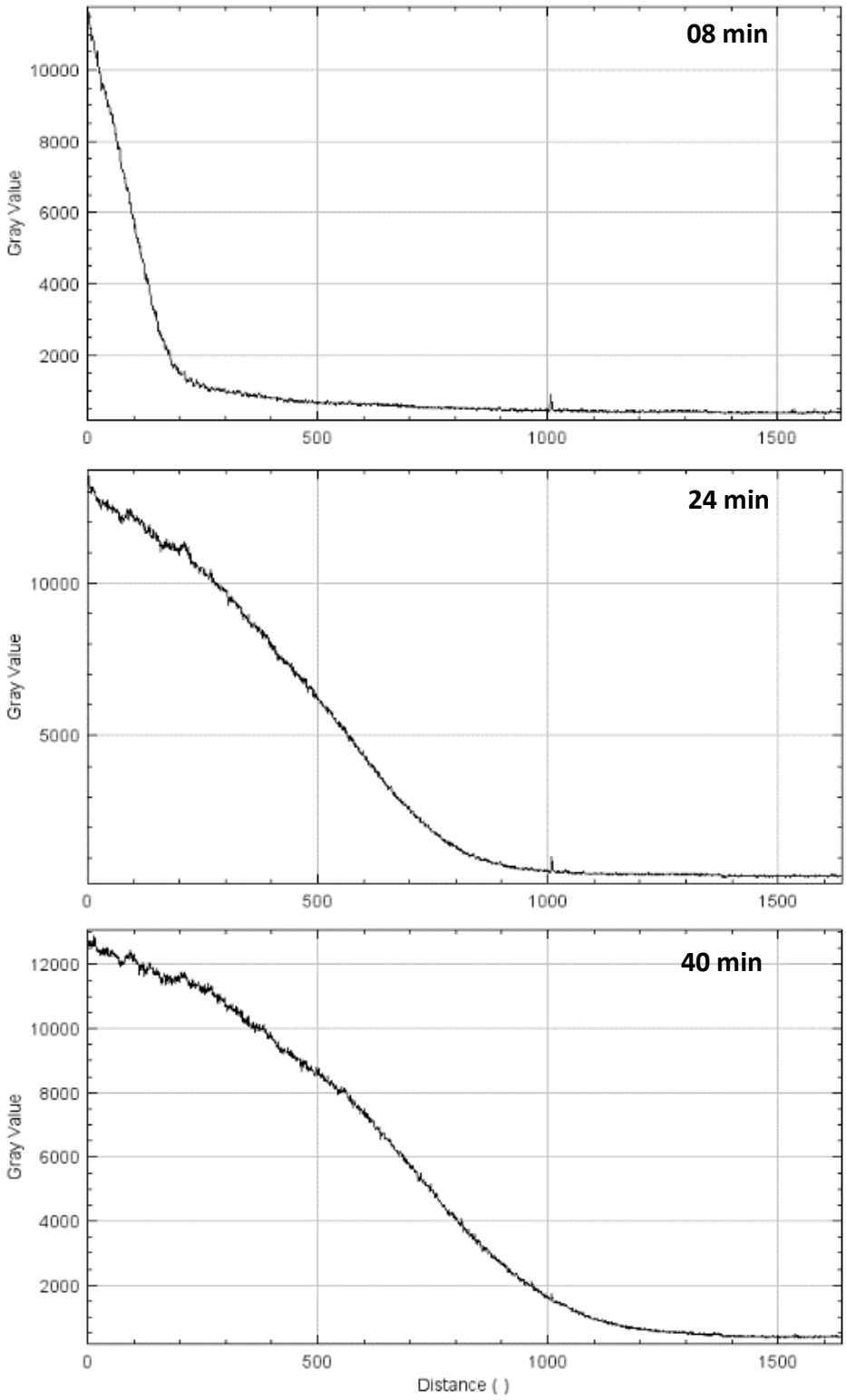

Figure 4-19: Variation of fluorescence intensity with the distance

The images obtained at 8 minutes intervals processed through pseudo-color processing using ImageJ are displayed in Figure 4-20 as in-situ images of fluorescent nanoparticles at 8, 16, 24, 32, and 40 minutes of flow times.

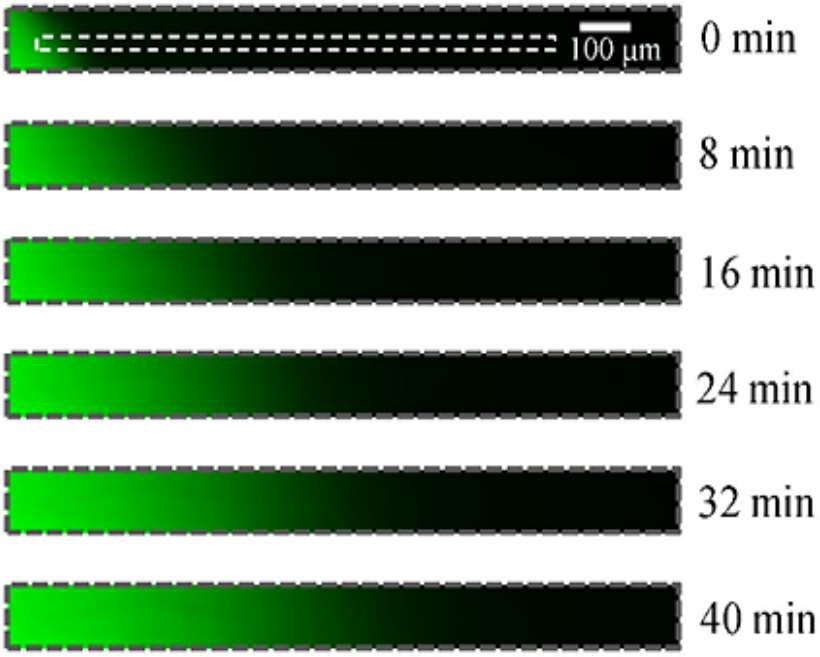

Figure 4-20: In-situ time lapse images of carboxyl modified polystyrene nanoparticles

The diffusion distance was measured starting from the fluorescence interface along the length of the channel. The distance vs. fluorescence intensity data obtained from five-time lapsed images at 8, 16, 24, 32 and 40 minutes are shown below in Figure 4-21.

Further, the corresponding nanoparticle concentrations for the fluorescence intensity profiles were determined using the calibration curve, and the constructed concentration vs. distance curve is shown in Figure 4-22.

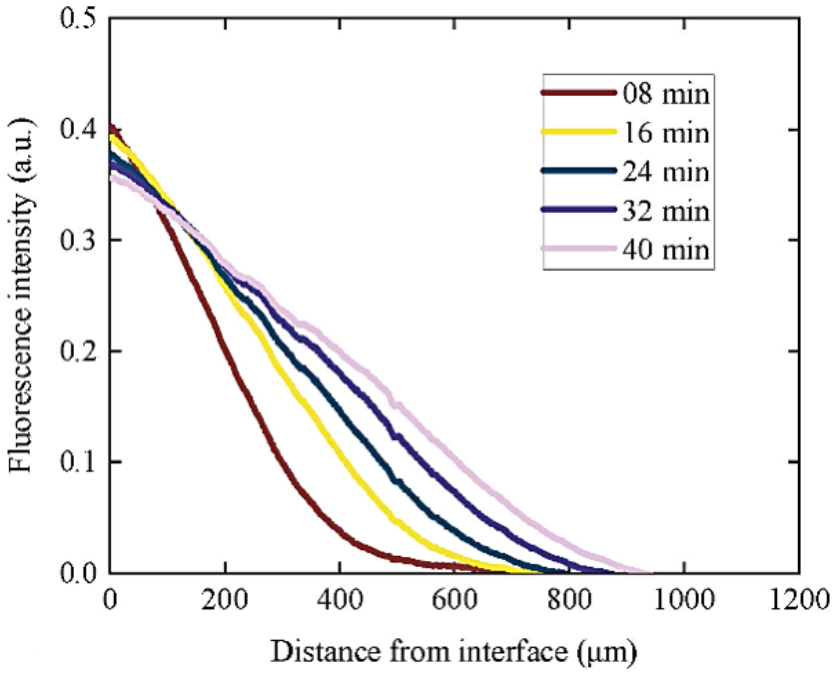

Figure 4-21: Fluorescence intensity profiles with the distance from the interface

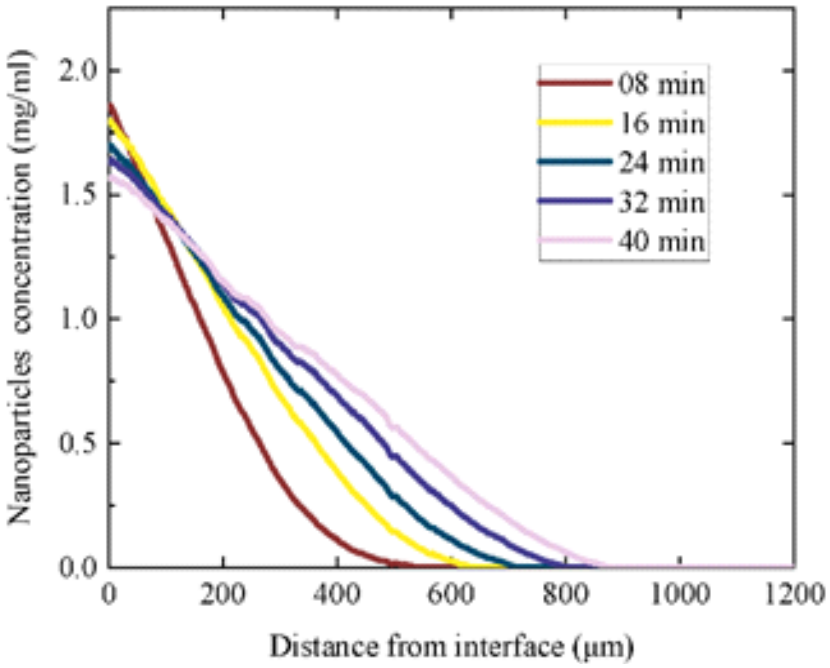

Figure 4-22: Nanoparticles concentration profiles with the distance from the interface at five flow time

4.3.3 Fick's second law model for nanoparticle diffusion

The nanoparticle concentration profiles obtained at different flow times can be fitted into the analytical function of Fick's law and the best fit analysis function curve was determined using the error function given in equation (2). Figure 4-23 illustrates the concentration profiles with the fitted curves for each concentration profile obtained at different flow times.

The average r^2 value was calculated for all times and the obtained value lies in between 0.988 – 0.998. Figure 4-24 indicates the variation of the calculated diffusion coefficient with the flow time. Diffusion coefficient of the nanoparticles calculated from the average of the diffusion coefficient values obtained at different flow times is 4.50 [± 0.26] × 10^{-11} m^2/s.

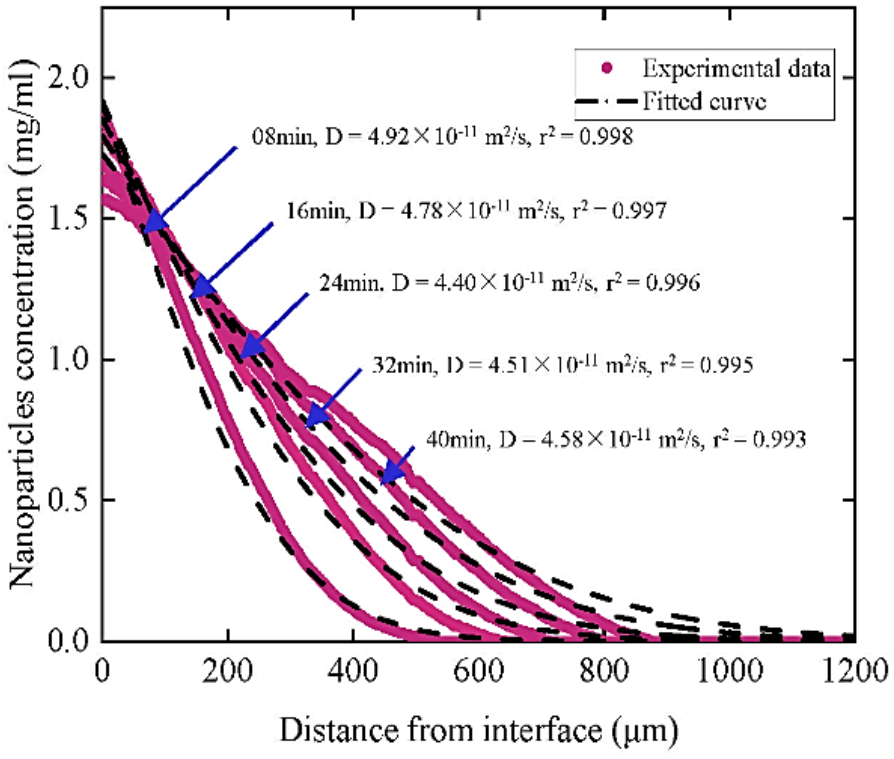

Figure 4-23: Nanoparticle concentration profiles obtained from experimental data and fitted curve using Fick's second law model

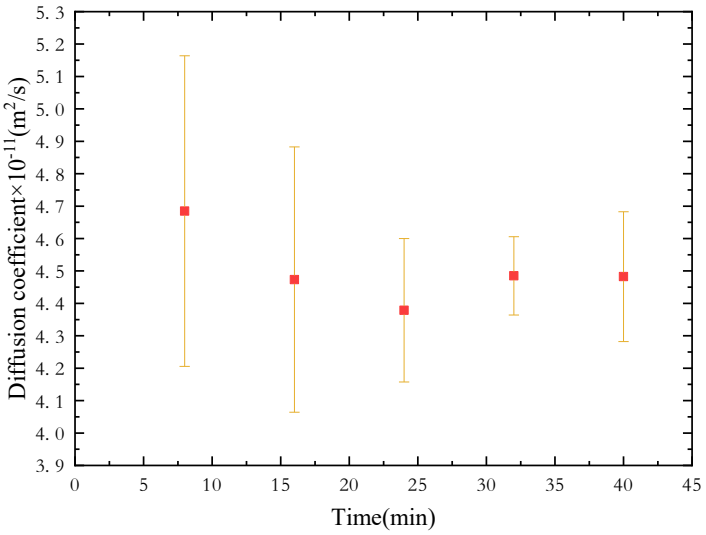

Figure 4-24: Calculated diffusion coefficient for each flow time without electric field

The observed variation in the diffusion coefficient can be attributed to several factors influencing both the system dynamics and measurement accuracy. Fluorescence quenching of certain nanoparticles may diminish signal intensity, affecting particle tracking precision. Variations in the initial nanoparticle concentration can lead to altered inter-particle interactions, thereby impacting the effective diffusion behavior. Furthermore, temperature fluctuations significantly affect diffusion rates, as the diffusion coefficient is inherently temperature dependent. These combined effects contribute to the temporal and experimental variability observed in the measured diffusion coefficient.

4.3.4 Variation of diffusion coefficient with electric field

The diffusion experiments were repeated while changing the direction of the electric field, and to compare the effect of the electric field, experiments were also conducted without the application of the electric field. Figure 4-25 represents the variation of diffusion coefficient at the different flow times when the applied electric field intensity is + 60V/cm, where the electric field would be accelerating the carboxyl modified nanoparticles. Further, Figure 4-26 represents the variation of diffusion coefficient at the different flow times when the applied electric field intensity is -60 V/cm where the applied electric field would be decelerating the carboxyl modified nanoparticles.

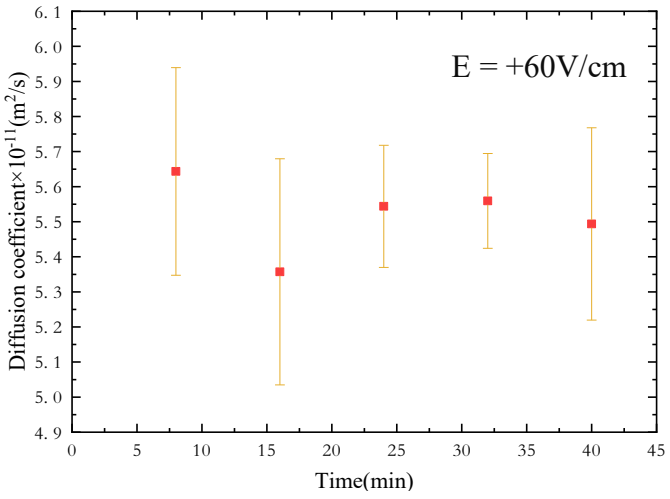

Figure 4-25: Variation of the diffusion coefficient with the flow time when E=+60V/cm

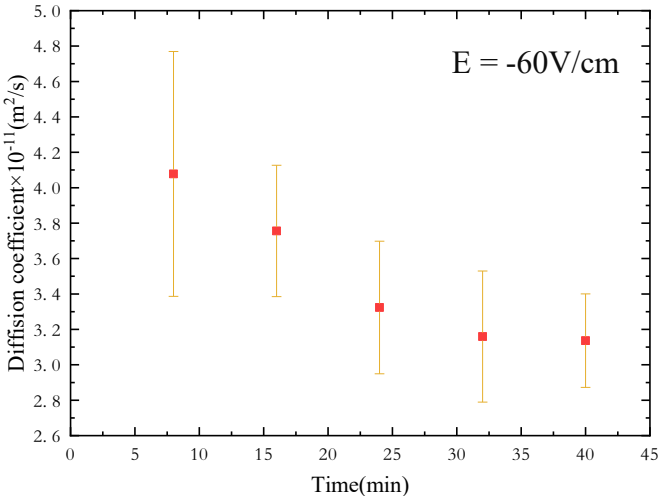

Figure 4-26: Variation of the diffusion coefficient with the flow time when E=-60V/cm

Moreover, Figure 4-24 above represents the variation of diffusion coefficient at the different flow times when the applied electric field intensity is 0 V/cm where there will not be any interferences from the applied electric field.

Graphical representation of the variation of the diffusion coefficient with the applied electric field is displayed in Figure 4-27.

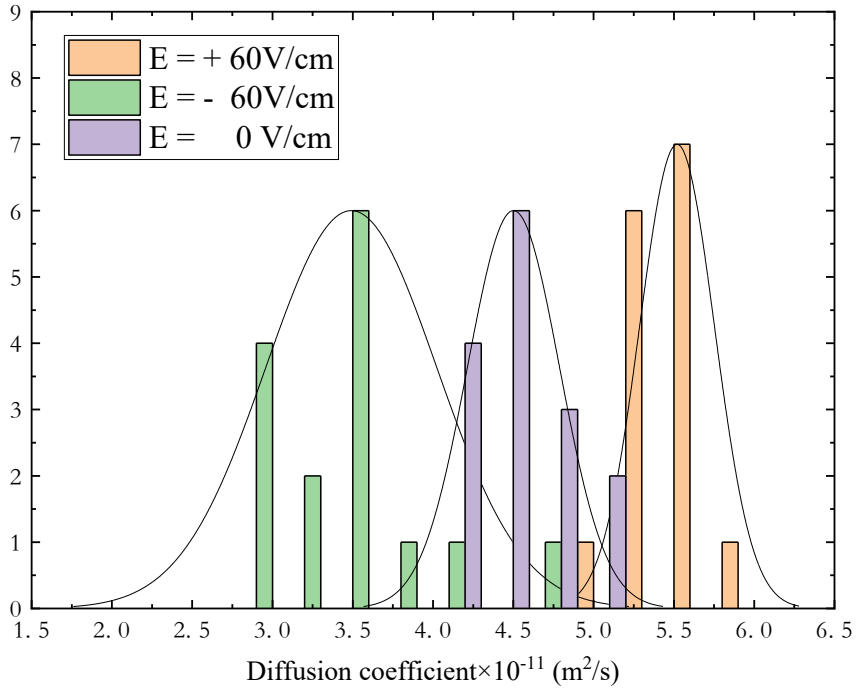

Figure 4-27: Variation of the diffusion coefficient with the electric field

Without any interferences from an external electrostatic field, the average diffusion coefficient of carboxyl-modified nanoparticles was calculated to be 4.5×10^{-11} m^2/s. With a forward electric field electric field with the intensity of +60 V/cm, the diffusion coefficient was calculated to be 5.5×10^{-11} m^2/s. In comparison with the diffusion coefficient without the application of an electric field it is evident that the diffusion coefficient has increased significantly with the application of the forward electric field.

Additionally, with the application of a reverse electric field with the intensity of -60 V/cm, the diffusion coefficients were calculated to be 3.5×10^{-11} m^2/s. Again, in comparison with the diffusion coefficient without the application of an electric field it can be observed that the diffusion coefficient has decreased with the application of the reverse electric field. Table 4.1 shows the variation of diffusion coefficient and the standard deviation of the diffusion coefficient.

Table 4.1: Variation of the diffusion coefficient with the applied electric field

	E=+60V/cm	E=-60V/cm	E=0V/cm
Diffusion coefficient average value	5.519507	3.490767	4.500927
Diffusion coefficient standard deviation	0.233658	0.531861	0.286824

The experiment was repeated for nanoparticles without any functional groups and the variation of the diffusion coefficient is depicted in Figure 4-28.

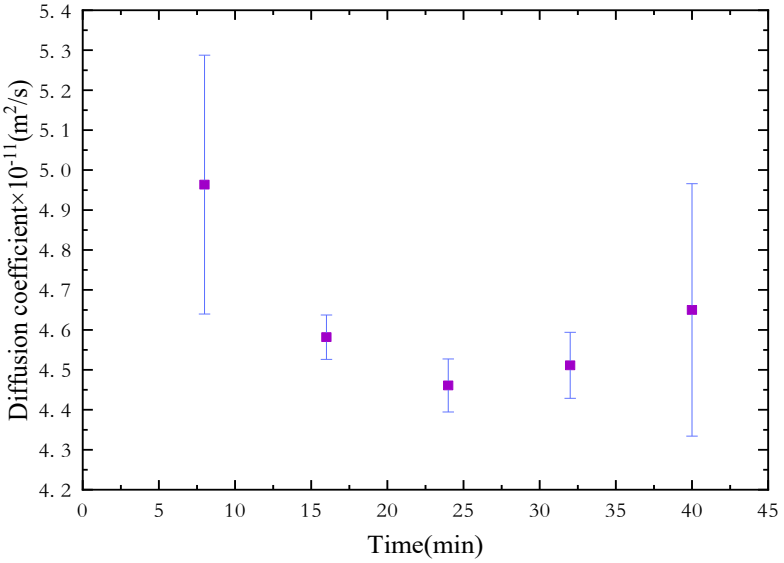

Figure 4-28: Variation of the diffusion coefficient of nanoparticles without the functional groups with the flow time when E=0V/cm

4.4 Evaluation and simulation of the effect of surface forces

As discussed above in chapter 3, evaluation and simulation of the effect of surface forces on the diffusion behavior and the separation efficiency was done using Ansys Fluent Student software by ANSYS Inc. The aim of the present study is to develop a simulation model to replicate the diffusive transport of nanoparticles inside a microchannel. The same carboxyl modified polystyrene nanoparticles were considered for the study, and they carry minor surface charges. Hence, the diffusion of nanoparticles in the current study can be influenced by an externally applied electric field as deliberated above under the previous objectives.

Flow conditions corresponding to the experimental setup was used for the model development, and a particle solution with 3.291×10^{-5} % (v/v) of carboxyl modified polystyrene nanoparticles in a water medium was supplied to the inlet point of the simulation model. Further, similar to the actual behavior within the channel the diffusion of the nanoparticles within the channel occurs via diffusion driven by the concentration gradient through the channel, without application of a momentum.

Diffusion proceeds from the nanoparticle solution-water interface near the inlet, to the water that is filled inside the microchannel. The diffusion coefficient can be defined as the proportionality constant between the species concentration gradient and the diffusion flux. The Stokes-Einstein relation, that is used to predict the diffusion behavior of spherical particle larger than the solvent molecules in a low-viscosity medium, is expressed by the equation (5).

$$D = \frac{k_B T}{6\pi\mu a} \qquad (5)$$

Where, 'D' is the diffusion coefficient, $'k_B'$ is the Boltzmann's constant, 'T' is absolute temperature, 'μ' is viscosity of the fluid medium, and 'a' is the particle radius. The Stokes-Einstein diffusion coefficient for the system was calculated to 9.0×10^{-12} m^2 s^{-1}, and it was used as the diffusion coefficient for the dilute approximation in species model.

4.4.1 Solution of the diffusion equation

Diffusion of functionalized styrene nanoparticles along the channel is governed by Fick's second law of diffusion was discussed above in equation (1), and given above in equation (2) is the solution to the Fick's second law model. The equation (2) discussed above can be rearranged as shown in equation (6) can be used to calculate the diffusion coefficient at time t via the inverse error function of the ratio between the concentration at a distance of x to the initial nanoparticle concentration. The data required for the calculation of diffusion coefficient under the electric field were obtained through the model developed through Ansys Fluent.

$$\frac{C(x,t)}{C_0} = erfc\left(\frac{x}{\sqrt{4D_F t}}\right) \qquad (6)$$

Under an externally applied electric field, nanoparticles experience electro migration. Corresponding to that, an electroosmotic flow is generates within the microchannel due to interactions with surface charges on the diffusion layer of the microchannel wall. Using the Helmholtz-Smoluchowski relation given in equation (4), the velocity gained by nanoparticles was calculated to be 1.761 x 10^{-9} ms^{-1}. The resultant velocity from both the electrophoretic velocity and electroosmotic velocities are included in this velocity.

4.4.2 Geometry and Mech development

Geometry for the fluid flow analysis can be created using ANSYS Space Claim Direct Modeler, ANSYS Design Modeler, or by importing a geometry file in an appropriate format. Present study uses ANSYS Design Modeler to create the geometry focusing on the fluid body inside the channel which is considered for the diffusion study. Shown in Figure 4-29 (a) is the fluid body with a rectangular cross section which is 100 µm in depth and 200 µm in width, and the geometry was created only considering the diffusion length of the channel.

Definition of the computational Mesh was done using ANSYS Meshing, with an element size of 10 µm. Named selections were created with the nanoparticle introduction point

defined as the inlet and the other corner of the channel was named as the outlet. Presented in Figure 4-29 (b) is the computational mesh which consist of 23331 nodes and 20000 elements.

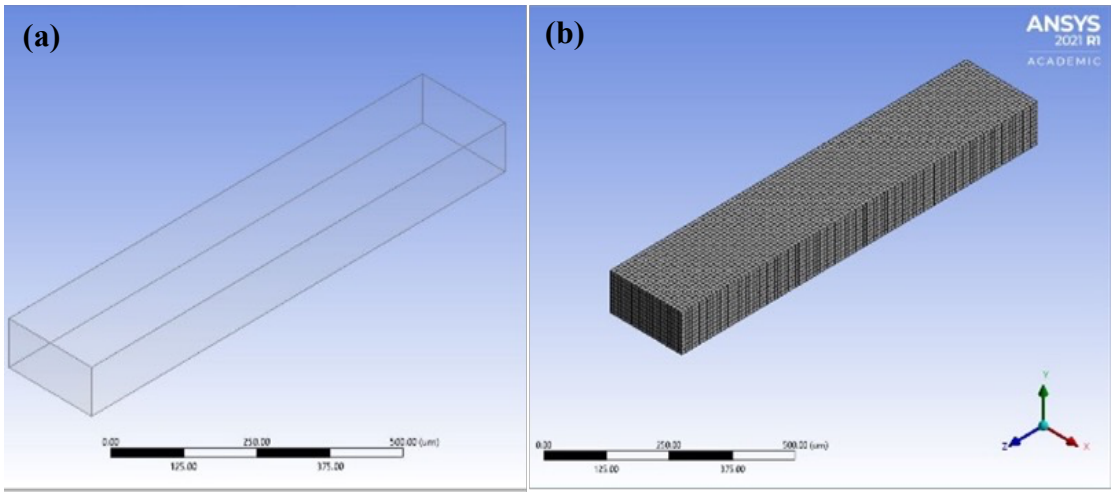

Figure 4-29: (a) channel geometry created by Ansys design modeler. (b) Computational mesh generated by Ansys meshing

DEFINE_SOURCE macro defined in UDF manual was utilized to develop the UDF and it was successfully executed with the fluent solver. It was built taking the inlet as the origin position and the diffusion distances were measured from the origin point. Moreover, the UDF was modified to get the diffusion distance, nanoparticle concentration, and flow time reported to a separate output file.

4.4.3 Development of the User Defined Function (UDF)

The UDF modified using C programming language is presented below.

```
#include "udf.h"
#include "mem.h"
#include "math.h"

DEFINE_SOURCE(electrostatic_flux,c,t,dS,eqn)

{
FILE * fp;
```

```
int dx,dy,dz,r;
real source,y,d,mc,time;
double a,v,mass,l,u;
real xc[ND_ND];

u = 0.00000000176131; /* Nanoparticle velocity */
y = C_YI(c,t,0); /* Species mass fraction */
d = C_R(c,t); /* cell density */
v = C_VOLUME(c,t); /* cell volume */
l = pow(v,(1/3));

a =l*l; /* cell dimensions */
mass = v*d*y; /* mass or nanoparticles in the cell*/
mc = y * d; /* nanoparticle concentration of the cell */
time = CURRENT_TIME;
C_CENTROID(xc,c,t);
source = (mass/(a*u)); /* additional flux due to the effect of electric field */

dS[eqn]=0;

dx = xc[0]*1000000; /* coordinates of the current particle*/
dy = xc[1]*1000000;
dz = xc[2]*1000000;

if (95<dx && dx<110 && dy<60 && dy>45 && dz<20) /* Writing output data to file*/

{
fp = fopen ("file2.txt", "a");
fprintf(fp, "%f %d %d %d %0.15lf %0.15lf\n", time, dx, dy,dz, mc, source);
fclose(fp);
}

else if (95<dx && dx<110 && dy<60 && dy>45 && dz<120 && dz>100)

{
fp = fopen ("file2.txt", "a");
fprintf(fp, "%f %d %d %d %0.15lf %0.15lf\n", time, dx, dy,dz, mc,source);
fclose(fp);
}

else if (95<dx && dx<110 && dy<60 && dy>45 && dz<220 && dz>200)
```

```
{
fp = fopen ("file2.txt", "a");
fprintf(fp, "%f %d %d %d %0.15lf %0.15lf\n", time, dx, dy,dz, mc,source);
fclose(fp);
}

else if (95<dx && dx<110 && dy<60 && dy>45 && dz<320 && dz>300)

{
fp = fopen ("file2.txt", "a");
fprintf(fp, "%f %d %d %d %0.15lf %0.15lf\n", time, dx, dy,dz, mc,source);
fclose(fp);
}

else if (95<dx && dx<110 && dy<60 && dy>45 && dz<420 && dz>400)

{
fp = fopen ("file2.txt", "a");
fprintf(fp, "%f %d %d %d %0.15lf %0.15lf\n", time, dx, dy,dz, mc,source);
fclose(fp);
}

else if (95<dx && dx<110 && dy<60 && dy>45 && dz<520 && dz>500)

{
fp = fopen ("file2.txt", "a");
fprintf(fp, "%f %d %d %d %0.15lf %0.15lf\n", time, dx, dy,dz, mc,source);
fclose(fp);
}

else if (95<dx && dx<110 && dy<60 && dy>45 && dz<620 && dz>600)

{
fp = fopen ("file2.txt", "a");
fprintf(fp, "%f %d %d %d %0.15lf %0.15lf\n", time, dx, dy,dz, mc,source);
fclose(fp);
}

return source;

}
```

The developed model was run through Ansys Fluent, and the nanoparticle concentration variation obtained from CFD-post is illustrated in Figure 4-30. When time t=0 minutes, the nanoparticle suspension concentration at the inlet of the microchannel is 3.5 mg/ml.

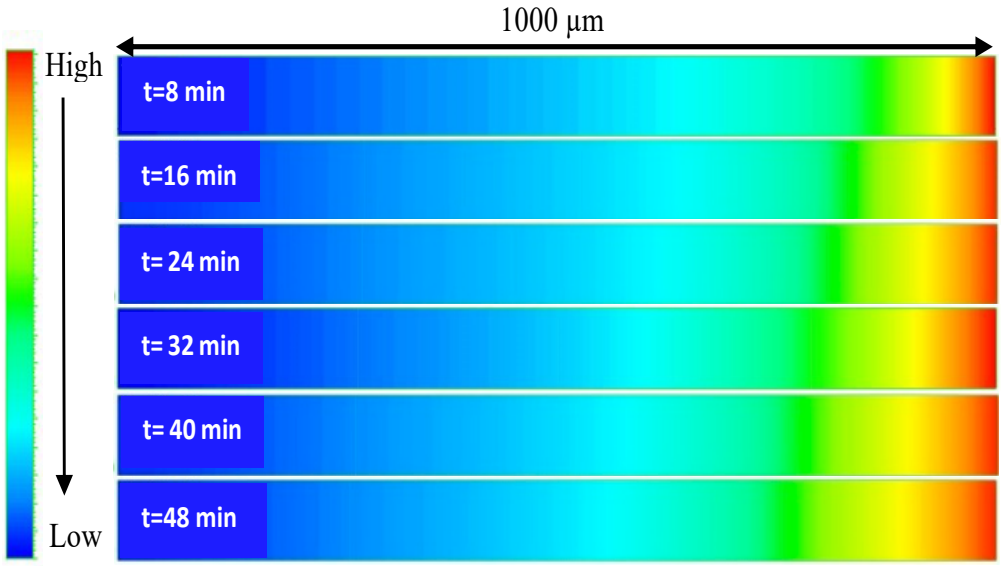

Figure 4-30: Contours of the variation of nanoparticle concentration along the microchannel

UDF was built taking the nanoparticle suspension and deionized water interface as the origin position and the diffusion distances were measured from that point. Nanoparticle concentration of different locations along the channel was exported to an output file including the respective flow time and distance from origin. Figure 4-31 presents the plot of obtained nanoparticle concentration versus the distance from the origin, at each flow time, and figure depicts the nanoparticles concentration vs. flow time, at different locations along the channel, and Figure 4-32 illustrates the nanoparticles concentration vs. flow time, at different locations along the channel.

The diffusion data recorded in the output file was used for the determination of diffusion coefficient under the influence of the external electric field using equation (6). According to the equations above ratio between the nanoparticle concentration at distance x at time t, and initial concentrations is equivalent to the complementary error function of $\frac{x}{\sqrt{4D_F t}}$.

Diffusion coefficient for the diffusion of polystyrene nanoparticles through the microchannel were calculated using $\frac{C(x,t)}{C_0}$ values and hence the value for $\frac{x}{\sqrt{4D_F t}}$ can be determined through the inverse error function value of $\frac{C(x,t)}{C_0}$.

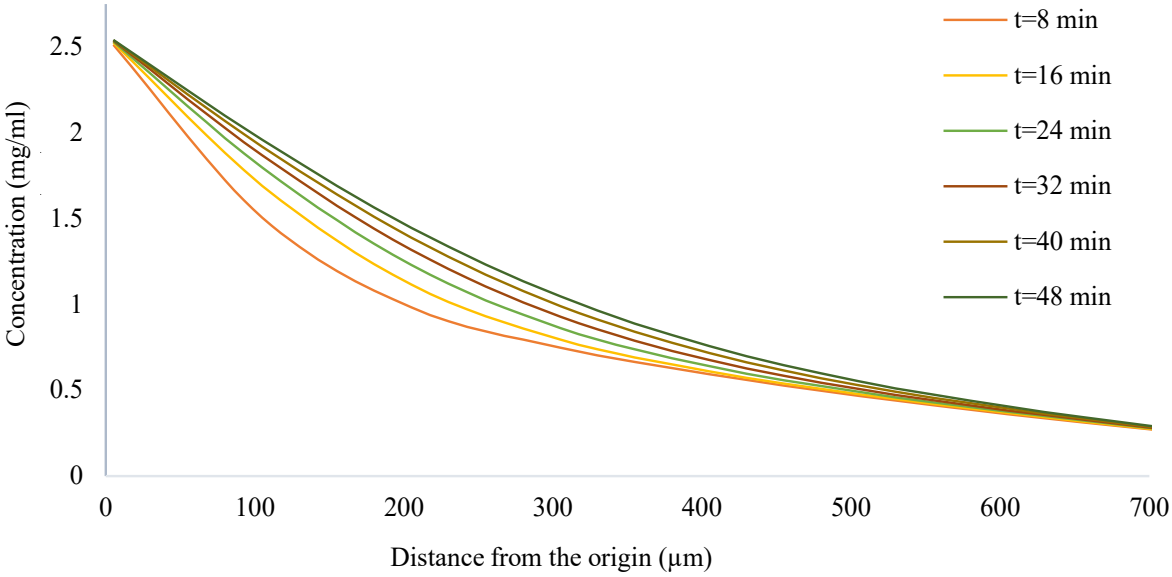

Figure 4-31: Nanoparticle concentration against the distance from the origin with flow time

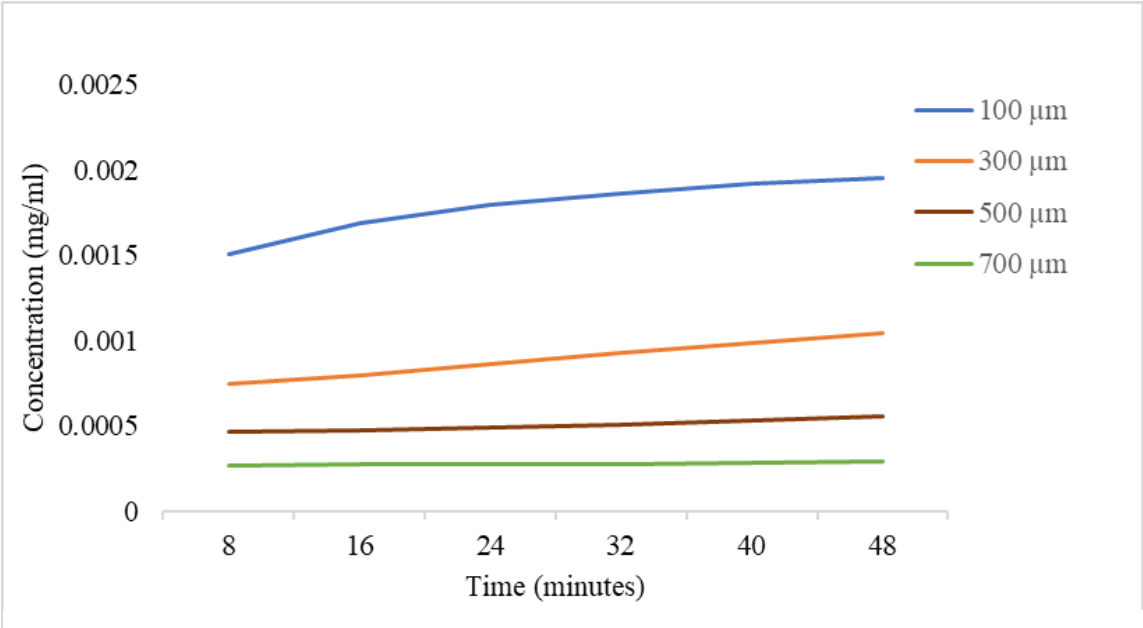

Figure 4-32: Nanoparticles concentration vs. flow time, at different locations along the channel

Table 4.2 below shows the nanoparticle concentration variation with distance and flow time, where the data at flow times of 8, 16, 24, 32, 40 and 48 minutes were used for the analysis.

Table 4.2: Nanoparticle concentration with distance and flow time

T (min) / *x* (μm)	8	16	24	32	40	48
5	0.00251	0.00252	0.00253	0.00253	0.00253	0.00253
105	0.0015	0.00169	0.00179	0.00186	0.00191	0.00195
205	0.00098	0.00111	0.00122	0.00131	0.00138	0.00144
305	0.00075	0.00079	0.00086	0.00092	0.00098	0.00104
405	0.00059	0.00060	0.00063	0.00067	0.00071	0.00075
505	0.00047	0.00047	0.00048	0.00050	0.00052	0.00055
605	0.00036	0.00036	0.00037	0.00038	0.00039	0.00040
705	0.00027	0.00027	0.00027	0.00027	0.00028	0.00028

The values of $\boldsymbol{X}\left(=\frac{\boldsymbol{x}}{\sqrt{\boldsymbol{4D_F t}}}\right)$ were determined by inverse error function value of $\left(\frac{\boldsymbol{C(x,t)}}{\boldsymbol{C_0}}\right)$, and using that the diffusion coefficient was calculated. Table 4.3 shows the calculated diffusion coefficient for flow time of 24 minutes.

Table 4.3: Calculation of diffusion coefficients when the flow time is 24 minutes

Distance (μm)	Concentration (mg/ml)	$\frac{C(x,t)}{C_0}$	$X\left(=\frac{x}{\sqrt{4D_F t}}\right)$	$D\left(=\frac{x^2}{4tX^2}\right)$
105	0.00179	0.709656	0.263269	2.761×10^{-11}
205	0.00122	0.48473	0.494066	2.988×10^{-11}
305	0.00086	0.339917	0.674813	3.546×10^{-11}
405	0.00063	0.251855	0.810242	4.337×10^{-11}
505	0.00048	0.192978	0.920526	5.225×10^{-11}
605	0.00037	0.147385	1.024478	6.054×10^{-11}
705	0.00027	0.108092	1.136198	6.684×10^{-11}

Through that the average diffusion coefficient at 24 minutes was calculated to be 4.5 x 10^{-11} m^2s^{-1}. Similarly, diffusion coefficient values corresponding to other time intervals were calculated and displayed in Figure 4-33.

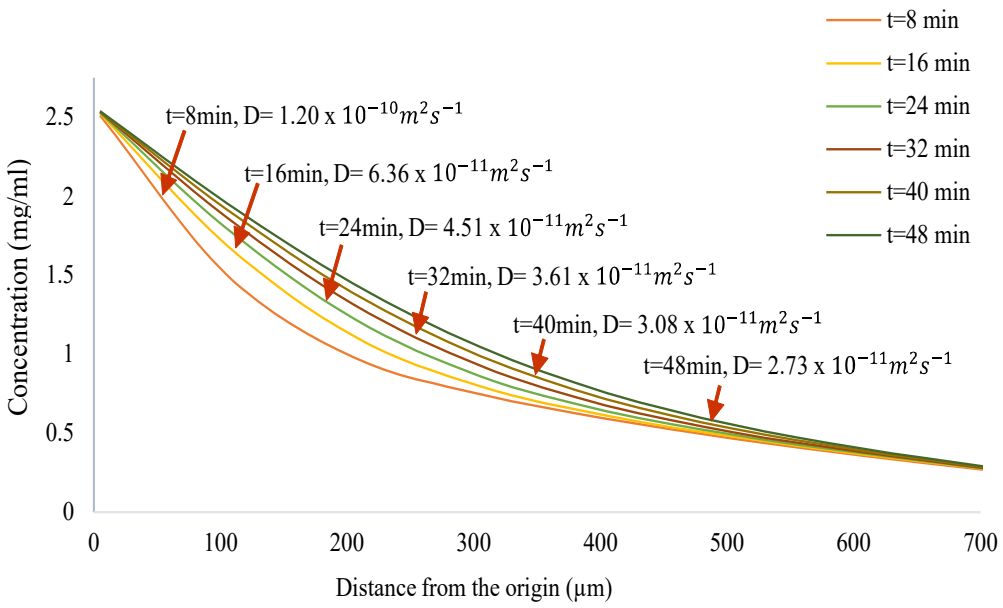

Figure 4-33: Calculated diffusion coefficient for each concentration profile

Using the diffusion coefficients at different flow times, the average diffusion coefficient was calculated to be 5.38 $\times 10^{-11}$ m^2s^{-1}.

4.4.4 Model Validation

The average diffusion coefficient was calculated to be 5.38 $\times 10^{-11}$ m^2s^{-1}, whereas the average diffusion coefficient obtained through the diffusion experiments under the electric field was 5.47 $\times$ 10^{-11} m^2 s^{-1}. Therefore, the absolute difference between the experimental and simulated diffusion coefficients is 0.09$\times 10^{-11}$ m^2/s.

This corresponds to a relative error of approximately 1.65%, indicating strong agreement between the model and experimental results.

CHAPTER 5

CONCLUSION AND RECOMMENDATIONS FOR FUTURE WORK

5.1 Conclusion

- A novel microfluidic technique was successfully developed to separate carbon microspheres with heterogeneous surface properties. The method addresses limitations in existing separation technologies that primarily focus on size and weight differences.
- The study demonstrated the critical role of surface forces between microspheres and nanoparticles, and the use of channel coatings in achieving effective separation of microspheres with different surface chemistries.
- The microfluidic separation device fabricated using PMMA, where the channel pattern was engraved on PMMA plates using computer numerical control (CNC) milling machine.
- Silica gel was selected as the suitable coating material due to its' polarity with the presence of hydroxyl groups on its surface. And the coating of the microchannels with silica gel was done using the sol-gel method, following the Stober method for nanoparticle synthesis using TEOS.
- The PMMA based microfluidic separation device is designed to differentiate and separate microspheres based on the availability of carboxyl and amino functional groups.
- Variations in the flow behavior of carboxyl-functionalized and amino-functionalized microspheres were systematically observed using fluorescence microscopy. Data analysis using ImageJ provided quantitative insights into the alterations of flow rates of different microspheres.

- Diffusion experiments within microfluidic systems using nanoparticles revealed that applying an external electric field significantly enhances the diffusion coefficient of functionalized nanoparticles.
- Electric field with an intensity of 60V/cm was applied using copper electrodes fixed to the microfluidic device.
- Experiments conducted with an external electric field highlights the potential for precise manipulation of nanoparticle transport within microfluidic devices for a variety of applications.
- Further, a simulation model was developed using CFD to show the diffusion behavior of nanoparticles under an externally applied electric field.
- ANSYS Fluent species transport model was utilized for this, and the effect of the externally applied electric field was included through a User Defined Function (UDF) which was developed using C programming language.
- The UDF was further modified to get the nanoparticle concentration data exported to an excel file for further analysis.
- Model validation against experimental data showed strong agreement, confirming its accuracy and reliability.
- The separation of bare and functionalized carbon microspheres in can be optimized by incorporating an electric field. The field will effectively accelerate or decelerate the functionalized microspheres, depending on the charge on functional groups and the direction of the applied electric field, facilitating efficient separation.
- The integration of experimental and computational approaches provides a robust framework for advancing nanoparticle separation technologies.
- This research offers potential advancements in applications with supercapacitor electrode fabrication, nanotechnology, and biomedical engineering, where precise control of material properties is essential.

5.2 Recommendations for future work

- Further studies can be carried out to prepare paper based microfluidic devices as a more economical platform to conduct microfluidic separations based on surface heterogeneity.
- The refining of the paper-based microfluidic devices can be done by exploring alternative materials and fabrication methods to improve separation efficiency and durability.
- Also, studies can focus on the separation of microspheres with additional surface functional groups such as, hydroxyl, phosphate groups to broaden the applicability of the technique developed.
- Studies can be conducted to evaluate the use of other external fields like magnetic fields to aid the separation of nanoparticles with surface functional groups.
- Moreover, the development of multi-stage microfluidic systems that combine size-based and surface heterogeneity-based separations for enhanced precision and usefulness.
- Studies can also focus on the long-term stability and reliability of the coatings and microfluidic devices for reuse.
- Additionally, enhancement of the computational model by can be done using tools other than ANSYS to incorporating more complex interactions, such as hydrodynamic and electrokinetic forces, to simulate realistic scenarios more accurately.
- Furthermore, simulation models can be developed for real-world applications, such as biomedical applications, such as separating biological nanoparticles or cells based on surface properties.

REFERENCES

[1] T. Brousse *et al.*, "Materials for electrochemical capacitors," *Springer Handbooks*, pp. 495–561, 2017, doi: 10.1007/978-3-662-46657-5_16.

[2] J. R. Miller and P. Simon, "Materials science: Electrochemical capacitors for energy management," *Science (1979)*, vol. 321, no. 5889, pp. 651–652, 2008, doi: 10.1126/science.1158736.

[3] M. Law, V. Ramar, and P. Balaya, "Na2MnSiO4 as an attractive high capacity cathode material for sodium-ion battery," *J Power Sources*, vol. 359, pp. 277–284, 2017, doi: 10.1016/j.jpowsour.2017.05.069.

[4] K. Zhang, L. L. Zhang, X. S. Zhao, and J. Wu, "Graphene/polyaniline nanofiber composites as supercapacitor electrodes," *Chemistry of Materials*, vol. 22, no. 4, pp. 1392–1401, 2010, doi: 10.1021/cm902876u.

[5] C. Zhong, Y. Deng, W. Hu, J. Qiao, L. Zhang, and J. Zhang, "A review of electrolyte materials and compositions for electrochemical supercapacitors," *Chem Soc Rev*, vol. 44, no. 21, pp. 7484–7539, 2015, doi: 10.1039/c5cs00303b.

[6] Y. Zhai, Y. Dou, D. Zhao, P. F. Fulvio, R. T. Mayes, and S. Dai, "Carbon Materials for Chemical Capacitive Energy Storage," *Advanced Materials*, vol. 23, no. 42, pp. 4828–4850, 2011, doi: 10.1002/adma.201100984.

[7] Z. Tan, G. Chen, and Y. Zhu, "Carbon-Based Supercapacitors Produced by Activation of Graphene-surporting materials," *Science (1979)*, vol. 1, no. June, pp. 211–225, 2015.

[8] P. V. Kamat, "Graphene-based nanoarchitectures. Anchoring semiconductor and metal nanoparticles on a two-dimensional carbon support," *Journal of Physical Chemistry Letters*, vol. 1, no. 2, pp. 520–527, 2010, doi: 10.1021/jz900265j.

[9] Y. Wang *et al.*, "The Journal of Physical Chemistry C Volume 113 issue 30 2009 [doi 10.1021%2Fjp902214f] Wang, Yan; Shi, Zhiqiang; Huang, Yi; Ma, Yanfeng;

Wang, Chengyan -- Supercapacitor Devices Based on Graphene Materials.pdf," *Journal of Physical Chemistry C*, vol. 113, no. 30 2009, pp. 13103–13107, 2009.

[10] G. Wang, L. Zhang, and J. Zhang, "A review of electrode materials for electrochemical supercapacitors," *Chem Soc Rev*, vol. 41, no. 2, pp. 797–828, 2012, doi: 10.1039/c1cs15060j.

[11] L. Zhang and X. S. Zhao, "Carbon-based materials as supercapacitor electrodes," *Chem Soc Rev*, vol. 38, no. 9, pp. 2520–2531, 2009, doi: 10.1039/b813846j.

[12] H. Jiang, P. S. Lee, and C. Li, "3D carbon based nanostructures for advanced supercapacitors," *Energy Environ Sci*, vol. 6, no. 1, pp. 41–53, 2013, doi: 10.1039/c2ee23284g.

[13] W. Gu and G. Yushin, "Review of nanostructured carbon materials for electrochemical capacitor applications: Advantages and limitations of activated carbon, carbide-derived carbon, zeolite-templated carbon, carbon aerogels, carbon nanotubes, onion-like carbon, and graphene," *Wiley Interdiscip Rev Energy Environ*, vol. 3, no. 5, pp. 424–473, 2014, doi: 10.1002/wene.102.

[14] M. Sawangphruk *et al.*, "High-performance supercapacitors based on silver nanoparticle-polyaniline- graphene nanocomposites coated on flexible carbon fiber paper," *J Mater Chem A Mater*, vol. 1, no. 34, pp. 9630–9636, 2013, doi: 10.1039/c3ta12194a.

[15] Y. Zhu *et al.*, "Graphene and graphene oxide: Synthesis, properties, and applications," *Advanced Materials*, vol. 22, no. 35, pp. 3906–3924, 2010, doi: 10.1002/adma.201001068.

[16] Q. Cheng, J. Tang, J. Ma, H. Zhang, N. Shinya, and L. C. Qin, "Graphene and carbon nanotube composite electrodes for supercapacitors with ultra-high energy density," *Physical Chemistry Chemical Physics*, vol. 13, no. 39, pp. 17615–17624, 2011, doi: 10.1039/c1cp21910c.

[17] M. F. El-Kady and R. B. Kaner, “Scalable fabrication of high-power graphene micro-supercapacitors for flexible and on-chip energy storage,” *Nat Commun*, vol. 4, pp. 1475–1479, 2013, doi: 10.1038/ncomms2446.

[18] Y. Xu, Z. Lin, X. Huang, Y. Liu, Y. Huang, and X. Duan, “Flexible solid-state supercapacitors based on three-dimensional graphene hydrogel films,” *ACS Nano*, vol. 7, no. 5, pp. 4042–4049, 2013, doi: 10.1021/nn4000836.

[19] P. Song, X. Zhang, M. Sun, X. Cui, and Y. Lin, “Synthesis of graphene nanosheets via oxalic acid-induced chemical reduction of exfoliated graphite oxide,” *RSC Adv*, vol. 2, no. 3, pp. 1168–1173, 2012, doi: 10.1039/c1ra00934f.

[20] A. Elmouwahidi, E. Bailón-García, A. F. Pérez-Cadenas, A. Celzard, V. Fierro, and F. Carrasco-Marín, “Carbon Microspheres with Tailored Texture and Surface Chemistry As Electrode Materials for Supercapacitors,” *ACS Sustain Chem Eng*, vol. 9, no. 1, pp. 541–551, 2021, doi: 10.1021/acssuschemeng.0c08024.

[21] S. Dalvand *et al.*, “A review on carbon material-metal oxide-conducting polymer and ionic liquid as electrode materials for energy storage in supercapacitors,” *Ionics (Kiel)*, vol. 30, no. 4, pp. 1857–1870, 2024, doi: 10.1007/s11581-024-05426-3.

[22] C. Ma, X. Chen, D. Long, J. Wang, W. Qiao, and L. Ling, “High-surface-area and high-nitrogen-content carbon microspheres prepared by a pre-oxidation and mild KOH activation for superior supercapacitor,” *Carbon N Y*, vol. 118, pp. 699–708, 2017, doi: 10.1016/j.carbon.2017.03.075.

[23] P. Forouzandeh, V. Kumaravel, and S. C. Pillai, “Electrode materials for supercapacitors: A review of recent advances,” *Catalysts*, vol. 10, no. 9, pp. 1–73, 2020, doi: 10.3390/catal10090969.

[24] H. Lyu *et al.*, “Bis(trimethylsilyl) 2-fluoromalonate derivatives as electrolyte additives for high voltage lithium ion batteries,” *J Power Sources*, vol. 412, no. August 2018, pp. 527–535, 2019, doi: 10.1016/j.jpowsour.2018.11.083.

[25] S. Kerisit, B. Schwenzer, and M. Vijayakumar, “Effects of oxygen-containing functional groups on supercapacitor performance,” *Journal of Physical Chemistry Letters*, vol. 5, no. 13, pp. 2330–2334, 2014, doi: 10.1021/jz500900t.

[26] A. Elmouwahidi, E. Bailón-García, A. F. Pérez-Cadenas, A. Celzard, V. Fierro, and F. Carrasco-Marín, “Carbon Microspheres with Tailored Texture and Surface Chemistry As Electrode Materials for Supercapacitors,” *ACS Sustain Chem Eng*, vol. 9, no. 1, pp. 541–551, 2021, doi: 10.1021/acssuschemeng.0c08024.

[27] A. G. Olabi, Q. Abbas, M. A. Abdelkareem, A. H. Alami, M. Mirzaeian, and E. T. Sayed, “Carbon-Based Materials for Supercapacitors: Recent Progress, Challenges and Barriers,” *Batteries*, vol. 9, no. 1, 2023, doi: 10.3390/batteries9010019.

[28] A. Burk, “Ultracapacitors: why, how, and where is the technology,” *J Power Sources*, vol. 91, no. 1, pp. 37–50, 2000.

[29] “Batteries In A Portable World,” 2021.

[30] H. Kelly-Holmes, “Advertising as multilingual communication,” *Advertising as Multilingual Communication*, vol. 45, pp. 1–206, 2016, doi: 10.1057/9780230503014.

[31] C. Meng, O. Z. Gall, and P. P. Irazoqui, “A flexible super-capacitive solid-state power supply for miniature implantable medical devices,” *Biomed Microdevices*, vol. 15, no. 6, pp. 973–983, 2013, doi: 10.1007/s10544-013-9789-1.

[32] R. Dubey and V. Guruviah, “Review of carbon-based electrode materials for supercapacitor energy storage,” *Ionics (Kiel)*, vol. 25, no. 4, pp. 1419–1445, 2019, doi: 10.1007/s11581-019-02874-0.

[33] T. Brousse, D. Bélanger, and J. W. Long, “To Be or Not To Be Pseudocapacitive?,” *J Electrochem Soc*, vol. 162, no. 5, pp. A5185–A5189, 2015, doi: 10.1149/2.0201505jes.

[34] G. Gautham Prasad, N. Shetty, S. Thakur, Rakshitha, and K. B. Bommegowda, “Supercapacitor technology and its applications: A review,” *IOP Conf Ser Mater Sci Eng*, vol. 561, no. 1, 2019, doi: 10.1088/1757-899X/561/1/012105.

[35] J. Zhang, M. Gu, and X. Chen, “Supercapacitors for renewable energy applications: A review,” *Micro and Nano Engineering*, vol. 21, no. October, p. 100229, 2023, doi: 10.1016/j.mne.2023.100229.

[36] M. T. Jeena *et al.*, “A siloxane-incorporated copolymer as an in situ cross-linkable binder for high performance silicon anodes in Li-ion batteries,” *Nanoscale*, vol. 8, no. 17, pp. 9245–9253, 2016, doi: 10.1039/c6nr01559j.

[37] X. T. Yang, Z. G. Liang, Y. J. Yuan, J. L. Yang, and H. Xia, “Preparation and electrochemical performance of porous carbon nanosphere,” *Wuli Xuebao/Acta Physica Sinica*, vol. 66, no. 4, 2017, doi: 10.7498/aps.66.048101.

[38] Y. Lu, C. Yang, H. Rong, and D. Pan, “Preparation of porous carbon microspheres,” *J Appl Polym Sci*, vol. 102, no. 1, pp. 798–803, 2006, doi: 10.1002/app.24112.

[39] H. Kim, M. E. Fortunato, H. Xu, J. H. Bang, and K. S. Suslick, “Carbon microspheres as supercapacitors,” *Journal of Physical Chemistry C*, vol. 115, no. 42, pp. 20481–20486, 2011, doi: 10.1021/jp207135g.

[40] P. A. T. Kelly, C. J. Davis, and G. M. Goodwin, “Differential patterns of local cerebral glucose utilization in response to 5-hydroxytryptamine, agonists,” *Neuroscience*, vol. 25, no. 3, pp. 907–915, 1988, doi: 10.1016/0306-4522(88)90044-9.

[41] H. Wang *et al.*, “Mn3O4-graphene hybrid as a high-capacity anode material for lithium ion batteries,” *J Am Chem Soc*, vol. 132, no. 40, pp. 13978–13980, 2010, doi: 10.1021/ja105296a.

[42] T. Najam *et al.*, “Nanostructure engineering by surficial induced approach: Porous metal oxide-carbon nanotube composite for lithium-ion battery,” *Materials Science and Engineering: B*, vol. 273, no. December 2020, p. 115417, 2021, doi: 10.1016/j.mseb.2021.115417.

[43] V. V. Khedekar, S. Mohammed Zaeem, and S. Das, “Graphene-metal oxide nanocomposites for supercapacitors: A perspective review,” *Adv Mater Lett*, vol. 9, no. 1, pp. 2–19, 2018, doi: 10.5185/amlett.2018.1932.

[44] Xian Jian *et al.*, “Carbon-Based Electrode Materials for Supercapacitor: Progress, Challenges and Prospective Solutions,” *J. of Electrical Engineering*, vol. 4, no. 2, Feb. 2016, doi: 10.17265/2328-2223/2016.02.004.

[45] H. Kim, M. E. Fortunato, H. Xu, J. H. Bang, and K. S. Suslick, “Carbon microspheres as supercapacitors,” *Journal of Physical Chemistry C*, vol. 115, no. 42, pp. 20481–20486, 2011, doi: 10.1021/jp207135g.

[46] C. Garnier *et al.*, “Activated carbon surface heterogeneity seen by parallel probing by inverse liquid chromatography at the solid/liquid interface and by gas adsorption analysis at the solid/gas interface,” *Carbon N Y*, vol. 45, no. 2, pp. 240–247, 2007, doi: 10.1016/j.carbon.2006.10.004.

[47] M. Sevilla and A. B. Fuertes, “The production of carbon materials by hydrothermal carbonization of cellulose,” *Carbon N Y*, vol. 47, no. 9, pp. 2281–2289, 2009, doi: 10.1016/j.carbon.2009.04.026.

[48] N. Zhao *et al.*, “Hierarchical porous carbon with graphitic structure synthesized by a water soluble template method,” *Mater Lett*, vol. 87, pp. 77–79, 2012, doi: 10.1016/j.matlet.2012.07.085.

[49] M. D. Levi *et al.*, “Solving the capacitive paradox of 2D MXene using electrochemical quartz-crystal admittance and in situ electronic conductance measurements,” *Adv Energy Mater*, vol. 5, no. 1, pp. 1–11, 2015, doi: 10.1002/aenm.201400815.

[50] J. Chmiola, P. L. T. Celine Largeot, P. Simon, and Y. Gogotsi, “Monolithic carbide-derived carbon films for micro-supercapacitors,” *Science (1979)*, vol. 328, no. 5977, pp. 480–483, 2010, doi: 10.1126/science.1184126.

[51] C. Liu, F. Li, M. Lai-Peng, and H. M. Cheng, “Advanced materials for energy storage,” *Advanced Materials*, vol. 22, no. 8, pp. 28–62, 2010, doi: 10.1002/adma.200903328.

[52] J. Yan, Q. Wang, T. Wei, and Z. Fan, “Recent advances in design and fabrication of electrochemical supercapacitors with high energy densities,” *Adv Energy Mater*, vol. 4, no. 4, 2014, doi: 10.1002/aenm.201300816.

[53] J. Y. Miao *et al.*, “Synthesis and properties of carbon nanospheres grown by CVD using Kaolin supported transition metal catalysts,” *Carbon N Y*, vol. 42, no. 4, pp. 813–822, 2004, doi: 10.1016/j.carbon.2004.01.053.

[54] Z. N. Tetana, S. D. Mhlanga, and N. J. Coville, “Chemical vapour deposition syntheses and characterization of boron-doped hollow carbon spheres,” *Diam Relat Mater*, vol. 74, no. 2016, pp. 70–80, 2017, doi: 10.1016/j.diamond.2017.02.005.

[55] R. Panickar, C. B. Sobhan, and S. Chakravorti, “Chemical vapor deposition synthesis of carbon spheres: Effects of temperature and hydrogen,” *Vacuum*, vol. 172, no. November 2019, p. 109108, 2020, doi: 10.1016/j.vacuum.2019.109108.

[56] M. M. Titirici, M. Antonietti, and A. Thomas, “A generalized synthesis of metal oxide hollow spheres using a hydrothermal approach,” *Chemistry of Materials*, vol. 18, no. 16, pp. 3808–3812, 2006, doi: 10.1021/cm052768u.

[57] M. Sevilla and A. B. Fuertes, “The production of carbon materials by hydrothermal carbonization of cellulose,” *Carbon N Y*, vol. 47, no. 9, pp. 2281–2289, 2009, doi: 10.1016/j.carbon.2009.04.026.

[58] Q. Wu, W. Li, J. Tan, Y. Wu, and S. Liu, “Hydrothermal carbonization of carboxymethylcellulose: One-pot preparation of conductive carbon microspheres and water-soluble fluorescent carbon nanodots,” *Chemical Engineering Journal*, vol. 266, pp. 112–120, 2015, doi: 10.1016/j.cej.2014.12.089.

[59] V. Pavlenko *et al.*, *A comprehensive review of template-assisted porous carbons: Modern preparation methods and advanced applications*, vol. 149, no. May. 2022. doi: 10.1016/j.mser.2022.100682.

[60] P. Gurunathan, M. G. Karthick Babu, and K. Ramesha, “ Template assisted synthesis of Sn@C microspheres and SnO 2 @C micro bowls as anode for Li-Ion batteries ,” *Energy Storage*, vol. 2, no. 5, pp. 1–14, 2020, doi: 10.1002/est2.152.

[61] C. Wang *et al.*, “Recent progress in template-assisted synthesis of porous carbons for supercapacitors,” *Advanced Powder Materials*, vol. 1, no. 2, p. 100018, 2022, doi: 10.1016/j.apmate.2021.11.005.

[62] Y. Xie, D. Kocaefe, C. Chen, and Y. Kocaefe, “Review of Research on Template Methods in Preparation of Nanomaterials,” *J Nanomater*, vol. 2016, 2016, doi: 10.1155/2016/2302595.

[63] J. Xu *et al.*, “Fabrication of wrinkled carbon microspheres and the effect of surface roughness on the microwave absorbing properties,” *Chemical Engineering Journal*, vol. 401, p. 126027, 2020, doi: 10.1016/j.cej.2020.126027.

[64] H. Wang, X. Li, J. Peng, Y. Cai, J. Jiang, and Q. Li, “Control of the interface graphitized/amorphous carbon of biomass-derived carbon microspheres for symmetric supercapacitors,” *Nanoscale Adv*, vol. 3, no. 16, pp. 4858–4865, 2021, doi: 10.1039/d1na00262g.

[65] L. Frusteri *et al.*, “Carbon microspheres preparation, graphitization and surface functionalization for glycerol etherification,” *Catal Today*, vol. 277, pp. 68–77, 2016, doi: 10.1016/j.cattod.2016.02.044.

[66] A. Elmouwahidi, E. Bailón-García, A. F. Pérez-Cadenas, A. Celzard, V. Fierro, and F. Carrasco-Marín, “Carbon Microspheres with Tailored Texture and Surface Chemistry As Electrode Materials for Supercapacitors,” *ACS Sustain Chem Eng*, vol. 9, no. 1, pp. 541–551, 2021, doi: 10.1021/acssuschemeng.0c08024.

[67] H. Kim, M. E. Fortunato, H. Xu, J. H. Bang, and K. S. Suslick, “Carbon microspheres as supercapacitors,” *Journal of Physical Chemistry C*, vol. 115, no. 42, pp. 20481–20486, 2011, doi: 10.1021/jp207135g.

[68] H. Kim, M. E. Fortunato, H. Xu, J. H. Bang, and K. S. Suslick, “Carbon microspheres as supercapacitors,” *Journal of Physical Chemistry C*, vol. 115, no. 42, pp. 20481–20486, 2011, doi: 10.1021/jp207135g.

[69] A. Peigney, C. Laurent, E. Flahaut, R. R. Bacsa, and A. Rousset, “CNTの比表面積の求め方.pdf,” *Carbon N Y*, vol. 39, p. 507, 2001.

[70] A. G. Pandolfo and A. F. Hollenkamp, “Carbon properties and their role in supercapacitors,” *J Power Sources*, vol. 157, no. 1, pp. 11–27, 2006, doi: 10.1016/j.jpowsour.2006.02.065.

[71] C. Liang, Z. Li, and S. Dai, “Mesoporous carbon materials: Synthesis and modification,” *Angewandte Chemie - International Edition*, vol. 47, no. 20, pp. 3696–3717, 2008, doi: 10.1002/anie.200702046.

[72] A. Lenshof and T. Laurell, “Continuous separation of cells and particles in microfluidic systems,” *Chem Soc Rev*, vol. 39, no. 3, pp. 1203–1217, 2010, doi: 10.1039/b915999c.

[73] L. R. Radovic, A. B. Silva-Tapia, and F. Vallejos-Burgos, “Oxygen migration on the graphene surface. 1. Origin of epoxide groups,” *Carbon N Y*, vol. 49, no. 13, pp. 4218–4225, 2011, doi: 10.1016/j.carbon.2011.05.059.

[74] T. Jain *et al.*, “Corrigendum to ‘End-to-end assembly of gold nanorods via oligopeptide linking and surfactant control’ [J. Colloid Interface Sci. 376 (2012) 83-90],” *J Colloid Interface Sci*, vol. 384, no. 1, p. 217, 2012, doi: 10.1016/j.jcis.2012.06.059.

[75] S. Kang, M. Pinault, L. D. Pfefferle, and M. Elimelech, “Single-walled carbon nanotubes exhibit strong antimicrobial activity,” *Langmuir*, vol. 23, no. 17, pp. 8670–8673, 2007, doi: 10.1021/la701067r.

[76] A. H. Lu, E. L. Salabas, and F. Schüth, “Magnetic nanoparticles: Synthesis, protection, functionalization, and application,” *Angewandte Chemie - International Edition*, vol. 46, no. 8, pp. 1222–1244, 2007, doi: 10.1002/anie.200602866.

[77] N. Kaur, S. Gupta, V. K. Jindal, and K. Dharamvir, “Pressure induced transformations in condensed and molecular phases of C60,” *Carbon N Y*, vol. 48, no. 3, pp. 744–755, 2010, doi: 10.1016/j.carbon.2009.10.021.

[78] F. Safizadeh and E. Ghali, “Monitoring passivation of Cu-Sb and Cu-Pb anodes during electrorefining employing electrochemical noise analyses,” *Electrochim Acta*, vol. 56, no. 1, pp. 93–101, 2010, doi: 10.1016/j.electacta.2010.09.046.

[79] N. Surugau and P. L. Urban, “Electrophoretic methods for separation of nanoparticles,” *J Sep Sci*, vol. 32, no. 11, pp. 1889–1906, 2009, doi: 10.1002/jssc.200900071.

[80] M. P. Hughes, “Strategies for dielectrophoretic separation in laboratory-on-a-chip systems,” *Electrophoresis*, vol. 23, no. 16, pp. 2569–2582, 2002, doi: 10.1002/1522-2683(200208)23:16<2569::AID-ELPS2569>3.0.CO;2-M.

[81] J. Fu *et al.*, “Selective adsorption and separation of organic dyes from aqueous solution on polydopamine microspheres,” *J Colloid Interface Sci*, vol. 461, pp. 292–304, 2016, doi: 10.1016/j.jcis.2015.09.017.

[82] R. Nasiri *et al.*, “Microfluidic-Based Approaches in Targeted Cell/Particle Separation Based on Physical Properties: Fundamentals and Applications,” *Small*, vol. 16, no. 29, pp. 1–27, 2020, doi: 10.1002/smll.202000171.

[83] D. R. Breed, R. Thibault, F. Xie, Q. Wang, C. J. Hawker, and D. J. Pine, “Functionalization of polymer microspheres using click chemistry,” *Langmuir*, vol. 25, no. 8, pp. 4370–4376, 2009, doi: 10.1021/la801880u.

[84] N. P. Ivleva, “Chemical Analysis of Microplastics and Nanoplastics: Challenges, Advanced Methods, and Perspectives,” *Chem Rev*, vol. 121, no. 19, pp. 11886–11936, 2021, doi: 10.1021/acs.chemrev.1c00178.

[85] D. Walls and J. M. Walker, “Protein Chromatography,” *Protein Chromatography*, vol. 1485, p. 423, 2017, doi: 10.1007/978-1-4939-6412-3.

[86] B. Bao *et al.*, “Recent advances in microfluidics-based chromatography—a mini review,” *Separations*, vol. 8, no. 1, pp. 1–19, 2021, doi: 10.3390/separations8010003.

[87] P. Y. Yeh, N. A. A. Rossi, J. N. Kizhakkedathu, and M. Chiao, “A silicone-based microfluidic chip grafted with carboxyl functionalized hyperbranched polyglycerols for selective protein capture,” *Microfluid Nanofluidics*, vol. 9, no. 2–3, pp. 199–209, 2010, doi: 10.1007/s10404-009-0535-1.

[88] J. J. Benítez *et al.*, "Microfluidic extraction, stretching and analysis of human chromosomal DNA from single cells," *Lab Chip*, vol. 12, no. 22, pp. 4848–4854, 2012, doi: 10.1039/c2lc40955k.

[89] D. Feng, T. Xu, H. Li, X. Shi, and G. Xu, "Single-cell Metabolomics Analysis by Microfluidics and Mass Spectrometry: Recent New Advances," *J Anal Test*, vol. 4, no. 3, pp. 198–209, 2020, doi: 10.1007/s41664-020-00138-9.

[90] M. Sarma, J. Lee, S. Ma, S. Li, and C. Lu, "A diffusion-based microfluidic device for single-cell RNA-seq," *Lab Chip*, vol. 19, no. 7, pp. 1247–1256, 2019, doi: 10.1039/c8lc00967h.

[91] L. Mats, G. T. T. Gibson, and R. D. Oleschuk, "Plastic LC/MS microchip with an embedded microstructured fibre having the dual role of a frit and a nanoelectrospray emitter," *Microfluid Nanofluidics*, vol. 16, no. 1–2, pp. 73–81, 2014, doi: 10.1007/s10404-013-1221-x.

[92] X. Wang, L. Yi, N. Mukhitov, A. M. Schrell, R. Dhumpa, and M. G. Roper, "Microfluidics-to-mass spectrometry: A review of coupling methods and applications," *J Chromatogr A*, vol. 1382, pp. 98–116, 2015, doi: 10.1016/j.chroma.2014.10.039.

[93] S. W. Lin, C. H. Chang, and C. H. Lin, "High-throughput Fluorescence Detections in Microfluidic Systems," *Genomic Medicine, Biomarkers, and Health Sciences*, vol. 3, no. 1, pp. 27–38, 2011, doi: 10.1016/S2211-4254(11)60005-8.

[94] M. Pumera, "Contactless conductivity detection for microfluidics: Designs and applications," *Talanta*, vol. 74, no. 3, pp. 358–364, 2007, doi: 10.1016/j.talanta.2007.05.058.

[95] P. Xue *et al.*, "Isolation and elution of Hep3B circulating tumor cells using a dual-functional herringbone chip," *Microfluid Nanofluidics*, vol. 16, no. 3, pp. 605–612, 2014, doi: 10.1007/s10404-013-1250-5.

[96] J. C. Contreras-Naranjo, H. J. Wu, and V. M. Ugaz, “Microfluidics for exosome isolation and analysis: Enabling liquid biopsy for personalized medicine,” *Lab Chip*, vol. 17, no. 21, pp. 3558–3577, 2017, doi: 10.1039/c7lc00592j.

[97] N. E. Song *et al.*, “Development and application of a multi-residue method to determine pesticides in agricultural water using quechers extraction and lc-ms/ms analysis,” *Separations*, vol. 7, no. 4, pp. 1–12, 2020, doi: 10.3390/separations7040052.

[98] A. F. Wali *et al.*, “Lc-ms phytochemical screening, in vitro antioxidant, antimicrobial and anticancer activity of microalgae nannochloropsis oculata extract,” *Separations*, vol. 7, no. 4, pp. 1–11, 2020, doi: 10.3390/separations7040054.

[99] A. Oliva and M. Llabrés, “Validation of a size-exclusion chromatography method for bevacizumab quantitation in pharmaceutical preparations: Application in a biosimilar study,” *Separations*, vol. 6, no. 3, pp. 1–12, 2019, doi: 10.3390/separations6030043.

[100] W. De Malsche, J. Op De Beeck, S. De Bruyne, H. Gardeniers, and G. Desmet, “Realization of 1 × 10 6 theoretical plates in liquid chromatography using very long pillar array columns,” *Anal Chem*, vol. 84, no. 3, pp. 1214–1219, 2012, doi: 10.1021/ac203048n.

[101] F. Detobel *et al.*, “Fabrication and chromatographic performance of porous-shell pillar-array columns,” *Anal Chem*, vol. 82, no. 17, pp. 7208–7217, 2010, doi: 10.1021/ac100971a.

[102] W. De Malsche, H. Eghbali, D. Clicq, J. Vangelooven, H. Gardeniers, and G. Desmet, “Pressure-driven reverse-phase liquid chromatography separations in ordered nonporous pillar array columns,” *Anal Chem*, vol. 79, no. 15, pp. 5915–5926, 2007, doi: 10.1021/ac070352p.

[103] J. young Kim and D. O'Hare, "Monolithic nano-porous polymer in microfluidic channels for lab-chip liquid chromatography," *Nano Converg*, vol. 5, no. 1, pp. 1–7, 2018, doi: 10.1186/s40580-018-0151-4.

[104] H. Yin, K. Killeen, R. Brennen, D. Sobek, M. Werlich, and T. Van De Goor, "Microfluidic chip for peptide analysis with an integrated HPLC column, sample enrichment column, and nanoelectrospray tip," *Anal Chem*, vol. 77, no. 2, pp. 527–533, 2005, doi: 10.1021/ac049068d.

[105] J. De Vos, M. Dams, K. Broeckhoven, G. Desmet, B. Horstkotte, and S. Eeltink, "Prototyping of a Microfluidic Modulator Chip and Its Application in Heart-Cut Strong-Cation-Exchange-Reversed-Phase Liquid Chromatography Coupled to Nanoelectrospray Mass Spectrometry for Targeted Proteomics," *Anal Chem*, vol. 92, no. 3, pp. 2388–2392, 2020, doi: 10.1021/acs.analchem.9b05141.

[106] A. M. Striegel and A. K. Brewer, "Hydrodynamic chromatography," *Annual Review of Analytical Chemistry*, vol. 5, pp. 15–34, 2012, doi: 10.1146/annurev-anchem-062011-143107.

[107] L. Duan and L. Yobas, "On-chip hydrodynamic chromatography of DNA through centimeters-long glass nanocapillaries," *Analyst*, vol. 142, no. 12, pp. 2191–2198, 2017, doi: 10.1039/c7an00499k.

[108] L. J. Millet, J. D. Lucheon, R. F. Standaert, S. T. Retterer, and M. J. Doktycz, "Modular microfluidics for point-of-care protein purifications," *Lab Chip*, vol. 15, no. 8, pp. 1799–1811, 2015, doi: 10.1039/c5lc00094g.

[109] J. P. Murrihy *et al.*, "Ion chromatography on-chip," *J Chromatogr A*, vol. 924, no. 1–2, pp. 233–238, 2001, doi: 10.1016/S0021-9673(01)00855-X.

[110] M. Rahbar, A. R. Wheeler, B. Paull, and M. Macka, "Ion-Exchange Based Immobilization of Chromogenic Reagents on Microfluidic Paper Analytical Devices," *Anal Chem*, vol. 91, no. 14, pp. 8756–8761, 2019, doi: 10.1021/acs.analchem.9b01288.

[111] A. Murphy, B. Gorey, K. De Guzman, N. Kelly, E. P. Nesterenko, and A. Morrin, "Microfluidic paper analytical device for the chromatographic separation of ascorbic acid and dopamine," *RSC Adv*, vol. 5, no. 113, pp. 93162–93169, 2015, doi: 10.1039/c5ra16272f.

[112] R. Ishibashi, K. Mawatari, K. Takahashi, and T. Kitamori, "Development of a pressure-driven injection system for precisely time controlled attoliter sample injection into extended nanochannels," *J Chromatogr A*, vol. 1228, pp. 51–56, 2012, doi: 10.1016/j.chroma.2011.05.095.

[113] M. Kato, M. Inaba, T. Tsukahara, K. Mawatari, A. Hibara, and T. Kitamori, "Femto liquid chromatography with attoliter sample separation in the extended nanospace channel," *Anal Chem*, vol. 82, no. 2, pp. 543–547, 2010, doi: 10.1021/ac9017605.

[114] A. Smirnova, H. Shimizu, Y. Pihosh, K. Mawatari, and T. Kitamori, "On-Chip Step-Mixing in a T-Nanomixer for Liquid Chromatography in Extended-Nanochannels," *Anal Chem*, vol. 88, no. 20, pp. 10059–10064, 2016, doi: 10.1021/acs.analchem.6b02395.

[115] H. Shimizu, K. Morikawa, Y. Liu, A. Smirnova, K. Mawatari, and T. Kitamori, "Femtoliter high-performance liquid chromatography using extended-nano channels," *Analyst*, vol. 141, no. 21, pp. 6068–6072, 2016, doi: 10.1039/c6an01195k.

[116] K. Tsougeni, P. Zerefos, A. Tserepi, A. Vlahou, S. D. Garbis, and E. Gogolides, "TiO2-ZrO2 affinity chromatography polymeric microchip for phosphopeptide enrichment and separation," *Lab Chip*, vol. 11, no. 18, pp. 3113–3120, 2011, doi: 10.1039/c1lc20133f.

[117] Q. Min, X. Chen, X. Zhang, and J. J. Zhu, "Tailoring of a TiO2 nanotube array-integrated portable microdevice for efficient on-chip enrichment and isotope labeling of serum phosphopeptides," *Lab Chip*, vol. 13, no. 19, pp. 3853–3861, 2013, doi: 10.1039/c3lc50548k.

[118] D. Zhao, Z. He, G. Wang, H. Wang, Q. Zhang, and Y. Li, “Three-dimensional ordered titanium dioxide-zirconium dioxide film-based microfluidic device for efficient on-chip phosphopeptide enrichment,” *J Colloid Interface Sci*, vol. 478, pp. 227–235, 2016, doi: 10.1016/j.jcis.2016.05.054.

[119] J. J. Lee *et al.*, “Synthetic ligand-coated magnetic nanoparticles for microfluidic bacterial separation from blood,” *Nano Lett*, vol. 14, no. 1, pp. 1–5, 2014, doi: 10.1021/nl3047305.

[120] V. Murlidhar *et al.*, “A radial flow microfluidic device for ultra-high-throughput affinity-based isolation of circulating tumor cells,” *Small*, vol. 10, no. 23, pp. 4895–4904, 2014, doi: 10.1002/smll.201400719.

[121] Z. Zhao, Y. Yang, Y. Zeng, and M. He, “A microfluidic ExoSearch chip for multiplexed exosome detection towards blood-based ovarian cancer diagnosis,” *Lab Chip*, vol. 16, no. 3, pp. 489–496, 2016, doi: 10.1039/c5lc01117e.

[122] S. J. Reinholt and H. G. Craighead, “Microfluidic Device for Aptamer-Based Cancer Cell Capture and Genetic Mutation Detection,” *Anal Chem*, vol. 90, no. 4, pp. 2601–2608, 2018, doi: 10.1021/acs.analchem.7b04120.

[123] S. Magdeldin and A. Moser, “Affinity Chromatography: Principles and Applications,” *Affinity Chromatography*, no. March 2012, 2012, doi: 10.5772/39087.

[124] E. K. Sackmann, A. L. Fulton, and D. J. Beebe, “The present and future role of microfluidics in biomedical research,” *Nature*, vol. 507, no. 7491, pp. 181–189, 2014, doi: 10.1038/nature13118.

[125] S. Song, L. Wang, J. Li, C. Fan, and J. Zhao, “Aptamer-based biosensors,” *TrAC - Trends in Analytical Chemistry*, vol. 27, no. 2, pp. 108–117, 2008, doi: 10.1016/j.trac.2007.12.004.

[126] C. Chen *et al.*, “Microfluidic isolation and transcriptome analysis of serum microvesicles,” *Lab Chip*, vol. 10, no. 4, pp. 505–511, 2010, doi: 10.1039/b916199f.

[127] “Unknown - 1976 - © 1976 Nature Publishing Group,” 1976.

[128] P. Li, Y. Gao, and D. Pappas, “Multiparameter cell affinity chromatography: Separation and analysis in a single microfluidic channel,” *Anal Chem*, vol. 84, no. 19, pp. 8140–8148, 2012, doi: 10.1021/ac302002a.

[129] S. R. Pullagurla *et al.*, “Parallel affinity-based isolation of leukocyte subsets using microfluidics: Application for stroke diagnosis,” *Anal Chem*, vol. 86, no. 8, pp. 4058–4065, 2014, doi: 10.1021/ac5007766.

[130] M. He, J. Crow, M. Roth, Y. Zeng, and A. K. Godwin, “Integrated immunoisolation and protein analysis of circulating exosomes using microfluidic technology,” *Lab Chip*, vol. 14, no. 19, pp. 3773–3780, 2014, doi: 10.1039/c4lc00662c.

[131] L. Wang, G. Musile, and B. R. McCord, “An aptamer-based paper microfluidic device for the colorimetric determination of cocaine,” *Electrophoresis*, vol. 39, no. 3, pp. 470–475, 2018, doi: 10.1002/elps.201700254.

[132] S. Fatemeh Shams, M. R. Ghazanfari, and C. Schmitz-Antoniak, “Magnetic-plasmonic heterodimer nanoparticles: Designing contemporarily features for emerging biomedical diagnosis and treatments,” *Nanomaterials*, vol. 9, no. 1, 2019, doi: 10.3390/nano9010097.

[133] P. Figueiredo *et al.*, “In vitro evaluation of biodegradable lignin-based nanoparticles for drug delivery and enhanced antiproliferation effect in cancer cells,” *Biomaterials*, vol. 121, pp. 97–108, 2017, doi: 10.1016/j.biomaterials.2016.12.034.

[134] H. L. Nguyen, H. N. Nguyen, H. H. Nguyen, M. Q. Luu, and M. H. Nguyen, “Nanoparticles: Synthesis and applications in life science and environmental technology,” *Advances in Natural Sciences: Nanoscience and Nanotechnology*, vol. 6, no. 1, 2015, doi: 10.1088/2043-6262/6/1/015008.

[135] T. Lu, Z. Li, W. Fan, X. Zhang, and Q. Lv, “Nanoparticles for Inhibition of Asphaltenes Deposition during CO2 Flooding,” *Ind Eng Chem Res*, vol. 55, no. 23, pp. 6723–6733, 2016, doi: 10.1021/acs.iecr.5b04893.

[136] M. Kesente *et al.*, “Encapsulation of olive leaves extracts in biodegradable PLA nanoparticles for use in cosmetic formulation,” *Bioengineering*, vol. 4, no. 3, 2017, doi: 10.3390/bioengineering4030075.

[137] K. Lee, J. Lee, D. Ha, M. Kim, and T. Kim, “Low-electric-potential-assisted diffusiophoresis for continuous separation of nanoparticles on a chip,” *Lab Chip*, vol. 20, no. 15, pp. 2735–2747, 2020, doi: 10.1039/d0lc00196a.

[138] M. Seo, S. Park, D. Lee, H. Lee, and S. J. Kim, “Continuous and spontaneous nanoparticle separation by diffusiophoresis,” *Lab Chip*, vol. 20, no. 22, pp. 4118–4127, 2020, doi: 10.1039/d0lc00593b.

[139] V. V. Khutoryanskiy, “Beyond PEGylation: Alternative surface-modification of nanoparticles with mucus-inert biomaterials,” *Adv Drug Deliv Rev*, vol. 124, pp. 140–149, 2018, doi: 10.1016/j.addr.2017.07.015.

[140] X. Li *et al.*, “Control of nanoparticle penetration into biofilms through surface design,” *Chemical Communications*, vol. 51, no. 2, pp. 282–285, 2015, doi: 10.1039/c4cc07737g.

[141] E. D. H. Mansfield, K. Sillence, P. Hole, A. C. Williams, and V. V. Khutoryanskiy, “POZylation: a new approach to enhance nanoparticle diffusion through mucosal barriers,” *Nanoscale*, vol. 7, no. 32, pp. 13671–13679, 2015, doi: 10.1039/c5nr03178h.

[142] J. T. Huckaby and S. K. Lai, “PEGylation for enhancing nanoparticle diffusion in mucus.,” *Adv Drug Deliv Rev*, vol. 124, pp. 125–139, Jan. 2018, doi: 10.1016/j.addr.2017.08.010.

[143] A. Parodi *et al.*, “Bromelain surface modification increases the diffusion of silica nanoparticles in the tumor extracellular matrix,” *ACS Nano*, vol. 8, no. 10, p. 9874—9883, Oct. 2014, doi: 10.1021/nn502807n.

[144] A. A. S. Bhagat, H. Bow, H. W. Hou, S. J. Tan, J. Han, and C. T. Lim, “Microfluidics for cell separation,” *Med Biol Eng Comput*, vol. 48, no. 10, pp. 999–1014, 2010, doi: 10.1007/s11517-010-0611-4.

[145] M. Ebadi, K. Buskaran, B. Saifullah, S. Fakurazi, and M. Z. Hussein, “The impact of magnesium–aluminum-layered double hydroxide-based polyvinyl alcohol coated on magnetite on the preparation of core-shell nanoparticles as a drug delivery agent,” *Int J Mol Sci*, vol. 20, no. 15, pp. 1–17, 2019, doi: 10.3390/ijms20153764.

[146] G. B. Kale, “Thermodynamic Diffusion Coefficients,” *Defect and Diffusion Forum*, vol. 279, pp. 39–52, 2008, doi: 10.4028/www.scientific.net/ddf.279.39.

[147] C. D’Agostino, M. D. Mantle, L. F. Gladden, and G. D. Moggridge, “Prediction of binary diffusion coefficients in non-ideal mixtures from NMR data: Hexane-nitrobenzene near its consolute point,” *Chem Eng Sci*, vol. 66, no. 17, pp. 3898–3906, 2011, doi: 10.1016/j.ces.2011.05.014.

[148] G. D. Moggridge, “Prediction of the mutual diffusivity in binary non-ideal liquid mixtures from the tracer diffusion coefficients,” *Chem Eng Sci*, vol. 71, pp. 226–238, 2012, doi: 10.1016/j.ces.2011.12.016.

[149] F. d’Orlyé, A. Varenne, and P. Gareil, “Determination of nanoparticle diffusion coefficients by Taylor dispersion analysis using a capillary electrophoresis instrument,” *J Chromatogr A*, vol. 1204, no. 2, pp. 226–232, 2008, doi: 10.1016/j.chroma.2008.08.008.

[150] W. R. Bowen and A. Mongruel, “Calculation of the collective diffusion coefficient of electrostatically stabilised colloidal particles,” *Colloids Surf A Physicochem Eng Asp*, vol. 138, no. 2–3, pp. 161–172, 1998, doi: 10.1016/S0927-7757(96)03954-4.

[151] E. G. Scheibel, “Physical Chemistry in Chemical Engineering Design,” *Ind Eng Chem*, vol. 46, no. 8, pp. 1569–1579, 1954, doi: 10.1021/ie50536a023.

[152] J. Grandgirard, D. Poinsot, L. Krespi, J. P. Nénon, and A. M. Cortesero, “Costs of secondary parasitism in the facultative hyperparasitoid Pachycrepoideus dubius: Does host size matter?,” *Entomol Exp Appl*, vol. 103, no. 3, pp. 239–248, 2002, doi: 10.1023/A.

[153] K. Keshmiri, M. Pourmohammadbagher, H. Huang, and N. Nazemifard, "Microfluidics to determine the diffusive mass transfer of a low viscosity solvent into a high viscosity hydrocarbon," *Fuel*, vol. 235, no. August 2018, pp. 1327–1336, 2019, doi: 10.1016/j.fuel.2018.08.108.

[154] J. Qiu, B. Bao, S. Zhao, and X. Lu, "Microfluidics-based determination of diffusion coefficient for gas-liquid reaction system with hydrogen peroxide," *Chem Eng Sci*, vol. 231, p. 116248, 2021, doi: 10.1016/j.ces.2020.116248.

[155] A. Kashani *et al.*, "Simulation of flow dynamics and heat transfer behavior of nanofluid in microchannel with rough surfaces," *International Journal of Thermofluids*, vol. 24, no. October, p. 100901, 2024, doi: 10.1016/j.ijft.2024.100901.

[156] V. Y. Rudyak, S. L. Krasnolutskii, and D. A. Ivanov, "Molecular dynamics simulation of nanoparticle diffusion in dense fluids," *Microfluid Nanofluidics*, vol. 11, no. 4, pp. 501–506, 2011, doi: 10.1007/s10404-011-0815-4.

[157] C. Lim, B. Yan, L. Yin, and L. Zhu, "Simulation of diffusion-induced stress using reconstructed electrodes particle structures generated by micro/nano-CT," *Electrochim Acta*, vol. 75, pp. 279–287, 2012, doi: 10.1016/j.electacta.2012.04.120.

[158] D. L. Cheung, "Molecular simulation of nanoparticle diffusion at fluid interfaces," *Chem Phys Lett*, vol. 495, no. 1–3, pp. 55–59, 2010, doi: 10.1016/j.cplett.2010.06.074.

[159] M. Shademan, R. M. Barron, and R. Balachandar, "Evaluation of OpenFOAM in Academic Research and Industrial Applications," no. May, pp. 1–7, 2013.

[160] Y. Deng, S. Menon, Z. Lavrich, H. Wang, and C. L. Hagen, "Design, simulation, and testing of a novel micro-channel heat exchanger for natural gas cooling in automotive applications," *Appl Therm Eng*, vol. 110, pp. 327–334, 2017, doi: 10.1016/j.applthermaleng.2016.08.193.

[161] A. Wilson, A. Singhai, and V. Rajput, “International Journal of Research Publication and Reviews Simulation of Micro-Channel Based on the Applying Different Boundary Conditions using ANSYS (Fluent),” vol. 5, no. 1, pp. 5575–5587, 2024.

[162] F. Ahmed, Y. Yoshida, J. Wang, K. Sakai, and T. Kiwa, “Design and validation of microfluidic parameters of a microfluidic chip using fluid dynamics,” *AIP Adv*, vol. 11, no. 7, pp. 1–9, 2021, doi: 10.1063/5.0056597.

[163] B. V. N. Sewwandi *et al.*, “Fabrication of size-tunable graphitized carbon spheres with hierarchical surface morphology on p-Si (100) by chemical vapour deposition,” *Sri Lankan Journal of Physics*, vol. 22, no. 1, p. 80, 2021, doi: 10.4038/sljp.v22i1.8093.

[164] Z. Lei, Z. Chen, and X. S. Zhao, “Growth of polyaniline on hollow carbon spheres for enhancing electrocapacitance,” *Journal of Physical Chemistry C*, vol. 114, no. 46, pp. 19867–19874, 2010, doi: 10.1021/jp1084026.

[165] H. Zhao, X. Lu, Y. Wang, B. Sun, X. Wu, and H. Lu, “Effects of additives on sucrose-derived activated carbon microspheres synthesized by hydrothermal carbonization,” *J Mater Sci*, 2017, doi: 10.1007/s10853-017-1258-4.

[166] Y. Zhang, W. Hou, H. Guo, S. Shi, and J. Dai, “Preparation and Characterization of Carbon Microspheres From Waste Cotton Textiles By Hydrothermal Carbonization,” 2019, doi: 10.32604/jrm.2019.07884.

[167] T. A. Khan, H. Kim, A. Gupta, S. Saidatul, and R. Jose, “Synthesis and characterization of carbon microspheres from rubber wood by hydrothermal carbonization,” no. November, 2018, doi: 10.1002/jctb.5867.

[168] S. Mourdikoudis and R. M. Pallares, “Characterization techniques for nanoparticles : comparison and complementarity upon studying,” pp. 12871–12934, 2018, doi: 10.1039/c8nr02278j.

[169] D. Casimir, H. Alghamdi, I. Y. Ahmed, R. Garcia-Sanchez, and P. Misra, “Raman Spectroscopy of Graphene, Graphite and Graphene Nanoplatelets,” *2d Mater*, pp. 2–11, 2019, doi: 10.5772/intechopen.84527.

[170] H. Budde *et al.*, “Raman Radiation Patterns of Graphene,” *ACS Nano*, vol. 10, no. 2, pp. 1756–1763, 2016, doi: 10.1021/acsnano.5b06631.

[171] O. Eren, N. Ucar, A. Onen, N. Kizildag, and I. Karacan, “Synergistic effect of polyaniline, nanosilver, and carbon nanotube mixtures on the structure and properties of polyacrylonitrile composite nanofiber,” *J Compos Mater*, vol. 50, no. 15, pp. 2073–2086, 2016, doi: 10.1177/0021998315601891.

[172] S. Sain *et al.*, “Synthesis and characterization of PMMA-cellulose nanocomposites by in situ polymerization technique,” *J Appl Polym Sci*, vol. 126, no. SUPPL. 1, 2012, doi: 10.1002/app.36723.

[173] J. Osswald and K. T. Fehr, “FTIR spectroscopic study on liquid silica solutions and nanoscale particle size determination,” *J Mater Sci*, vol. 41, no. 5, pp. 1335–1339, 2006, doi: 10.1007/s10853-006-7327-8.

[174] M. Drahansky *et al.*, “We are IntechOpen , the world ’ s leading publisher of Open Access books Built by scientists , for scientists TOP 1 %,” *Intech*, vol. i, no. tourism, p. 13, 2016, doi: http://dx.doi.org/10.5772/57353.

[175] R. Antony, S. Theodore, D. Manickam, P. Kollu, and P. V Chandrasekar, “RSC Advances cyclohexane oxidation with hydrogen peroxide †,” vol. 41, pp. 24820–24830, 2014, doi: 10.1039/c4ra01960a.

LIST OF PUBLICATIONS

No	Description	Category	Impact Factor	Quartile
1	Zhichao Wang, Hongping Yu, Achini Liyanage, Junjie Qiu, Dilantha Thushara, Bo Bao, Shuangliang Zhao, (2022). Collective diffusion of charged nanoparticles in microchannel under electric field, Chemical Engineering Science,Volume 248, Part B, 117264, ISSN 0009-2509, (doi:10.1016/j.ces.2021.117264)	Indexed Journal SCIE, Scopus	4.44	Q1
2	Bao,B.; Wang,Z.; Thushara, D.; Liyanage, A.; Gunawardena, S.; Yang, Z.; Zhao, S. Recent Advances in Microfluidics-Based Chromatography- A MiniReview. Separations 2021, 8,3. (doi:10.3390/separations8010003)	Indexed Journal SCIE, Scopus	2.6	Q3
3	Liyanage, A.; Thushara, D.; Gunawardena, S. (2021). Simulation of Diffusive Transport of Nanoparticles under an Externally Applied Electric Field, From Innovation To Impact (FITI). (doi: 10.1109/FITI54902.2021.9833056)	Full paper, Conference proceeding		